



HAL
open science

(Mechanical effects of light on anisotropic micron-sized particles and their wetting dynamics at the water-air interface

Besira Mihiretie

► **To cite this version:**

Besira Mihiretie. (Mechanical effects of light on anisotropic micron-sized particles and their wetting dynamics at the water-air interface. Other. Université Sciences et Technologies - Bordeaux I, 2013. English. NNT: 2013BOR14813 . tel-00869331

HAL Id: tel-00869331

<https://theses.hal.science/tel-00869331>

Submitted on 3 Oct 2013

HAL is a multi-disciplinary open access archive for the deposit and dissemination of scientific research documents, whether they are published or not. The documents may come from teaching and research institutions in France or abroad, or from public or private research centers.

L'archive ouverte pluridisciplinaire **HAL**, est destinée au dépôt et à la diffusion de documents scientifiques de niveau recherche, publiés ou non, émanant des établissements d'enseignement et de recherche français ou étrangers, des laboratoires publics ou privés.

Numéro d'ordre : 4813

Thèse

présentée à

L'Université Bordeaux 1



Ecole Doctorale des Sciences Physiques et de l'Ingénieur

par

Besira Mekonnen MIHIRETIE

Pour obtenir le grade de

Docteur

Spécialité : Lasers, matière et nanosciences (LMN)

**Effets mécaniques de la lumière sur des particules anisotropes
micrométriques et dynamique du mouillage à l'interface eau-air**

(Mechanical effects of light on anisotropic micron-sized particles and
their wetting dynamics at the water-air interface)

Directeurs de thèse: Bernard POULIGNY et Jean-Christophe LOUDET

Devant la commission d'examen formée de :

M. F. Ren	Professeur, Université de Rouen	Rapporteur
M. S. Hanna	Professeur, Université de Bristol	Rapporteur
M. B. Pouligny	Directeur de Recherche, CNRS	Directeur de thèse
M. J-C. Loudet	Maître de Conférences, Université de Bordeaux	Directeur de thèse
M. A.G. Yodh	Professeur, Université de Pennsylvanie	Examineur
M. J-P. Galaup	Directeur de Recherche, CNRS	Examineur
M. F. Nallet	Professeur Université de Bordeaux	Examineur
M. P. Richetti	Directeur de Recherche, CNRS	Examineur

Acknowledgments

First of all, I wish to thank my supervisors Bernard Pouligny and Jean-Christophe Loudet for directing this work. They gave me the opportunity to work with them and contributed to this thesis with many valuable ideas and helpful feedback. I would like to thank Patrick Snabre for his support with software. I would also like to thank Juan Elezgaray for invaluable discussions and his comments on part of this thesis. I would like to thank Florinda Schembri for her help with the TISEAN software.

I express my heartfelt gratitude to the instrumentation team, Pascal Merzeau, Lionel Buisson and Ahmed Bentaleb and to mechanical workshop teams, Philippe Barboteau , Jean-Yves Juanico, Emmanuel Texier who provided me with the necessary support for the thesis.

I also express thanks to everybody in CRPP for providing me a very pleasant and friendly atmosphere and for your supports whenever I needed.

I am also grateful to the COMPLOIDS (European network), which supported me financially during the last 3 years.

On a more personal note, I would like to thank my family and friends for their unconditional support.

Last but not least, I wish to thank all jury members for their willingness to participate in my defense.

Glossary

PS	<i>Polystyrene</i>
T_g	<i>Glass transition temperature</i>
PVA	<i>Polyvinyl alcohol</i>
K	<i>aspect ratio of the particles</i>
a,b,c	<i>dimension of ellipsoids three semi-axis</i>
a_c, b_c	<i>dimension of contact line (dry region)</i>
T	<i>temperature</i>
ω	<i>beam radius</i>
ω_0	<i>beam waist</i>
I	<i>Intensity</i>
Z	<i>axial distance on the beam axis</i>
L	<i>lense</i>
GM	<i>galvanometric mirror</i>
M	<i>mirror</i>
DM	<i>dichroic mirror</i>
λ	<i>wave length</i>
η	<i>viscosity</i>
P	<i>Power</i>
PD	<i>photodiode</i>
PH	<i>pin hole</i>
k_c	<i>critical aspect ratio</i>
k_{cp}, k_{co}	<i>critical aspect ratio of prolate and oblate ellipsoids resp.</i>
x,y,z	<i>the three co-ordinate axes</i>

Résumé

Nous présentons une série d'expériences sur des particules micrométriques de polystyrène de formes ellipsoïdales. Les rapports d'aspects (k) des particules sont variables, de 0.2 à 8 environ. Ces ellipsoïdes sont manipulés dans l'eau par faisceau laser modérément focalisé. On observe la lévitation et l'équilibre dynamique de chaque particule, dans le volume et au contact d'une interface, solide-liquide ou liquide-liquide. Dans une première partie, nous montrons que des particules de k modéré sont piégées radialement. Par contre, les ellipsoïdes allongés ($k > 3$) ou aplatis ($k < 0.3$) ne peuvent pas être immobilisés. Ces particules « dansent » autour du faisceau, dans un mouvement permanent associant translation et rotation. Les mouvements sont périodiques, ou irréguliers (chaotiques) selon les caractéristiques de la particule et du faisceau. Un modèle en 2d est proposé qui permet de comprendre l'origine des oscillations. La seconde partie est une application de la lévitation optique pour une étude de la transition mouillage total-mouillage partiel des particules à l'interface eau-air. Nous montrons que la dynamique de la transition ne dépend pratiquement pas de la forme de particule, et qu'elle est déterminée par le mécanisme d'accrochage-décrochage de la ligne de contact.

Mots clés : *lévitation optique, effet mécaniques de la lumière, piégeage, ellipsoïde, pinces optiques, interface fluide.*

Abstract

We report experiments on ellipsoidal micrometre-sized polystyrene particles. The particle aspect ratio (k) varies between about 0.2 and 8. These particles are manipulated in water by means of a moderately focused laser beam. We observe the levitation and the dynamical state of each particle in the laser beam, in bulk water or in contact to an interface (water-glass, water-air, water-oil). In the first part, we show that moderate- k particles are radially trapped with their long axis lying parallel to the beam. Conversely, elongated ($k > 3$) or flattened ($k < 0.3$) ellipsoids never come to rest, and permanently “dance” around the beam, through coupled translation-rotation motions. The dynamics are periodic or irregular (akin to chaos) depending on the particle type and beam characteristics. We propose a 2d model that indeed predicts the bifurcation between static and oscillating states. In the second part, we apply optical levitation to study the transition from total to partial wetting of the particles at the

water-air interface. We show that the dynamics of the transition is about independent of particle shape, and mainly governed by the pinning-depinning mechanism of the contact line.

Keywords: *optical levitation, mechanical effects of light, trapping, ellipsoid, optical tweezers, fluid interface.*

Contents

Acknowledgments	2
Glossary	3
Résumé	4
Abstract	4
Introduction générale	8
General Introduction	11
Part A: Mechanical effect of light on micron sized ellipsoidal latex particles	14
A-I: Optical manipulation and trapping of non spherical particles	15
A-II: Experimental hardware and methods	23
A-II.1 Preparation of anisotropic particles	23
A-II.1.a Prolate ellipsoids	23
A-II.1.b Oblate and disk-like ellipsoids	26
A-II.2 Beam characterization	28
A-II.3 Optical levitation setup	32
A-II.4 Data acquisition and analysis	36
A-II.4.a Photodiode signal	36
A-II.4.b Video	37
A-III: Results and Discussion	40
A-III.1 Levitation: Particle behavior in bulk water	40
A-III.2 Particle in contact to an interface, at the beam-waist ($Z=0$)	42
A-III.2a: Water-air and water-oil interfaces	42
A-III.2b: Water-glass interfaces	44
A-III.3 Particle in contact to water-glass interface, at variable Z	61
A-III.3a: Influence of varying beam diameter on particle oscillation	63
A-III.3b: Vertical to horizontal transition	69
A-III.3c: Summary	71

A-IV: Analysis of oscillations	73
A-IV.1 Phase space reconstruction	74
A-IV.2 Dynamics of ellipsoidal particles - Experimental results	78
A-IV.2a: Influence of ellipsoid aspect ratio	79
A-IV.2b: Influence of the beam diameter (parameter Z)	83
A-IV.3 Conclusion	86
A-V: Ray-optics 2d model	87
A-V.1: 2-dimensional ray-optics model	88
A-V.2: 4-pole force / 2-pole torque model	93
A-V.3: Conclusion and prospects	98
Part B: Wetting dynamics of micron sized particles on water air interface	100
B-I: Introduction	101
B-II: Experimental methods	107
B-II.1 Sample preparation	107
B-II.2 Setup	108
B-III: Wetting dynamics of spheres	110
B-IV: Wetting dynamics of prolate and oblate ellipsoids	112
B-IV.1 Results for prolate ellipsoids	113
B-IV.2 Results for Oblate ellipsoids	116
B-IV.3 Discussion	118
Conclusion and prospects	122
Conclusion et perspectives	126
Bibliography	130
Appendix A	139
Appendix B	143

Introduction générale

Le travail présenté dans ce manuscrit concerne essentiellement les comportements de particules ellipsoïdales dans un faisceau laser modérément focalisé.

Historiquement, notre projet de thèse a débuté en juillet 2010. A l'origine, il s'agissait d'étudier la dynamique d'adsorption de particules micrométriques à l'interface de l'eau et de l'air. La question venait d'expériences faites quelques années auparavant par J.C. Loudet et B. Pouligny, avec des sphères de polystyrène ou de verre. Dans ces expériences, on manipule optiquement une particule, initialement dans l'eau, et on la transporte jusqu'au contact avec l'interface. On s'attend à ce que la particule perce l'interface, et s'immobilise ensuite dans une configuration de mouillage partiel, avec une ligne de contact circulaire. La question portait sur la vitesse à laquelle la transition se fait, entre états initial et final de la sphère.

Dans le cas d'une sphère idéale, la transition se décompose en une suite continue de lignes de contact circulaires, depuis un rayon infinitésimal jusqu'à celui correspondant à l'angle de contact d'équilibre. A priori, la dynamique de la transition est régie par la dissipation visqueuse au voisinage de la ligne de contact qui se déplace sur la surface de la particule [[de Gennes 2005](#)] (voir également l'exposé de [[Kaz 2012](#)], documents annexes).

En fait, des expériences exploratoires datant des années 90 ont révélé que ce scénario théorique est très éloigné de la réalité. Les observations avec des sphères de polystyrène ont montré que la dynamique était beaucoup plus lente que celle attendue, et que des particules apparemment identiques effectuaient la transition en des temps très différents [[Bobadova 1995](#), [Danjean 1996](#)]. Corrélativement, les expérimentateurs ont observé que les lignes de contact sur les particules émergées présentaient des irrégularités, et que celles-ci étaient variables d'une particule à l'autre, avec des valeurs très dispersées des angles de contact moyens. Les expériences ont montré aussi que lorsque plusieurs particules sphériques étaient simultanément présentes à l'interface, elles formaient des agrégats de structures aléatoires.

Les irrégularités sont dues à ce que les surfaces des particules ne sont pas parfaitement homogènes [[Chen 2005](#)]. En conséquence les lignes de contact ne sont pas planes, et elles déforment la surface de l'eau autour de chaque particule. Ces distorsions sont la source d'interactions capillaires entre les particules et la cause des agrégations observées [[Lucassen 92](#), [Kralchevsky 2001](#), [Danov 2005](#)]. A partir de ces éléments, l'idée est venue d'étudier la transition avec des particules donnant lieu à des lignes de contact non planes, mais de forme

contrôlée et connue. Les ellipsoïdes déjà étudiés au laboratoire présentait les bonnes caractéristiques [Loudet 2005, 2006, 2009, 2011]. Nous savions déjà qu'une particule allongée (ellipsoïde « prolata ») se place horizontalement en travers de l'interface, avec –à l'équilibre– une ligne de contact en forme de selle de cheval [Loudet 2005, 2006, 2009, 2011, Lehle 2008]. Notre objectif était d'observer si de telles particules présentaient des dynamiques d'émersion différentes de celles des sphères.

Les ellipsoïdes ne sont qu'un exemple très simple de forme non sphérique, dans un contexte où la forme sphérique est l'exception et non la règle. D'un point de vue large, l'étude des dynamiques d'émersion de particules de formes variées est pertinente pour de très nombreuses applications, où des particules jouent le rôle de stabilisant (voire de déstabilisant) pour des émulsions et des mousses [Binks 2002, 2006, Velikov 2007].

Dans la pratique, nous devions capturer et manipuler une particule dans l'eau pour ensuite la faire monter jusqu'au contact avec l'interface (eau-air, typiquement). Une solution simple est d'utiliser la pression de radiation d'un faisceau laser, dans un schéma dit de « lévitation optique » [Ashkin 1971]. Un montage de lévitation mis au point pour des projets précédents [Loudet 2005] existait déjà au laboratoire, et nous disposions également de la technique pour fabriquer des particules de polystyrène ellipsoïdales [Ho 1993].

Des expériences préliminaires, avec des ellipsoïdes peu allongés (rapport d'aspect $k < 3$) ont fonctionné sans aucune surprise : une telle particule est facilement capturée par le faisceau, et se centre sur l'axe en position verticale. La lévitation et l'ascension de la particule sont obtenues facilement, avec quelques milliwatts de puissance.

Par contre, et de façon très inattendue, nous avons constaté que des particules plus allongées ($k > 3$) réagissent très différemment. Ces particules ne se piègent pas radialement, mais ne sont pas rejetées par le faisceau non plus. Elles oscillent de façon permanente autour de l'axe du faisceau, avec une fréquence qui croît avec la puissance du faisceau. Nous avons ainsi découvert un phénomène d'oscillation entretenue d'une particule non sphérique dans un faisceau laser.

D'autres cas de « danse de particule » avaient déjà été signalés dans la littérature, dans des expériences utilisant des pinces optiques, avec des micro-bâtonnets d'oxydes métalliques [Pauzauskie 2006] et avec des petits disques biréfringents [Cheng 2002, 2003]. Mais ces

données étaient sporadiques, et rien n'était proposé dans les articles afférents qui puisse expliquer les oscillations que nous observions en volume dans l'eau¹.

Cette « danse de particule » s'est rapidement imposée comme un problème que nous voulions résoudre, dans un contexte où la manipulation par la lumière d'objets non sphériques mobilise beaucoup d'efforts dans la communauté des pinces optiques et procédés de la même famille. Nos particules étant simples et de caractéristiques bien connues, et nos conditions d'observation dans le montage de lévitation étant confortables, nous avons entrepris une étude systématique du phénomène.

Cette étude des états dynamiques des particules dans le faisceau laser est devenue la composante principale de notre travail de thèse. Elle fait l'objet des cinq chapitres de la partie A du manuscrit. Cette partie devrait intéresser principalement les utilisateurs de techniques de manipulation optique. Nous commençons par une courte revue des travaux menés dans le domaine, concernant les effets mécaniques de la lumière des particules non sphériques (chapitre A-I). Nos moyens et méthodes expérimentales sont décrits dans le chapitre A-II. Les résultats essentiels de nos expériences, avec des particules de différents rapports d'aspect dans des conditions variées d'illumination sont donnés en A-III. Comme nous le verrons, les oscillations ne sont pas toujours périodiques. Des nombreux cas de mouvements irréguliers sont mis en évidence (chapitre A-IV). Une interprétation des mouvements périodiques est proposée dans le chapitre A-V, à partir d'un modèle en dimension 2. Un résultat très significatif du modèle est que les oscillations s'expliquent par la nature des forces et couples optiques, indépendamment du couplage avec les parois du système.

L'objectif initial du projet, concernant la dynamique de transition entre les états de mouillage total et partiel, est traité dans la partie B. Cette partie est relativement courte, essentiellement parce qu'elle ne représente que quelques mois d'expériences à la fin de notre contrat de trois ans. Les expériences que nous avons faites avec les particules ellipsoïdales sont encore peu nombreuses, mais suffisantes pour dégager quelques aspects essentiels des dynamiques d'émersion des particules, sphériques et non sphériques.

Les résultats essentiels de la thèse sont résumés dans la dernière partie (résumé et perspectives). Nous terminons par quelques propositions pour des travaux ultérieurs.

¹ Dans l'article de [Cheng 2003], les oscillations ne sont observées qu'au contact d'une paroi solide. Les auteurs ont proposé un modèle où la friction le long de la surface est une condition nécessaire des oscillations. Dans notre cas, les oscillations sont présentes même très loin de toute paroi.

General Introduction

The work presented in this manuscript is mainly concerned with the behaviours of ellipsoid-shaped particles in response to optical forces from a moderately focused laser beam.

Historically, our PhD project has started in July 2010. It came from a problem that was posed a few years ago by J.C. Loudet and B. Pouligny, about the dynamics of adsorption of colloidal particles at interfaces. The problem was stated as follows: consider a solid particle, of the order of a micrometer in size, initially in bulk water. The particle, made e.g. of glass or polystyrene, is brought in contact to a water-air, or a water-oil, interface. One expects the particle to end up in a partial wetting configuration across the interface, with a circular contact line. The question was: how much time does it take for the particle to make the transition from complete to partial wetting?

With an ideal spherical particle the transition can be decomposed into a very simple sequence that amounts to a continuous series of circular contact lines growing from infinitesimal to the radius corresponding to the equilibrium contact angle. The dynamics of the transition can be inferred from the viscous dissipation due to the shear flow close to the moving contact line [de Gennes 2005] (see also the detailed analysis of this problem in the supplementary information of [Kaz 2012]).

In fact, exploratory experiments dating back to the 90's showed that reality differed much from the above theoretical picture. Observations with polystyrene spheres demonstrated that the transition was much slower than expected, and that seemingly identical particles would emerge at very different rates [Bobadova 1995, Danjean 1996]. Correlatively to this finding, contact lines were seen to be irregular on the micrometer scale. The irregularities were different among different particles, and the average contact angles were different too. When many particles were present at the interface, they would aggregate in random clusters, in clear relation with the irregularities of contact lines.

These irregularities are caused by the fact that surfaces of the particles are not perfectly homogeneous [Chen 2005]. As a consequence contact lines are non planar and distort the water surface around each particle. The distortions are the source of capillary interactions between particles and the cause of random aggregation [Lucassen 92, Kralchevsky 2001, Danov 2005]. On this basis, we reasoned that much might be learnt from experiments where the non-planarity of the contact line was not random but of simple shape and controlled.

Ellipsoid-shaped particles were a good candidate to meet this condition, as far one could tell from previous studies of equilibrium configurations of these particles at water-air and water-oil interfaces [Loudet 2005, 2006, 2009, 2011]. In principle, prolate ellipsoidal particles lie horizontal at the interface, and the contact lines take on saddle-like shapes whose characteristics are known [Loudet 2005, 2006, 2009, 2011, Lehle 2008]. Our objective was to observe whether such particles would emerge through the interface in a way that differed much from that of simple spheres.

Ellipsoidal particles are just a geometrically simple example in the general problem of non spherical particles, which are much more common than spheres in nature and industrial applications. From a wider perspective, studying the dynamics of how non spherical particles get in partially wetted configurations at interfaces is of direct interest to chemical engineering fields around particle stabilized emulsions and foams [Binks 2002, 2006, Velikov 2007].

In practice we had to pick up and manipulate a single particle in water and bring it up to the interface. This job might be simply done using the radiation pressure from a laser beam in an optical levitation scheme [Ashkin 1970]. A levitation setup, which was developed in the course of previous studies on particles at interfaces [Loudet 2005], was available to us in the laboratory, and the technique to fabricate ellipsoid shaped particles was already known and mastered [Ho 1993]. Preliminary experiments with short aspect ratio ellipsoids worked with no surprise: the particle would stand up in the laser beam, get radially trapped on the laser axis and lift up under a few milliwatts of power. Much to our surprise, more elongated ellipsoids behaved very differently: such particles could not be radially trapped; they rather went in and out of the beam in a kind of dance that became faster when the laser power was increased. We thus inadvertently came across a phenomenon of light driven sustained oscillation of a non spherical particle in a laser beam. Observations of “dancing particles” had previously been reported in works with optical tweezers, with metal oxide micro-rods [Pauzauskie 2006] and disks [Cheng 2002, 2003]. However the experimental data were sporadic and no interpretation was available to explain the oscillations that we were observing in bulk water². This “particle dance” was both a challenge to our understanding and a problem of general interest in the frame of optical manipulation of non spherical

² The model proposed by [Cheng 2003] infers the friction of the particle in contact to the cover slip of the sample chamber as the source of oscillations. Oscillations of elongated ellipsoids are observed in bulk water, away from bounding surfaces.

particles, currently a hot topic among the many applications of optical tweezers. We thus focused our work on studying the particle oscillations through systematic experiments.

The work on “dancing” particles has become the major part of our PhD project, and is the matter of Part A in this report. Due to the nature of the investigated problem, this work should be interesting mostly to users of optical manipulation techniques. Part A includes a short review of the literature about optical manipulation of non spherical particles (A-I), followed by a description of our experimental means and methods (A-II). A detailed report of our observations with many particles of different size parameters under different conditions of laser illumination is given in A-III. As we will see, oscillations do not simply amount to periodic motions; many configurations instead lead to chaotic dynamics (A-IV). A tentative model of oscillations in 2 dimensions is presented in chapter A-V. Very importantly the model supports the view that oscillations are due to the nature of radiation pressure forces only, and is then a general property independent of bounding surfaces.

The initial objective about the transition from total to partial wetting is the matter of Part B. This part is rather short, as it only represents a few months of experimenting at the end of our 3-year contract. Experiments with ellipsoids are rather exploratory, but we provide a few novel and instructive data about how the transition proceeds with large aspect ratio prolate particles.

The main results of our work are summarized in the end part together with suggestions for future developments (conclusion and prospects).

**Part A: Mechanical effect of light on micron sized
ellipsoidal latex particles**

A-I: Optical manipulation and trapping of non spherical particles

Radiation pressure (RP) forces from a few-milliwatts laser beam are known to produce forces in the picoNewton range, well enough to levitate and manipulate a small (micrometer sized) dielectric particle [Ashkin 1970, 2006, Roosen 1976]. Since the invention of laser optical tweezers (OT) [Ashkin 1986], based on a single very large aperture beam, considerable savoir-faire and theoretical knowledge have been accumulated in the art of trapping and manipulating particles with light. These works have generated a huge amount of literature; see the reviews by e.g. [Neuman 2004] or [Jonáš 2008].

However research works have dealt essentially with the simplest kind of particles namely spheres. In this case, solutions have been proposed to handle about any kind of particle, from a few tens of nanometers up to about hundreds of micrometers. Transparent spheres whose refractive index is larger than that of the surrounding medium ($n_p > n$, i.e. $m = n_p/n > 1$) may be trapped around the focus of a single large aperture Gaussian beam [Ashkin 1986, Neumann 2004, Jonáš 2008], or between the foci of a couple of coaxial counter propagating Gaussian beams [Ashkin 1970, Roosen 1976-78, Buican 1989, Vossen 2004, Rodrigo 2004,2005a, Kraikivski 2006]. Spheres made of weakly refractive matter ($m < 1$), of reflective or absorbing materials are pushed out of classical Gaussian beams, but, within certain limits, the difficulty may be circumvented by using beams with a hollow core. Laguerre-Gauss structures or optical vortex beams [Gahagan 1996, 1998] and optical bottles [Arlt 2000, Shvedov 2011, Alpmann 2012] are well-known solutions to this problem. An alternate solution, still with a Gaussian beam, is to scan the beam to obtain a time-averaged structure that is equivalent to a hollow beam [Jones 2007].

In the case of a particle made of a homogeneous isotropic non absorbing material, the optical force may be represented as the sum of surface stresses that are everywhere perpendicular to the surface³. Following [Simpson 2009, Simpson 2010b], the local force per unit surface at position \mathbf{r} may be written as:

³ In this context, it is legitimate to use the term “radiation pressure forces” to designate the result of momentum transfer from the electromagnetic field to the particle, in general. We note here that this convention may be in conflict with the one adopted by many authors who restrict “RP forces” to the non conservative part of the

$$\mathbf{f} = \frac{1}{4}|E|^2 \Delta\varepsilon \cdot \delta(\mathbf{n}) \hat{\mathbf{n}} \quad , \quad (\text{A-I.1})$$

The corresponding torque surface density is:

$$\mathbf{t} = \mathbf{r} \times \mathbf{f} \quad , \quad (\text{A-I.2})$$

In the above equations E is the electric field, and $\Delta\varepsilon = \varepsilon_p - \varepsilon_c$ is the difference between the particle dielectric constant (ε_p) and that of the outside continuous medium (ε_c). $\hat{\mathbf{n}}$ is the outwardly oriented unit vector $\hat{\mathbf{n}}$ normal to the surface, and the $\delta(\mathbf{n})$ function means that the force is localized on the interface.

The interaction with the particle causes a change of the linear momentum of light ($\hbar\mathbf{k}$ per photon for a plane wave of wave vector \mathbf{k}); this is the source of the optical force (Eq. A-I.1). Waves in general carry a finite amount of angular momentum, associated with the linear momentum, and called « orbital » momentum. The torque, in Eq. A-I.2, may be viewed as due to the change in the orbital angular momentum of light. There exists another source of angular momentum, associated with the polarization state of light and called « spin » momentum (\hbar per photon for a circularly polarized wave [Beth 1936]). Interaction with the particle in general changes the polarization state; this change consequently creates a torque that can make the particle rotate. The effect is well visible with birefringent particles and circularly polarized beams. Several experiments have been reported where microcrystals have been made to rotate continuously in optical tweezers with circularly polarized beams, see e.g. [Friese 1998, Rodriguez-Otazo 2009].

In the following, we will restrict our attention to situations where polarization effects are negligible. In practice, we will deal only with particles that are supposed to have negligible birefringence, and with linearly polarized beams, unless otherwise stated. In this context, mechanical effects of light are completely described by Eqs. (A-I.1, 2).

Since the force is directed along the normal to the surface, the optical torque acting on a sphere made of a transparent isotropic material is null. Therefore the sphere cannot be made

optical forces. While we do not pretend to oppose this use, we find it useful to clearly indicate what definition we adopt and why.

to rotate under the sole action of optical forces. The trajectory of the spherical particle thus reduces to a triplet of translational degrees of freedom (x, y, z) . The situation is very different with a non spherical particle, since the resulting torque is not null in general. Laser light will move the particle and make it rotate in the same time. Manipulating the particle now implies handling 6 degrees of freedom, (x, y, z) and 3 Euler angles.

Because of this complication, trapping of non-spherical particles is both very different and much less mastered than that of spheres [Wilking 2008]. Little is known about possibilities to effectively trap particles of various shapes, either experimentally or theoretically. There is currently a lot of interest from physicists and engineers about trapping and manipulating elongated particles, in great part due to the proliferating applications of nanotubes and nanorods in biophysics, microfluidics, microelectronics and photonics [Neves 2010, Pauzauskie 2006, Van der Horst 2007, Plewa 2004]. A goal pursued by engineers is to assemble micron-sized structures and mechanisms made of such particles, a challenge that necessitates optical trapping and control of the orientation of individual rods [Van der Horst 2007, Friese 2001]. The concept is illustrated below in Fig. A-I.1. The figure shows a procedure using a classical single beam tweezers to catch, orient and move a micro-rod of a semi-conductor material up to a surface, to later position the rod inside a micro-circuit [Pauzauskie 2006].

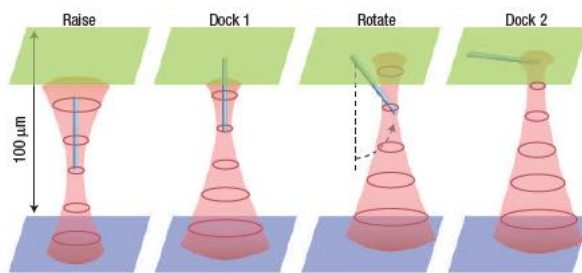


Figure A-I.1: Sketch taken from [Pauzauskie 2006], showing a 4-step procedure to manipulate and position a solid nanowire on the top surface

Experimental observations and the challenge of optically manipulating non spherical objects in general have motivated a bunch of theoretical and numerical studies in the recent years. The case of rods has been addressed along different shape variants, as cylinders [Bareil 2010, Simpson 2011b, Gauthier 1997, 1999], prolate ellipsoids [Simpson 2007, 2011a, Sosa-Martinez 2009] or chains of spheres [Borghese 2008]. Cao et al. recently carried out a systematic study of equilibrium configuration of cylindrical micro-rods in the single-beam OT geometry [Cao 2012], and gathered their data into the state diagram shown in Fig. A-I.2. Note

that a rod can be trapped in different configurations, perpendicular, parallel or oblique, depending on its length and diameter. According to the graphs in Fig. A-I.2, rod-shaped particles of micrometer sizes should be trapped parallel to the laser beam axis, which indeed is in line with experimental observations [Pauzauskie 2006, Rodriguez-Otazo 2009, Neves 2010]. Note worthily the computation predicts that rods having too large dimensions cannot be trapped by the optical tweezers.

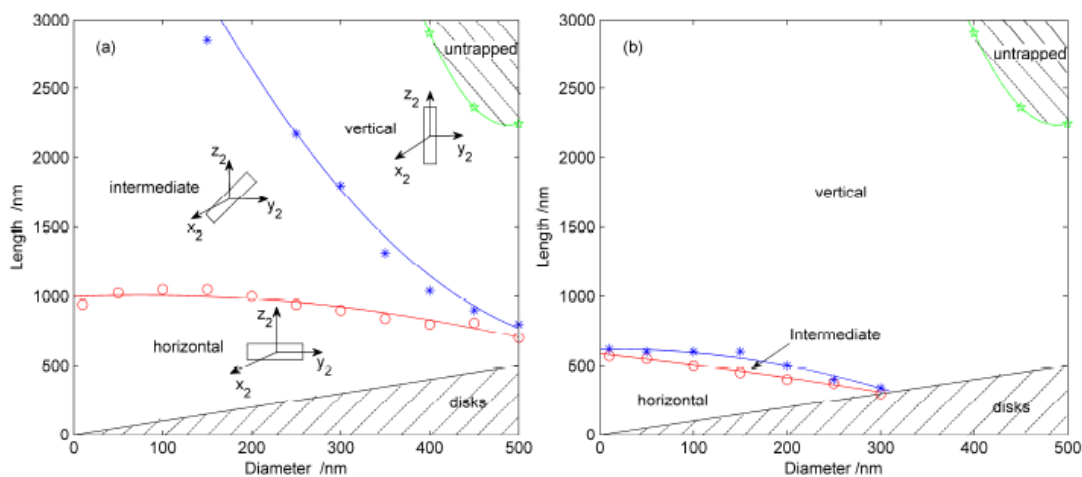


Figure A-I.2: Orientations landscapes of nanowires and microcylinders in (a) linearly polarized and (b) circularly polarized beams. From [Cao 2012].

Objects whose length is less than their diameter (the bottom right end in the graphs of Fig. A-I.2) are disks rather than rods. Similarly to rods, optical manipulation of disks poses some difficulties. The problems to be solved may be generalized to oblate ellipsoids or flat-shaped particles in general. Examples of such particles are erythrocytes, fibroblasts, and cells in general. In the technique called “Optical Chromatography” (OC) [Imasaka 1995], optical forces are used to separate, concentrate and sort biological species. The separation is made possible by the fact that objects having different size, shape and constituent characteristics have different mechanical responses to light, and then follow different trajectories under laser radiation pressure. In addition to shape dependence, orientation of the object and its location with the laser beam critically influences its response to laser illumination. In this context, it is important to get basic knowledge about the optical forces on disks and oblate ellipsoids. Recently Chang et al. carried out a numerical work on oblate ellipsoids [Chang 2012]; the

goal was to predict trajectories of such objects in a weakly focused laser beam, of the kind used in OC geometries. Particles, about $8\ \mu\text{m}$ in diameter, were definitely smaller than the beam diameter ($32\ \mu\text{m}$ at beam-waist). The authors computed the trajectories of an oblate ellipsoid as a function of its aspect ratio for different initial locations and orientations. They found that such particles might follow undulating trajectories, but that they would ultimately get laterally trapped along the laser beam axis, in “orthogonal” configuration (i.e. with their flat side parallel to the axis). This conclusion is in line with previous observations [Cheng 2002, 2003] and theoretical determination of equilibrium states [Grover 2000] of disks or red blood cells in a laser beam (note that Grover *et al.*’s computation took into account the dumbbell-shaped cross section of the erythrocyte). Interestingly, Chang *et al.* noticed that the particle might be either attracted or repelled from the beam axis, depending on its orientation. This property is illustrated in Fig. A-I.3.

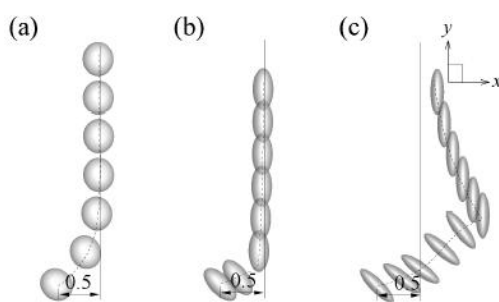


Figure A-I.3: *Computed trajectories of oblate ellipsoids, starting in off-axis position and negative tilt configuration. The particle aspect ratio decreases from left (0.9) to centre (0.5) and right (0.3). The initial offset (0.5) is scaled to the laser beam-waist. The beam propagates in the y direction. See [Chang 2012].*

The above data, either from experiments or numerical simulations may leave the reader with the impression that the action of optical forces and torques on rod-, disk-like, or ellipsoidal particles summarize into either stable (immobile) or unstable (rejection from laser beam) states. Indeed this is what is suggested in Fig. A-I.2 for cylindrical micro-rods. The conclusion, for the experimentalist, may simply be that the particle will be trapped in immobile configuration, or rejected from the laser beam. This conclusion may seem natural if one supposes that optical forces create a kind of energy landscape, with possibly potential wells where the particle can be confined, or barriers that push it out of the beam. Quantitatively, the picture of a potential well is close to correct in the case of a small sphere trapped by optical tweezers. However, this is not exactly true, because optical forces are fundamentally not conservative [Ashkin 1992, Simpson 2010a], meaning that they do not derive from a potential function. Because of this non-conservatism, nothing forbids that a

particle in a laser beam never comes to rest, but instead moves permanently in a more or less complicated manner. Indeed, a few such situations have been reported, as we explain below.

Experimental tests have revealed that the procedure of Fig. A-I works with certain rods but not with all of them. Pazauskie *et al.* noticed that some of their rods would not stay vertically trapped and would undergo sustained back-and-forth tilt motion around the laser beam axis [Pazauskie 2006]. However no formal interpretation was provided to explain the phenomenon. A similar observation was shortly mentioned by Wilking *et al.*, with the letter I from a colloidal “alphabet soup” [Wilking 2008], with no interpretation either.

Neves *et al.* worked with polymeric nano-fibres [Neves 2010], which they were able to align along the beam axis and stably trap in bulk water. However when the fibre was brought in contact to the cover slip of the sample chamber, it switched to a strongly oblique orientation. In this configuration, the fibre was observed to continuously rotate around the laser axis. Though the authors did not provide an explanation of how the particle would adopt a configuration leading to sustained rotation, they could verify that angular velocities were in line with computed values of optical torques [Neves 2010].

An observation that may have some similarities with the above mentioned oscillation of micro-rods [Pazauskie 2006] has been reported by Cheng *et al.* from trapping experiments with disk shaped organic particles [Cheng 2003]. The latter authors were able to stably trap disks *in bulk water* over a large range of dimensions (between 0.4 and 20 μm in diameter) around the focus of a linearly polarized laser [Cheng 2002]. The disks were trapped with their flat sides vertical along the beam axis. However, when the optical trap was moved close to the top window of the cell chamber, the disks were observed to undergo sustained oscillations, combining lateral and tilt motions around the beam axis, see Fig. A-I.4.

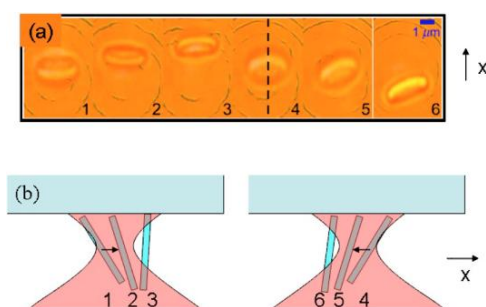


Figure A-I.4: Cheng *et al.*'s experiment with wax disks [Cheng 2003]. Photos in the top row are top views. The bottom sketches show the laser tweezers configuration, and the oscillatory motion of the disk.

Cheng *et al.* proposed an interpretation to explain why the disks, which were stably trapped in bulk water, would oscillate in the configuration of Fig. A-I.4. These authors spotted the change in hydrodynamic drag caused by friction along the top surface as the essential

difference between both situations. They proposed a model expression for the force introduced by the friction that coupled translation and tilt angle of the disk. Based on this expression, they showed that their model would indeed produce a bifurcation, between static and oscillating states disks [Cheng 2003]. The control parameter of the bifurcation is the distance z between the beam-waist and the top surface.

Our own work, the matter of the following sections, is dedicated to more or less similar phenomena which we observed with ellipsoidal particles, including prolate and oblate shapes. Rather than a tightly focused beam in an optical tweezers configuration, we use a moderately focused beam in a simple optical levitation scheme. The size parameters of the experiments, and the beam diffraction length l (about 14 μm), are definitely larger than those involved with micro-rods and single beam traps, but they offer the decisive advantage that the particle can be observed from different directions, while the main physical trends may be extrapolated to the submicron range. Moreover, the ellipsoids have very few birefringence and show little sensitivity to polarization of the laser beam, an appreciable simplification compared to disks and nano-ribbons. As we will see, the ellipsoidal particles either come to rest inside the beam or go through a characteristic back-and-forth motion, with a transition between both regimes that critically depends on their aspect ratio. We offer a complete experimental characterization of the phenomenon, and propose a physical interpretation based on a simple model of RP forces for an ellipsoid, in 2-dimensions. Unlike Cheng *et al.*'s analysis, we draw the conclusion that sustained particle oscillations are due to the nature of RP forces alone, not to a specific surface term in the hydrodynamic drag of the particle.

The following sections are organized as follows:

- In A-II we describe the experimental hardware and procedures. The section includes details on the preparation of the ellipsoidal particles, the levitation setup, and the devices for observation, signal acquisition and recording.
- The main experimental results are presented in A-III. Essentially we describe the different behaviors of the particles, in bulk water, close to a fluid-fluid interface and to a fluid-solid interface. As a major outcome of the observations, a state diagram is proposed that gathers the different dynamic states of particles according to their size parameters.

- Section A-IV is dedicated to the analysis of particle's oscillations using standard tools of non linear systems dynamics. The goal is to clearly identify periodic and non-periodic (akin to chaos) dynamics in the recorded experimental signals.
- In A-V we propose a simple model of light interaction with an ellipsoid. The model is limited to dimension 2, as it only considers the interaction of light with an elliptical body inside a plane. We compute the optical forces and torques in the ray-optics approximation, in the simple case of a collimated beam, i.e. a collection of parallel rays. As we will see, this very simplified picture is enough to produce a bifurcation between static and oscillating states.
- General conclusion and propositions for future works is included at the end.

A-II: Experimental hardware and methods

This chapter discusses the preparation of the materials used and methods applied in the project. The first section explains the sample preparation technique, the second one deals with the method of beam characterization, the third section describes the optical levitation setup and in the last section, we describe the means applied for data acquisition and analysis.

A-II.1 Preparation of anisotropic particles

The two main groups of methods to form non-spherical particles are:

(i) ab initio synthesis of non-spherical particles [Champion 2007]

(ii) Deforming already synthesized spherical particles [Champion 2007].

The former comprises lithography, photo polymerization [Xu 2005, Dendukuri 2005, 2006] etc, whereas the later uses already fabricated spherical particles to deform to a non-spherical geometry. We applied the latter method to obtain spheroidal particles of prolate or oblate type.

A-II.1.a Prolate ellipsoids

We used a technique initially designed by Ho *et al.*, and later further developed by Champion *et al.*, to synthesize prolate ellipsoidal particles [Ho 1993; Champion, 2007]. This technique consists in uniaxial mechanical stretching of polymeric spherical particles, which are previously embedded in polymeric films. This process requires heating up the system above the glass transition temperatures T_g of the spheres and slightly below that of the polymer matrix. Below T_g , polymers are in a frozen glassy state and feature an elastic solid-like behavior: they are almost not deformable and break quite easily when subjected to external stresses. In contrast, above T_g , polymers become soft and behave like a viscoelastic fluid: they can undergo a plastic deformation with high stretching capabilities. This sudden change in state is related to the chain mobility of the polymer: at high temperature long-range segmental motion appears (chain segments of 10 and 20 bonds begin to move) and in effect a rubbery state is manifested [Daoud 1995]. Thus, a polymer at this state can be easily stretched to a different form. Once the particles are stretched, the temperature is lowered below their T_g to freeze their shape permanently since the polymer returns to a solid-like state. This process may be applied to a rather broad range of particle size, typically going from a few hundreds of nanometers up to a few tens of micrometers.

Concerning the present study, the starting particles are commercially available polystyrene (PS) spheres with a diameter $D=10\ \mu\text{m}$ (purchased from either Polysciences®, Molecular Probes® or Invitrogen®). The PS glass transition temperature is around 100°C . We used polyvinyl alcohol (PVA) (FLUKA®) as the film-forming matrix. Hereafter, we list the different steps of the experimental protocol to prepare prolate ellipsoids (see Fig. A-II.1. for an illustration).

Step 1 – The PS beads are first dispersed (mechanical stirring) in an aqueous PVA solution (6-8% wt). The mass fraction of particles is around 0.1% and the average molecular weight of the PVA is 88000 (88% hydrolyzed). The stirring is gentle in order to avoid the formation of air bubbles which may indeed cause film breakage during the stretching step.

Step 2 – The suspension is then poured into a Petri dish (diameter 8 cm) which is stored in an oven at 50°C for few hours to let the water evaporate. Again, the evaporation rate must be moderate to minimize the nucleation of air bubbles.

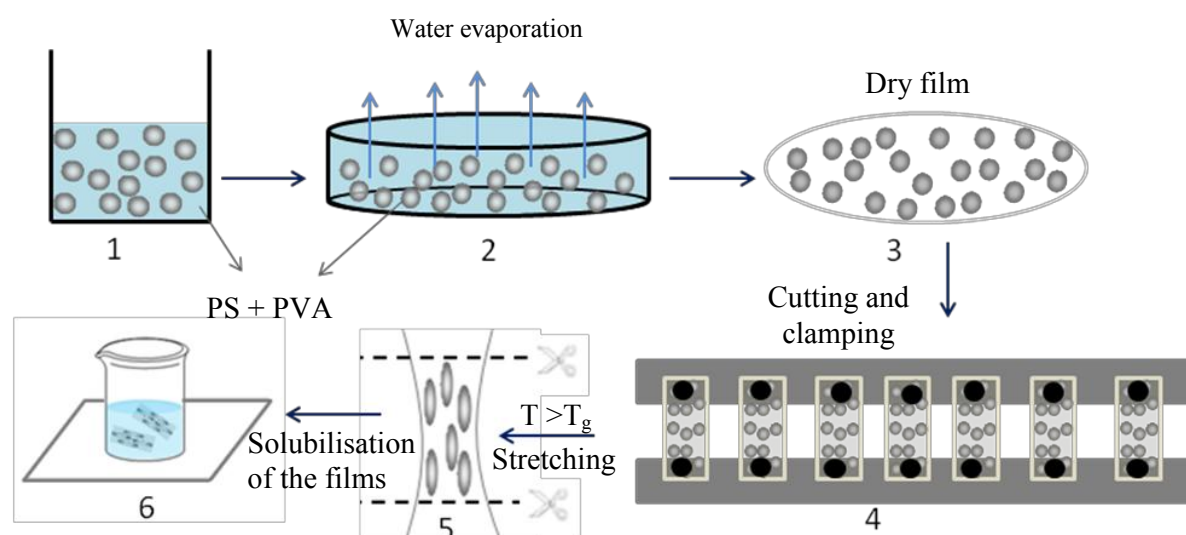


Figure A-II.1: Details of stretching procedure.

Step 3 – After this drying time, the polymer film is solid, homogeneous and relatively flexible. Its thickness is about half a millimeter and it is still humid. This humidity is responsible for the great flexibility and deformability of the film, which can then be peeled off quite easily. Indeed, water plays the role of a plasticizer and therefore decreases the film glass transition temperature, which becomes less than room temperature. If the film were fully dry, i.e. containing only the PVA and the trapped PS beads, it would be rigid and very brittle. Its

properties would be close to those of pure PVA ($T_g \approx 85^\circ\text{C}$), which is semi-crystalline. In this solid state, it is impossible to peel off the film.

Step 4 – The dry film is cut into identical strips of dimensions $L \times l = 2.5 \text{ cm} \times 1.5 \text{ cm}$ which are further clamped on the metal jaws of a stretching device which is fitted in an oven. Only the upper jaw is mobile; its motion may be controlled through a step motor interfaced to simple homemade LabVIEW software. The oven temperature is then raised and reaches 115°C (greater than the T_g of PS). Before stretching, the oven temperature is uniform everywhere.

Step 5 – The strips are stretched vertically at a constant speed equal to $1 \text{ mm}\cdot\text{s}^{-1}$ till the desired elongation is reached. The final elongation sets the prolate ellipsoid aspect ratios k_1 and k_2 : denoting a, b, c the ellipsoid three semi-axes (Fig. A-II.15), we have $k_1=a/b$ and $k_2=a/c$. Once stretched, the films are cooled down to room temperature to freeze the particle ellipsoidal shape.

To locate the most homogeneous deformation zones on the strips, one may initially draw black square grids on them ($0.2 \text{ cm} \times 0.2 \text{ cm}$ for example). After stretching, only the rectangular regions with dimensions consistent with the desired targeted elongation are kept. These regions are mostly located on the central parts of the strips where the stretching is the most homogeneous, as expected.

Before implementing the last two steps, the above protocol may be repeated two or three times (or even more) to get a sufficient amount of particles.

Step 6 – The central zones of the stretched strips are cut and dissolved in distilled water at $T = 50^\circ\text{C}$. The obtained solution is then centrifuged to make the PS ellipsoids sediment and eliminate the upper PVA rich phase.

Many washing cycles with distilled water are necessary to remove PVA traces as much as possible. It is very likely though that there remains some PVA adsorbed at the particle surface, even after several washing cycles. Therefore, in our levitation experiments, it will be important to compare the behavior of ellipsoids with that of PVA treated spheres; thereby avoiding any possible artifact coming from differences in surface chemistry. The ellipsoids are finally dispersed in distilled water and stored in the fridge at 4°C .

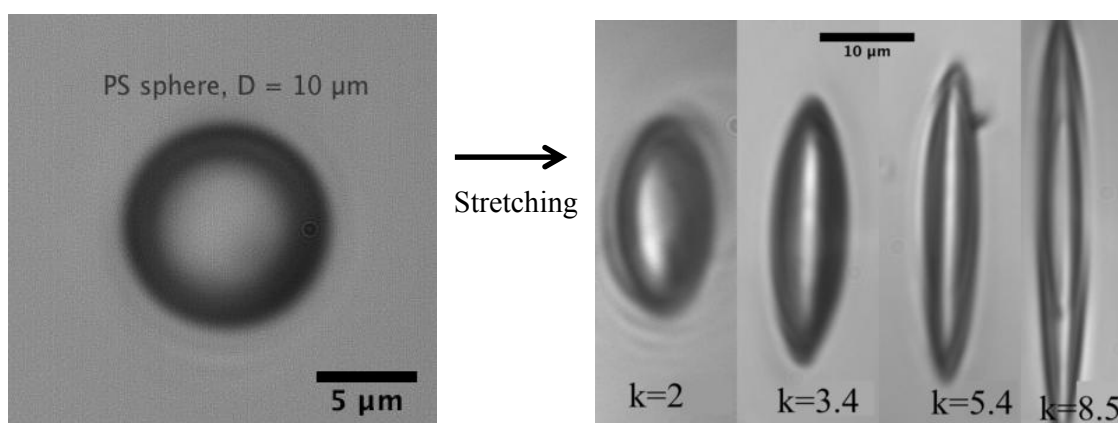


Figure A-II.2: The photos show different prolate ellipsoids made from a sphere by mechanical stretching.

The birefringence behaviors of these ellipsoidal particles were examined using cross polarized optical microscope. We measured relative retardation of the light from the position of extinction and calculated the birefringence. This yields a value of birefringence in the order of fraction of the wavelength of light used.

A-II.1.b Oblate and disk-like ellipsoids

The fabrication of oblate or disk-like particles requires stretching the polymer strips in two orthogonal directions [Champion 2007]. A specific experimental setup was then recently designed by the laboratory instrumentation team. The device consists in two orthogonal mechanical arms on top of which five pairs of jaws are mounted in parallel; these components are fitted in an oven positioned horizontally (see Fig. A-II.3a). The arms are connected to step motors and may be moved independently at different speeds. The whole setup is computer-controlled.

Although the main steps remain essentially the same, the experimental protocol may be adjusted a bit, especially if one wishes to prepare big (several micrometers) and thin (a few hundreds of nanometers) disks. At step 1, the concentration of the PVA solution may be increased a little bit up to 10% wt. This ensures that there is enough polymeric material to stretch the film-forming matrix to (very) high elongation ratios (>150%). At step 4, the dry films may be cut into strips having the shape of octagons instead of squares. Indeed, because of the setup geometry and the likely existence of focused constraints in certain places, squares were always torn apart rather quickly after the jaws started to move. The stretching speed was

also slowed down to $0.1 \text{ mm}\cdot\text{s}^{-1}$ on each axis and the stretching temperature was slightly increased up to 130°C .

These conditions enable the stretching of five octagonal strips in parallel (each with an initial thickness of about half a millimeter and sides equal to 2.5 cm) up to an elongation ratio of 175% on each axis. The final thickness is less than $100 \mu\text{m}$ and all strips are deformed in the same way, as illustrated on Fig. A-II.3b. However, the stretched zones on a given strip are not homogeneous (see the black grid), except in the central region. If we cut out a larger area, we end up with particles having a broad size and aspect ratio distributions. This may not be too much of a problem if we are primarily interested in the behavior of one or two particles and not a huge collection of them.

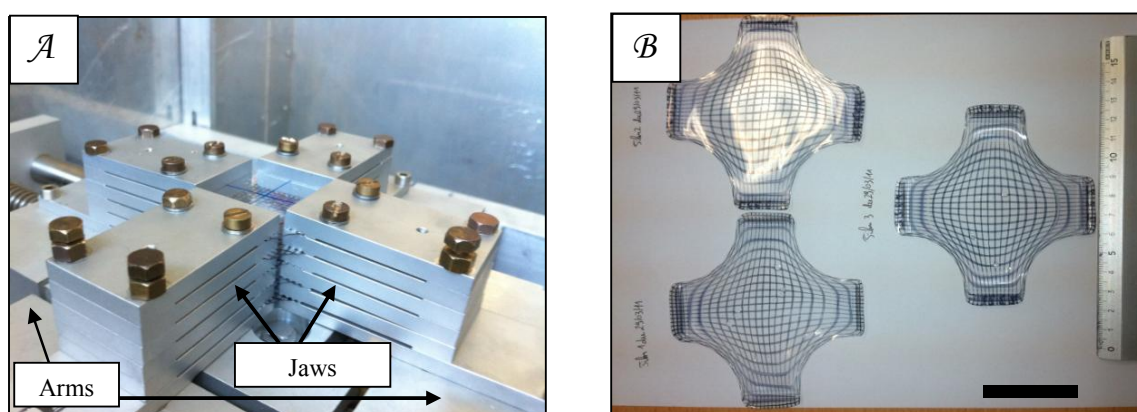


Figure A-II.3: *Fabrication of oblate ellipsoids. (a) A 4-jaw device for 2-d stretching. (b) Photos of stretched film, [Mondiot 2011].*

Sample cell

Once the ellipsoids are prepared, they are diluted ($< 0.01 \text{ % wt}$) in water and placed in a glass cuvette (Fig. A-II.4). The sample cell is 1 or 2 mm in thickness and has polished sidewalls, allowing for observation from all directions. It is placed on a motorized xy stage (we define x , y as the horizontal directions) which can be moved in both directions with 50 nm resolution (Aerotech). The sample cell can also be moved in the z direction (vertical) by means of a manual translation stage. Resolution in z is about 1 micrometer.

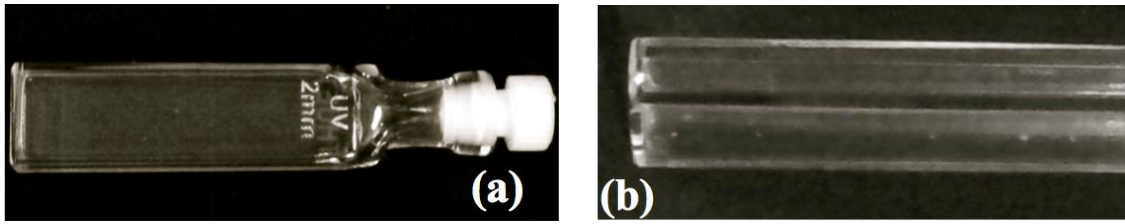


Figure A-II.4: *Standard cuvette cells (THUET, France). The cell is set horizontally in the optical setup. (a) A top view, showing the 1x4 cm top window. The cell in the figure is 2 mm in thickness. (b) An oblique view, showing both the bottom window and the side of the cuvette. The latter is optically transparent too, allowing for side observation.*

A-II.2 Beam characterization

All our experiments use a green continuous wave laser, of wavelength $\lambda=514$ nm (in air). In the first 10 months of our work, the source was an argon ion laser, which was subsequently replaced by a solid state laser, a Coherent Genesis type. Both sources have similar performance in power, providing up to 2 Watts. All the powers that will be mentioned later in the report are measured just upstream of the focusing objective.

We used the knife-edge technique [Dickey 2000] to determine the transverse intensity profile of the laser beam. The principle of this method is to scan an opaque knife transversely across the beam profile along, say, x . For each position of the knife, we measure the transmitted intensity reaching a large area photo detector. From the series of such measurements, we determine the beam waist size, beam waist position and diffraction parameter (M^2) value of our laser beam.

Assuming a Gaussian distribution of the beam profile and also considering uniform parasitic background intensity, the intensity distribution may be written as [Siegman 1986].

$$I(x, y) = I_o \exp\left[\frac{-2(x^2 + y^2)}{\omega^2}\right] + I_1 \quad , \quad (\text{A-II.1})$$

where ω is the beam radius and I_1 is the constant background.

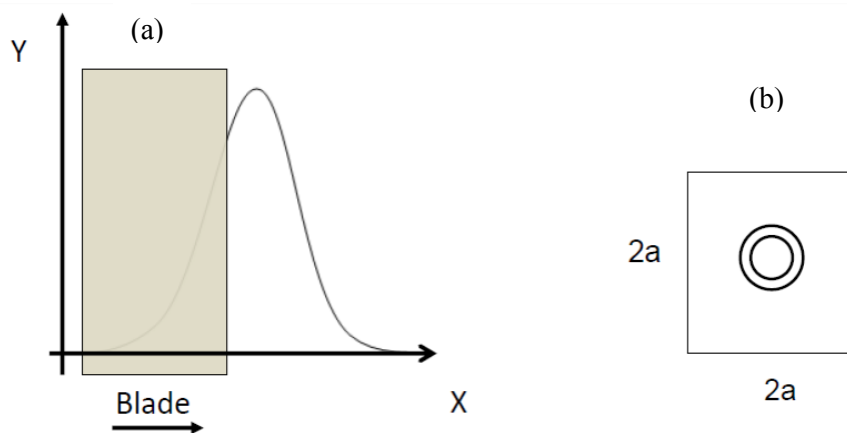


Figure A-II.5: (a) A Gaussian beam profile partially covered with sharp blade. (b) Rectangular region with size $2a$.

Consider a rectangular region (Fig. A-II.5b) of size $a \gg \omega$. Integration of the intensity over the whole rectangular region with respect to y-axis provides:

$$J(x) = AI_o \exp\left(-2x^2/\omega^2\right) + 2aI_1 \quad , \quad (\text{A-II.2})$$

Now the fraction of intensity which is recorded on the photodiode can be expressed as:

$$S(x) = \int_x^\infty J(x') dx' = \alpha - \beta x + \gamma \left(2 - \text{erf} \left(\frac{\sqrt{2}x}{\omega} \right) \right) \quad , \quad (\text{A-II.3})$$

Re-arranging equation (A-II.3), we deduce a fitting equation of the form:

$$y = A + \text{Berf} \left(\frac{x - x_c}{C} \right) + D + Ex \quad , \quad (\text{A-II.4})$$

where A, B, C, D, E are the fit parameters. From equations (A-II.3) and (A-II.4), we obtain:

$$\omega = \sqrt{2}C \quad , \quad (\text{A-II.5})$$

The green Gaussian laser beam operating at 514 nm is directed through a focusing microscope objective of numerical aperture 0.5 (Fig. A-II.6). The beam is vertical and propagates upward. The purpose of the objective is to focus the beam inside the sample, down to a radius ω_o (the beam-waist radius by definition). The vertical position of the objective can be finely tuned by means of a piezoelectric stage, with a $1\mu\text{m}$ resolution. Moving the objective by z simply amounts to moving the beam-waist plane vertically by the same amount (this is not exactly true, but quantitatively a very good approximation).

The blade is located above the objective, at altitude z_b , approximately where the sample (glass cuvette) is located in the optical levitation experiments (Fig. A-II.10). The microscope on top of the setup allows us to observe the transverse section of the beam, together with the blade, as illustrated in Fig. A-II.6b. The diameter of the section (2ω) varies when we move the objective vertically, and goes through a minimum ($\omega=\omega_0$) when the blade crosses the beam-waist plane, $Z=0$.

The knife edge technique thus allows us to measure ω in different horizontal sections, as a function of Z , the distance to the beam-waist plane. The sharp blade is driven through the focused beam in a step by step motion at $0.1\mu\text{m/s}$ (Fig. A-II.6a). The signal given by a photodiode located above the blade is recorded at sampling frequency of 100Hz.

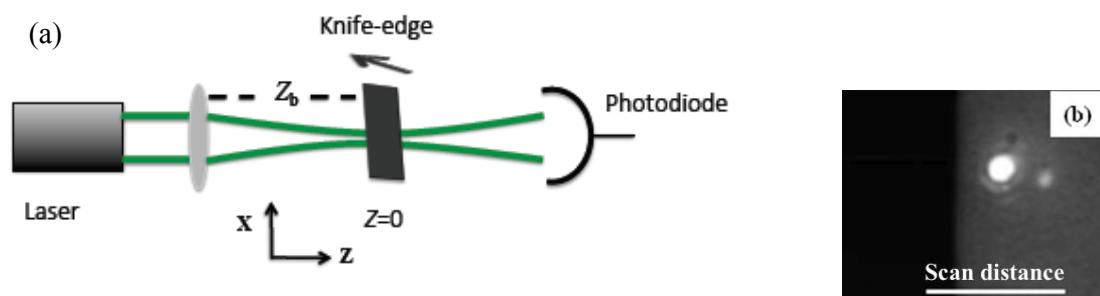


Figure A-II.6: (a) Knife edge technique. The blade (the black rectangle) is moved across the beam, and the transmitted power is measured by means of the photodiode. (b) Image of the blade (dark region) before it covers the beam (bright spot).

The intensity profile detected by the photodiode is fitted by equation (A-II.4). Below is an example of a scan close to the beam-waist plane. Note that the scan profile is well fitted to, with beam waist value of $\omega_0 = 1.3\mu\text{m}$.

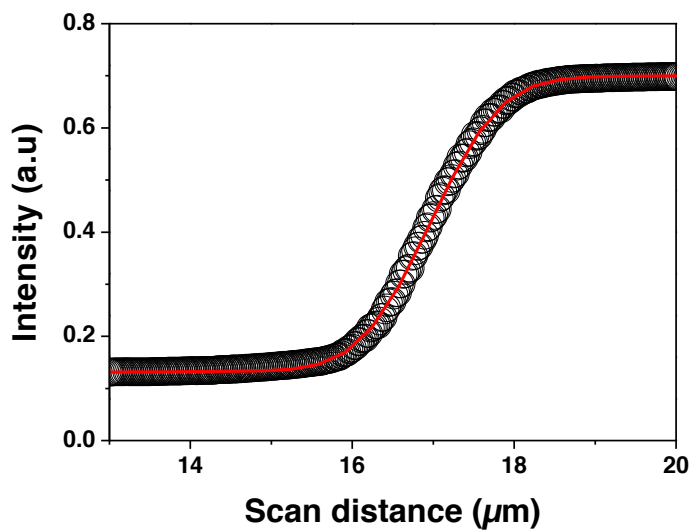


Figure A-II.7: Transmitted power as a function of the blade horizontal position. The blade is about in the beam-waist plane. The red line is the fit from eqn. A-II.4. Data obtained with the Coherent Genesis laser.

For an ideal Gaussian beam, the beam-radius varies according to [Siegman 1986]:

$$\omega(z) = \omega_o \left[1 + \left(\frac{\lambda z}{\pi \omega_o^2} \right)^2 \right]^{1/2} \quad (\text{A-II.6})$$

The large Z limit of Eq.(A.II.6) gives the far-field diffraction angle $\theta = \lambda / \pi \omega_o$. In reality, the laser beam diverges faster than predicted by Eq.(A.II.6). The real divergence is quantified as

$$\theta = M^2 \lambda / \pi \omega_o \quad (\text{A-II.7})$$

The ideal beam has $M^2=1$.

Our experimental data are gathered below, in Fig. A-II.8. The circles represent experimental values whereas the solid line is the fit from equation (A-II.6).

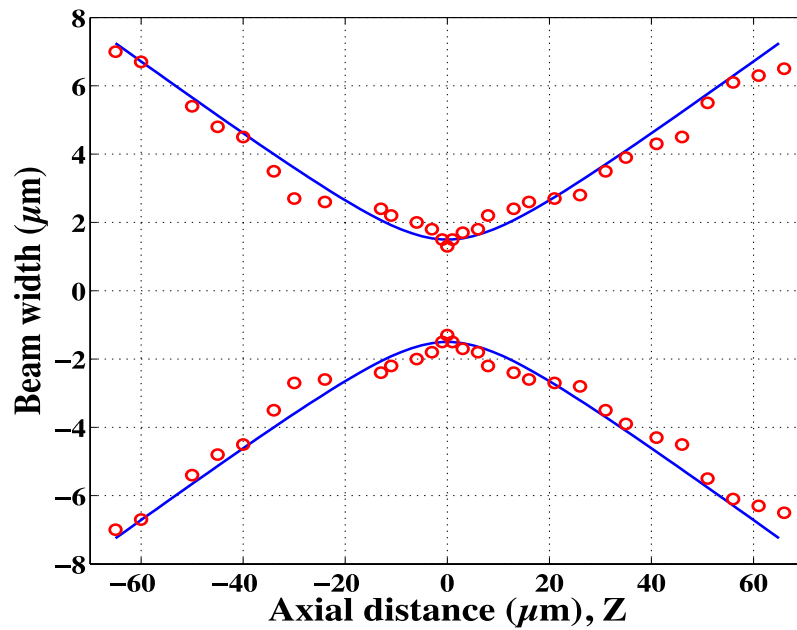


Figure A-II.8: Evolution of the beam radius along the beam axis. Source: Coherent Genesis laser.

The far field angle is obtained from the slope of the beam profile (Fig. A-II.8), i.e $\theta = 0.104$ rad, which results in $M^2 = 1.14$ indicating that the laser has a good beam quality. The beam diffraction length is calculated to be about $10 \mu\text{m}$ (in air).

A-II.3 Optical levitation setup

Here we describe the optical levitation set-up that allows us to study the mechanical effect of light on particles (both spherical and non spherical). The collimated laser light from the source passes through three lenses ($L_{1,2,3}$) before it is focused on the back-aperture of the objective. These lenses are separated by the sum of their focal lengths (pair of lenses form Keplerian telescopes), in such a way the light remains collimated after the telescope. We used coupled galvanometric mirrors for beam steering. The translation of the beam on the sample plane is achieved by a rotation of the beam around the rear focus (F') of the microscope objective. The latter task is achieved by rotating the galvanometric mirrors (GM and F' are in conjugate planes, see Fig. A-II.9).

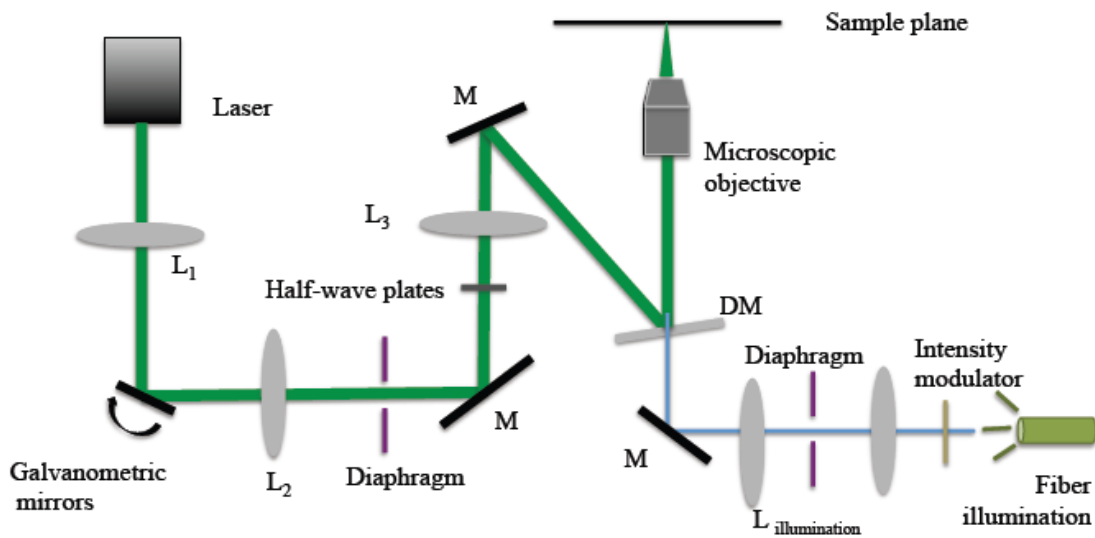


Figure A-II.9: The laser and illumination system of experimental set-up. *M*: mirror. *DM*: dichroic mirror. *L*: lenses.

The remaining part of the set-up is shown in figure A-II.10a. The entire system is built on an optical table fitted with compressed air dampers (to limit vibrations).

As shown in Fig. A-II.10a, the green Gaussian laser beam ($\lambda=514$ nm), made vertical ($//z$), is moderately focused through L_1 objective down to $1.3 \mu\text{m}$ in beam-waist radius. A couple of digital cameras (C_1, C_2) yield simultaneous video images of the particle, from top through L_3 and laterally through L_2 , with an X50 magnification. L_1, L_3 (Zeiss) and L_2 (Mitutoyo) are long-working distance microscope objectives. The top view may be focused into the plane of beam-waist ($z=0$) or at finite distance from it ($z>0$ or <0). The setup also comprises a photodiode (PD), that measures the intensity $I(t)$ of the transmitted laser beam through a pinhole (PH).

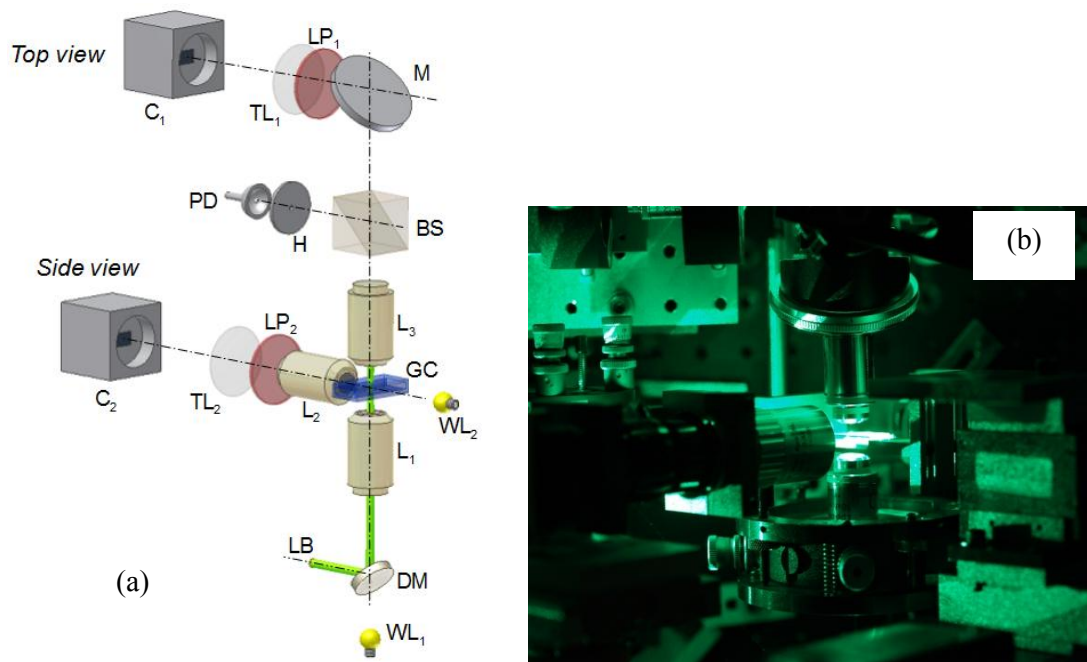


Figure A-II.10: (a) Sketch of optical setup. The elements are not to scale, for clarity. LB: laser beam. BS: beam splitter. $TL_{1,2}$: tube lenses. $LP_{1,2}$: long-pass (red) filters. See text for other symbols definitions. Bright field illumination is provided by two white light sources ($WL_{1,2}$). (b) Photo of the experimental set up, with green laser, showing the three objectives used for focusing and observation.

Observations are performed by means of two video cameras ($C_{1,2}$ in Fig. A-II.10) through a couple of long-working distance microscope objectives: one provides a top view (L_3), through the ceiling of the cuvette, and the other one (L_2) a lateral view. The setup allows us to vary z between -100 and $+100 \mu\text{m}$.

The experiments are carried out with polystyrene particles, inside a glass chamber filled with water (Fig. A-II.4). A typical experiment starts with capturing one particle from the suspension. A simple method amounts to horizontally shift the cuvette to bring a particle across the laser beam (Fig. A-II.11a). The laser beam then drives particle levitation; the particle locks onto the beam axis and starts lifting up. The ascension ends when the particle gets in contact to the chamber's top surface (Fig. A-II.11b).

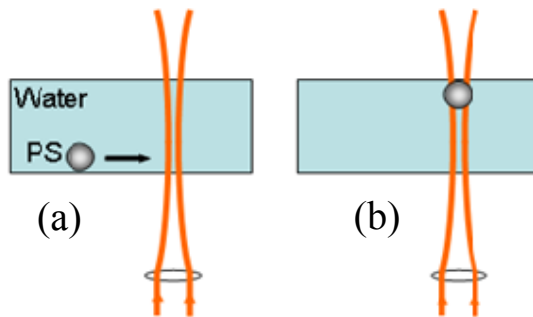


Figure A-II.11: Dilute suspension of polystyrene sphere in water. (a) Bringing the selected sphere to the beam axis. (b) A levitated sphere trapped below the chamber top surface.

The optical levitation described in Fig. A-II.11 only provides 2-dimensional trapping. The 3-dimensional equilibrium is achieved when the sphere hits the ceiling of the cuvette (Fig. A-II.11 b), with the sphere being locked by the radiation pressure force and the contact force exerted by the glass surface. The sphere there is kept immobile (Fig. A-II.11b).

The steps to start levitation of ellipsoids are the same as for a sphere (Fig. A-II.11), with the capture of a particle lying at the bottom of the cuvette. As these particles are heavier than water, most of the ellipsoids are found lying on the lower boundary of the chamber, with a little but discernable amount of Brownian motion. Levitation of a short ellipsoid ($k < 3$, say) is very simple and technically similar to that of a simple sphere. We start the experiment by picking up one ellipsoidal particle with the laser. Within a few seconds, the particle stands up and starts levitating. To keep the particle in focus in the course of levitation, we progressively lower the cuvette (hence the lower position of the cuvette in Fig. A-II.12b). Levitation ends with the ellipsoid sitting vertically in contact to the cuvette ceiling, as sketched in Fig. A-II.12b. In Fig. A-II.12, the beam-waist and the observation plane coincide, i.e. $z = z_F - z_{bw} = 0$. Levitation of longer ellipsoids is a bit more delicate, because these particles do not keep locked on the laser beam axis and constantly oscillate, moving out and back to the axis (this will be the matter of the following Sections). Lifting the particle up to the top demands frequent feedback from the experimenter, using the x, y translation stages to keep the particle within the beam; but this is not difficult.

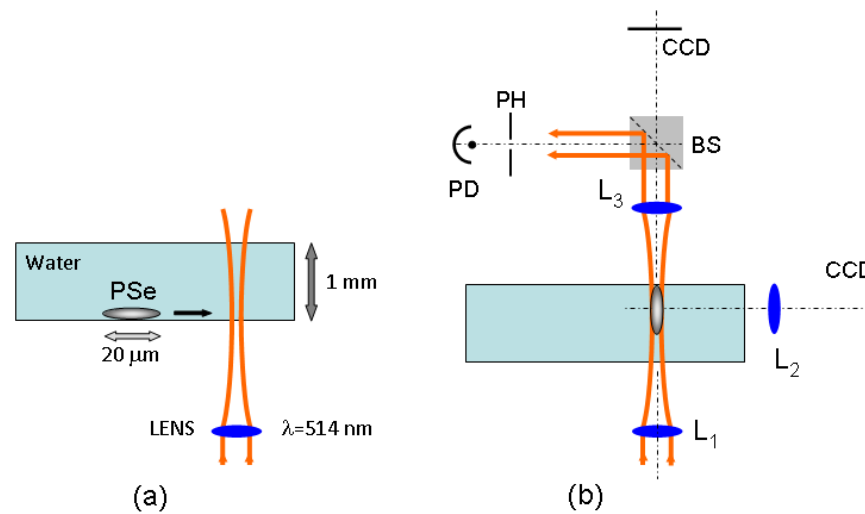


Figure A-II.12: *Optical levitation of ellipsoidal particles. (a), Dilute suspension of ellipsoidal particle in water , initial steps are similar to those of sphere. (b) levitated ellipsoid in contact to the cuvette ceiling. Parts of the setup are not to scale, for clarity. L: objective. CCD: digital camera. PD: photodiode. Bs: beam splitter. PH: pinhole.*

A-II.4 Data acquisition and analysis

We observe the particle levitation, dynamics, image etc. from the top and side views, with a homemade microscope. Such movies and images are analyzed using homemade pattern-recognition software. The photodiode (PD in Fig. A-II.12) measures the intensity $I(t)$ of the transmitted laser beam through a pinhole (PH). This signal is exploited for the diagnosis of the particle dynamics.

A-II.4.a Photodiode signal

The photodiode records the on axis signal loss of the beam due to scattering of light by the oscillating particle (Fig. A-II.13). The particle motion results in fluctuating scattering losses, showing up as time modulation of the photodiode signal. The signal on the photodiode is recorded using homemade software, where we can choose the acquisition rate and duration of recording time. It is not possible to separate translation and rotation components of the particle's motion within $I(t)$, but, compared to image analysis, it offers the advantage of high resolution in time, with sampling frequencies up to 10 kHz.

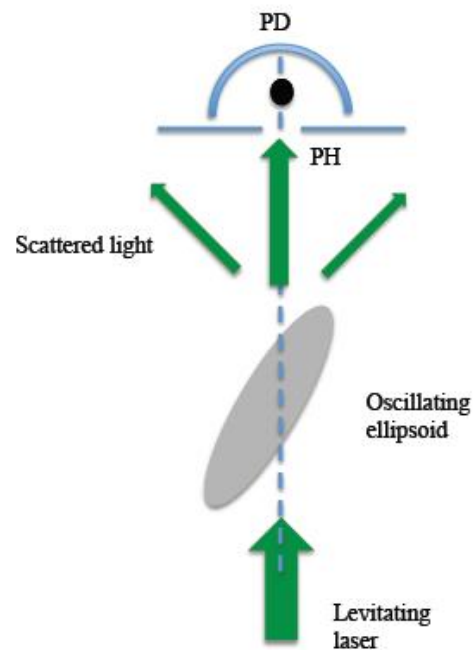


Figure A-II.13: *Signal recording. Sketch of signal detection on the photodiode.*

A-II.4.b Video

Images and movies are acquired from the two CCD cameras (*Edmund optics*) simultaneously using StreamPix software. This enables us to have synchronized observation of the system from different directions, Fig. A-II.14. The capture rate for the camera can be as high as 200Hz but for a typical experiment with reasonable field of view and file size, we used acquisition frequency of 40Hz. The recorded images are used to determine particle size, aspect ratio, beam position and quality of beam profile. The movies are used to study dynamics of the particles.

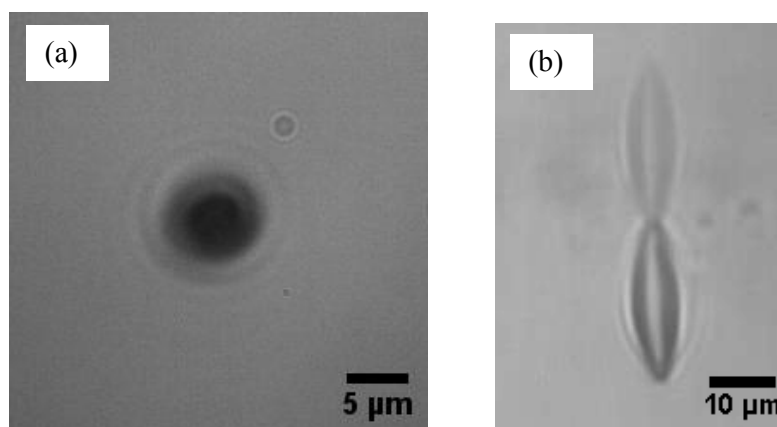


Figure A-II.14: Video microscopy of an elongated particle. (a) Top view. (b) Side view. What is seen is the particle (dark, at bottom) associated with its mirror image reflected by the cuvette top glass (on top, in light grey). The particle and the image are bound tip to tip, indicating that the particle has got in contact to the top glass.

The elongation of the particles is characterized through a couple of aspect ratios, defined as $k_1=a/b$, $k_2=a/c$, with $a>b\geq c$ denoting the half lengths along the ellipsoid's eigen-directions (Fig. A-II.15).

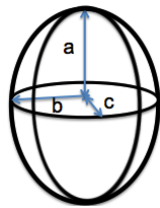
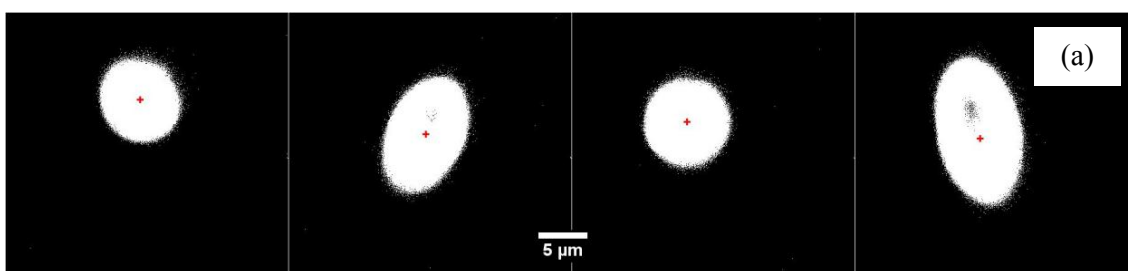


Figure A-II.15: 3-dimensional sketch of an ellipsoid showing the three axes.

A cylindrically symmetric prolate particle has $k>1$, and an oblate one has $k<1$. But we can generalize this definition to non cylindrically symmetrical particles while keeping the distinction between prolate and oblate ellipsoids as particles in our experiment are not too far from cylindrical symmetry, i.e. $a \neq b \approx c$.

Particle tracking

As explained in the previous sections, we record movies of the levitation of particles or/and the dynamics of the levitated particle. These movies are analyzed using a home made (P. Snabre) autocorrelation treatment, that comes as a plugin of ImageJ software. The user must enter the acquisition rate of the movies, long and short axis of the particle in pixels (axisymmetric particles are assumed) and the estimate of the maximum displacement of the particle. The analysis yields elliptical contours that best fit to the top and side images of the particle (Fig. A-II.16a&b). Consecutive images from left to right show the position and orientation of particles in increasing time.



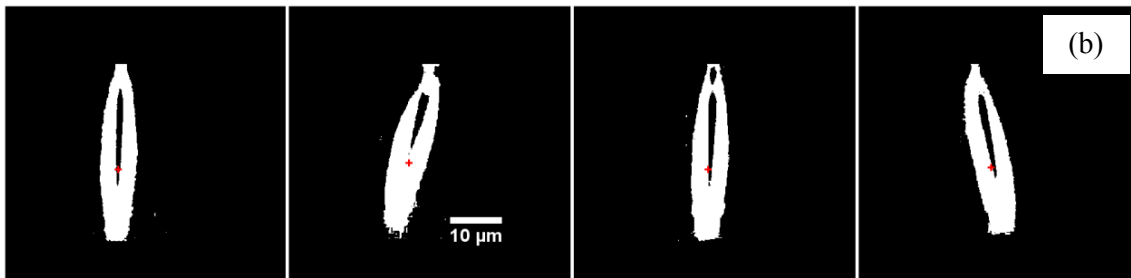


Figure A-II.16: (a) Analysis of consecutive images of an oscillating ellipsoid from top view movie. (b) Analysis of movies from side view. The red cross indicates the barycentre of the ellipsoid.

From the contours we extract the horizontal coordinates of the barycentre and the tilt angle, θ . The tilt angle in general differs from the exact tilt angle ($\theta < \theta_{ilt}$), and is exact ($\theta = \theta_{ilt}$) only when the plane of oscillation is perpendicular to the axis of the side camera. The output file from the analysis comprises the position and angular orientation of the particle in time.

Time (s)	$x(\mu\text{m}) \pm 0.5$	$y(\mu\text{m}) \pm 0.5$	θ (deg) ± 0.8
0.02	24.8	31.1	-15.5
0.04	22.6	30.6	-9
0.06	22	31	-1
0.08	22.5	32	7.9

Tableau 1: Output file from particle tracking. First column is time between each frame, next two columns are the translational displacement of the particle and the last column is rotational displacement.

A-III: Results and Discussion

The first section discusses the levitation behavior of particles in a bulk medium, whereas the remaining two sections, address the behavior of these particles at an interface.

A-III.1 Levitation: Particle behavior in bulk water

When a micron-sized particle is subjected to laser light, it can be locked at some point in space, i.e. optically trapped, or simply pushed against gravity, i.e. levitated. We performed single particle optical levitation. Optical levitation, as sketched in Fig. A-II. 11, only provides a 2-dimensional (2d) trap. The low aperture laser beam does not provide axial trapping by itself contrary to a large aperture beam (as in optical tweezers). However, the static equilibrium may be achieved in bulk if the power is lowered such that the radiation pressure levitation force just balances the particle weight [Ashkin 1970]. A polystyrene spherical particle can be maintained about immobile in such condition, far from the walls of the cuvette. The corresponding levitation power (P_{lev}) is very small (< 3 mW), because of the very small effective weight of a latex particle in water (polystyrene density is only 1.05). The obtained vertical equilibrium is not strictly stable, meaning that the particle drifts up or down if no feedback is applied. Fortunately the drift in water is very slow, leaving us enough time to observe the particle behavior at about constant altitude (Fig. A-III. 1).

In a similar experiment with non-spherical particles, we observed that such particles, either come to rest inside the beam or go through a characteristic dancing motion, with a transition between both regimes that critically depends on their aspect ratio, i.e. oscillation appears when the particle's elongation reaches a threshold value. In such cases, the particle is seen to oscillate as soon as it comes into the laser beam, at the beginning of the experiment and during ascension. We thus bring the particle up in bulk water, away from the cell bottom and still well below the cell ceiling. By tuning the laser beam power down to an appropriate value, of the order of 3 mW, we are able to cancel ascension and maintain the particle at about constant altitude. There, it undergoes sustained oscillations, combining angular and translational excursions (Fig. A-III.1) . See the movie at : <http://youtu.be/UWIMw3V3PZQ>

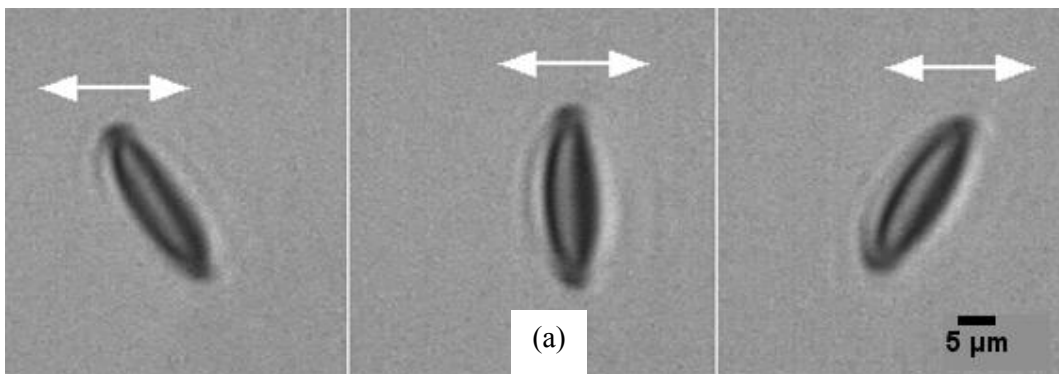
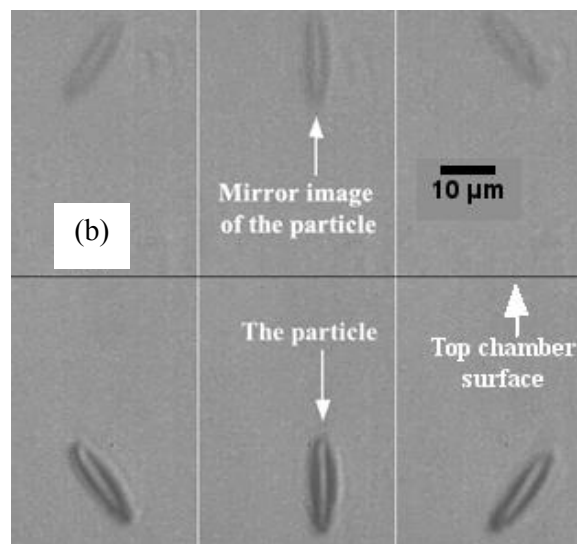


Figure A-III.1: Lateral view of an oscillating prolate ellipsoid. (a) In bulk, far away from the surfaces, where the mirror image of the particle is out of the view of the camera. The arrows show oscillation direction (b) Near the top surface, where both the particle and its mirror image are visible. The bottom one is the true particle located few microns below the black straight line (approximate location of the top chamber surface). Images were recorded every 1 second.



Similarly, in our experiment with oblate ellipsoidal particles ($k < 1$, by definition, see A-II.4b), we have observed that ellipsoids which are not too flat levitate like spheres, whereas very flat ones ($k \ll 1$) show oscillatory states (Fig. A-III.2). See the movie at: <http://youtu.be/6MorGQnzofc>

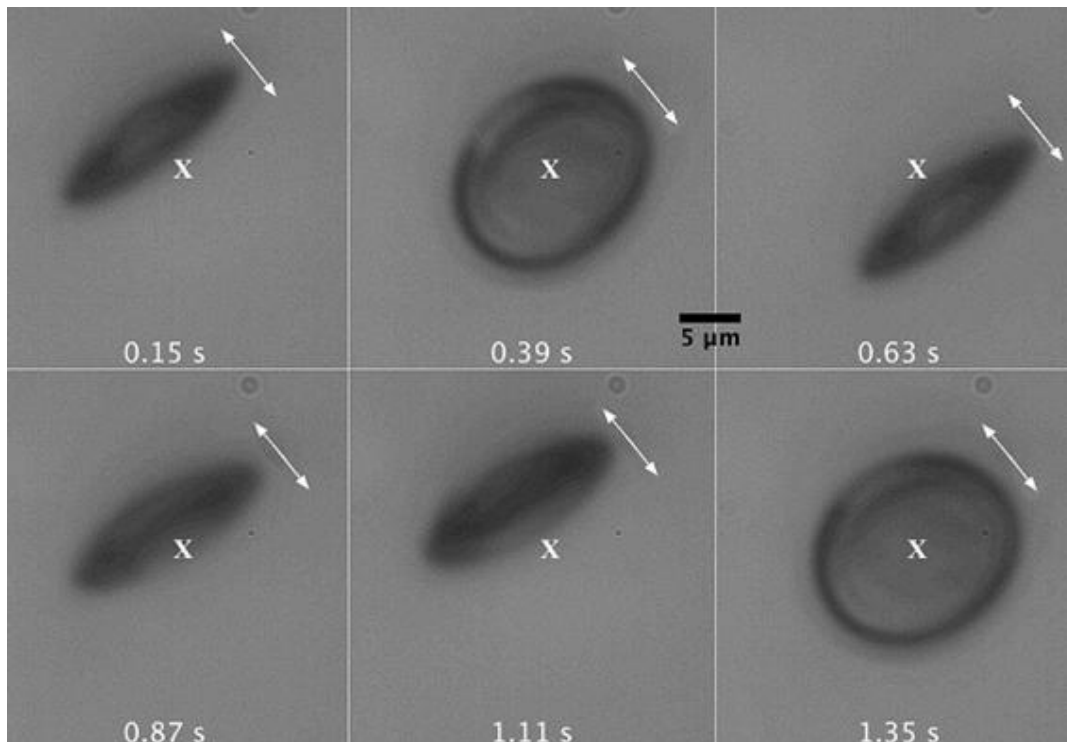


Figure A-III.2: Images taken from top view of an oscillating oblate ellipsoid in bulk. The white cross 'X' – represents the position of the beam center. The arrows represent the oscillation direction.

Figs. A-III.1&2 show the mechanical responses to a moderately focused Gaussian beam of prolate and oblate ellipsoidal particles in bulk water. However, these observations are delicate for they require the use of very low laser power which results in very slow particle motion. Therefore, for practical convenience, most of our experiments were carried out with the particle touching the interface (water-air/oil: sec. A-III.2a and water-glass: sec. A-III.2b) which serves as a contact condition to fix the altitude of the particle within an upper boundary.

A-III.2 Particle in contact to an interface, at the beam-waist ($Z=0$)

A-III.2a: Water-air and water-oil interfaces

When a levitating particle reaches the top of the glass cell, a kind of 3d-trapping is achieved: the particle is locked in Z with its upper tip in contact to the water-glass interface, and the laser beam keeps the particle on-axis (the non oscillating case) or within a few microns around the axis (when oscillation occurs). The nature of the interface does not seem to be

important: similarly to the water-glass interface, we have observed trapping of micron-sized particles in contact to a fluid interface, namely a water-air or a water/oil interface. Dynamical states were similar to those in bulk water, meaning that we observed both static and oscillating states. In the case of the water-oil interface, the viscosity of the oil (79.5% decane + 20.5 % undecane) was matched to that of water (1 mPa.s), making the water-oil system a continuous phase from the viewpoint of hydrodynamics, at low Reynolds number, as in the experiments of [Loudet 2005]. The water-oil interface, in this situation, only ensures the boundary condition in z , while the drag force and torque acting on the particle are the same as in bulk water. Very similarly to behaviors in bulk water, short prolate ellipsoids did not oscillate, while longer ones did. The figure below (Fig. A-III.3) shows the tracking of the centre of mass of an oscillating prolate ellipsoid underneath the water-oil interface.

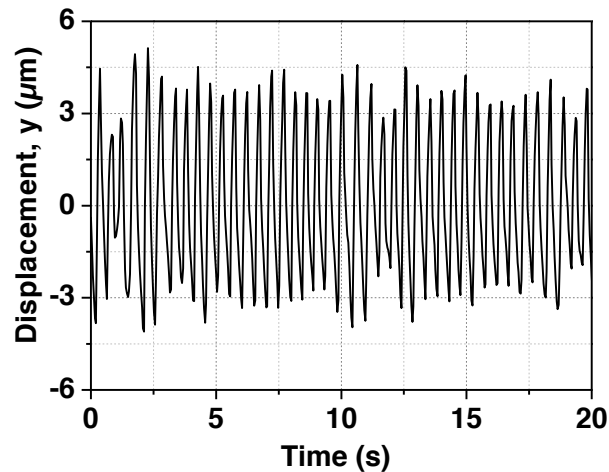


Figure A-III.3: *The analysis of horizontal displacement of an oscillating prolate ellipsoid (from top view movie) under water-oil interface. The experiment is performed at beam waist plane with particle, $k_1=4.1$, $k_2=3.78$ at laser power ~ 15 mW.*

Similar behaviors were observed for oblate ellipsoids at the water-air interface. Below we report an example of oscillating oblate ellipsoids at the water-air interface, where the oscillation dynamics is recorded through the scattered signal at the photodiode.

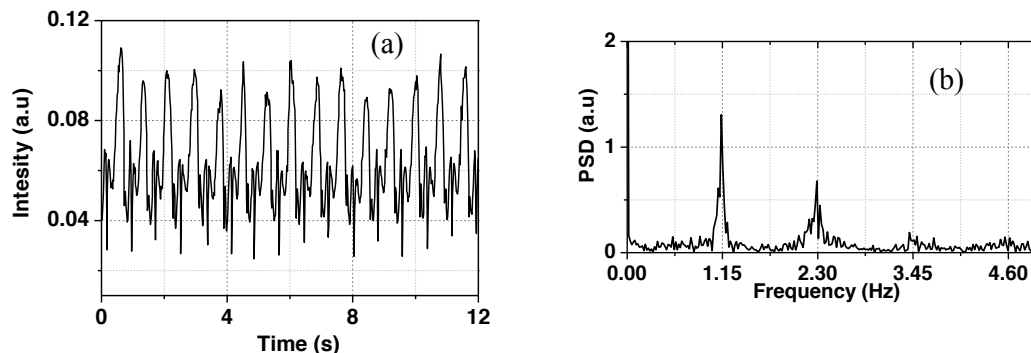


Figure A-III.4: Time series (a) and the corresponding fast Fourier transform, (b) of an oblate ellipsoid oscillating at the water air interface. The experiment is performed at beam waist plane with particle, $k_1=0.26$, $k_2=0.3$ at laser power ~ 15 mW.

As we mentioned above, only the tip of the particle is in contact with the interface, meaning that the particle body is entirely inside water (a kind of complete wetting). This is strictly true with the water-glass interface. In the case of water-air or water-oil interface, complete wetting is maintained only for a while, from a few seconds up to several minutes, say. This leaves enough time for oscillations to be observed and recorded, as reported above. Ultimately, the particle gets through the interface and settles in a partial-wetting configuration, which is energetically favorable. The transition from complete to partial wetting is irreversible, and is a dynamically complex phenomenon. This problem is discussed in part B of the manuscript.

A-III.2b: Water-glass interfaces

This section deals with particles in contact to the water-glass interface. We present the dynamical states of ellipsoids of different aspect ratios. Recall that the particle center is close to the beam waist ($Z = 0$).

A-III.2b.1: Static equilibrium

We start the experiment with spherical PS particles. When such a sphere is exposed to a Gaussian beam it is attracted to the beam center and levitates (Fig. A-III.5.a). The ascension ends when the particle gets in contact to the cell ceiling (Fig. A-III.5.b).

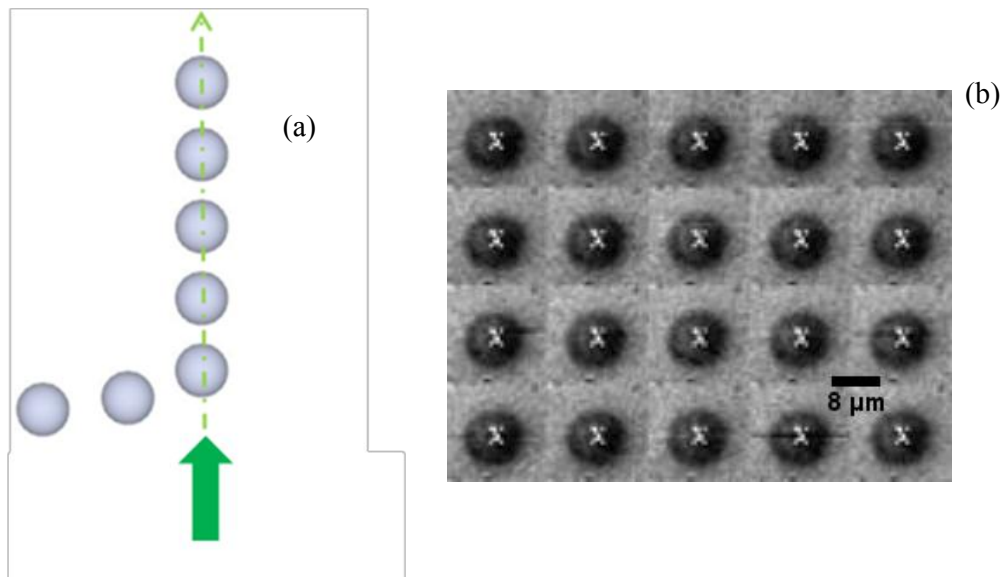


Figure A-III.5: (a) Sketch of levitating sphere. The green arrow represents the laser. (b) Consecutive images (left to right) for the top view of a levitated sphere trapped below the top surface of the cell chamber, where the white cross (X) – represents the position of the beam center. The sphere is $10\ \mu\text{m}$ in diameter. Time step between two successive images is 3 seconds.

Now we come back to the case of prolate particles, and we first deal with moderate aspect ratios, namely $k < 3$, approximately. When exposed to laser beam illumination, such an ellipsoid gets drawn to the beam center; aligns its long axis vertically and laterally locks on the beam axis. Thus, given enough power the ellipsoid levitates without oscillation, like spheres do. The configuration remains the same until the particle reaches the top of the cell.

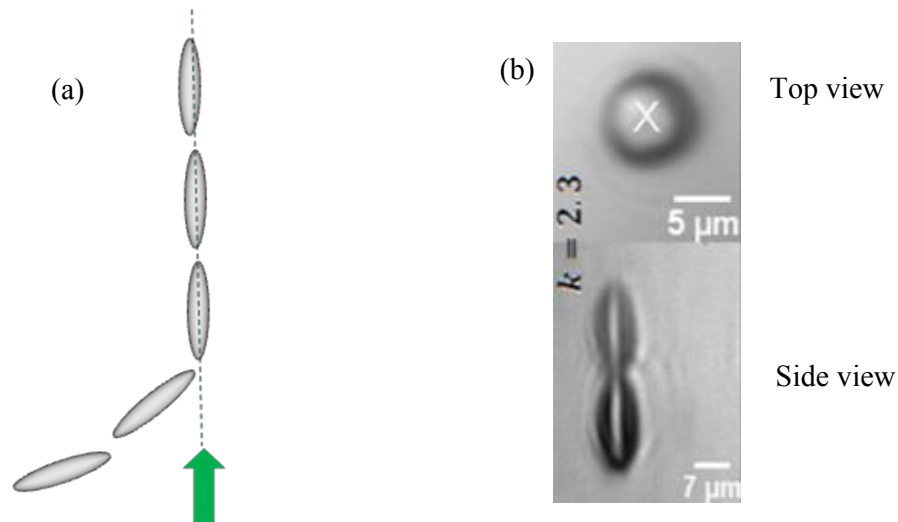
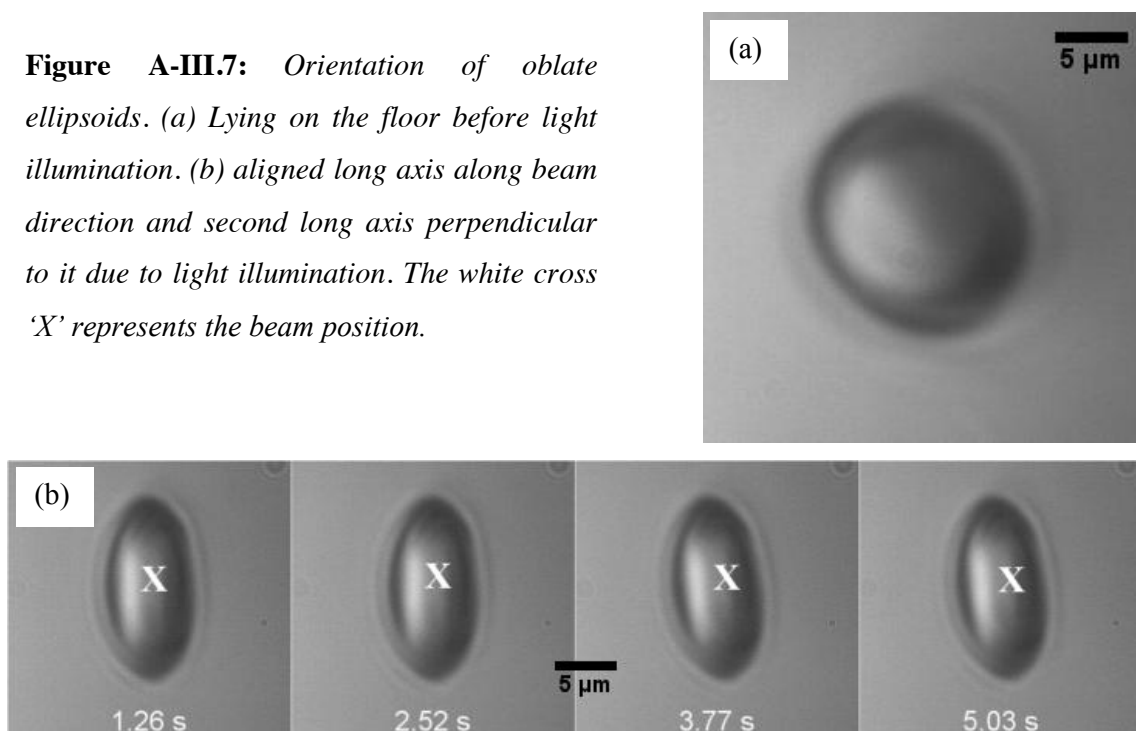


Figure A-III.6: (a) Sketch illustrating the levitation of moderate aspect ratio prolate ellipsoids. The green arrow represents the laser. (b) Example of a prolate particle, in the experiment.

Figure A-III.6b depicts the same particle shown by both top and side microscopes. The ‘X’ in the top view shows the location of the beam center. The side view shows the particle (bottom) and its mirror image (top) through the cell top glass surface. At this point if the laser is switched off, the particle begins to sediment and it loses its preferred direction. See the levitation movie at : <http://youtu.be/zOyLwlpjoGY>

Similarly slightly flattened oblate ellipsoidal particles ($k > 0.33$) also show static equilibrium orientation when exposed to Gaussian laser light. These ellipsoids aligned their long axis parallel to the beam axis and their second long axis perpendicular to the beam axis (parallel to the interface). Below in Fig. A-III.7 we present an example of such a particle ($k_1 = 0.48$, $k_2 = 0.44$).

Figure A-III.7: Orientation of oblate ellipsoids. (a) Lying on the floor before light illumination. (b) aligned long axis along beam direction and second long axis perpendicular to it due to light illumination. The white cross 'X' represents the beam position.



In summary: the critical aspect ratio below which prolate ellipsoids stay static inside the beam is $k_{cp} \approx 3$. A similar critical aspect ratio for oblate ellipsoid is $k_{co} \approx 0.33$. In terms of optical trapping, such particles ($k_{cp} < 3$, $k_{co} > 0.33$) show no definite difference from the sphere they are derived from. But more elongated type of ellipsoids (of prolate and oblate type) show sustained oscillations under laser illumination. The next section discusses these in detail.

A-III.2b.2: Sustained oscillations

Here we consider larger aspect ratio prolate ellipsoids, $k_{l, 2} > 3$. These ellipsoids show sustained oscillations in angular and translational positions when exposed to moderately focused Gaussian laser beam (Fig.A-III.8).

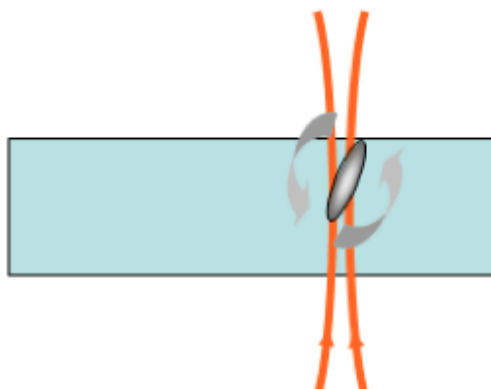


Figure A-III.8 : A large aspect-ratio ellipsoid does not remain immobile inside the levitating laser beam, but undergoes a sustained back and forth motion (a kind of dance, indicated by the curved arrows).

This kind of motion is illustrated in Fig. A-III.9 through sequences of images recorded from different directions.

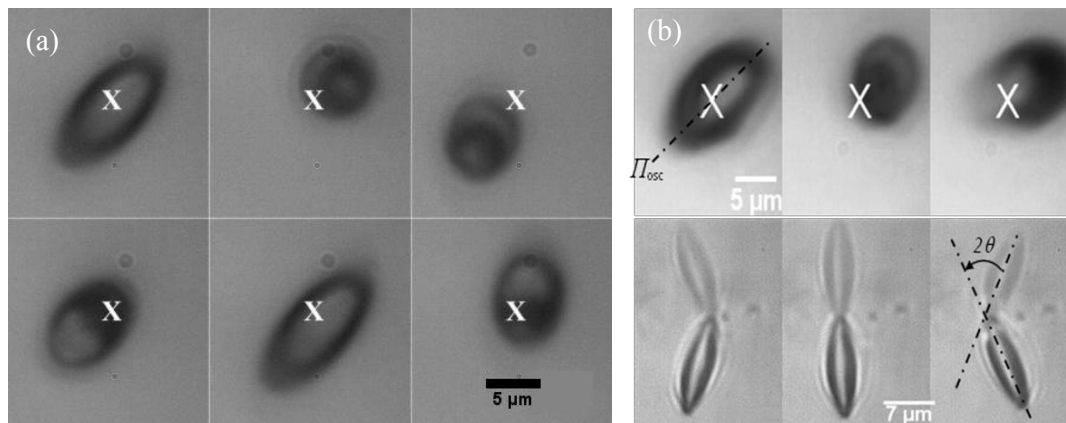


Figure A-III.9: (a) Large aspect ratio ellipsoid (top views): Consecutive images taken every 0.1 second showing different positions and orientations in time. The white cross represents the location of beam axis. (b) Combined top and lateral views. Photos in upper row are top views ((x, y) plane), and those in the lower row are side views ((x, z) plane). Successive frames are separated by 0.1 second. The dotted line in the top marks the instantaneous plane of oscillation (π_{osc}). The angle indicated at the bottom (2θ) is twice the particle long axis tilt angle. Aspect ratio of the ellipsoid: $k_1=3.6$ and $k_2=3.3$.

As revealed in Fig. A-III.9, the particle is seen to constantly oscillate, both in position of its center and in tilt angle.

The movies of sustained oscillation at the water-glass interface are available at <http://youtu.be/1ANBAzpPwck> for the top view of dancing particle and at <http://youtu.be/hDDg8Kx66wc>, for the side view.

Below we discuss these dynamical behaviors.

Regular dynamics

Periodic oscillations were obtained only with ellipsoids of moderate aspect ratio (< 5 , say). Conversely, non symmetrical and longer particles gave irregular signals, with no well-marked peaks in frequency spectrum, similar to chaos. Analysis of images like those in Fig.

A-III.9 yield the translational and rotational coordinates of the particle in time. The images are recorded from both lateral and top views.

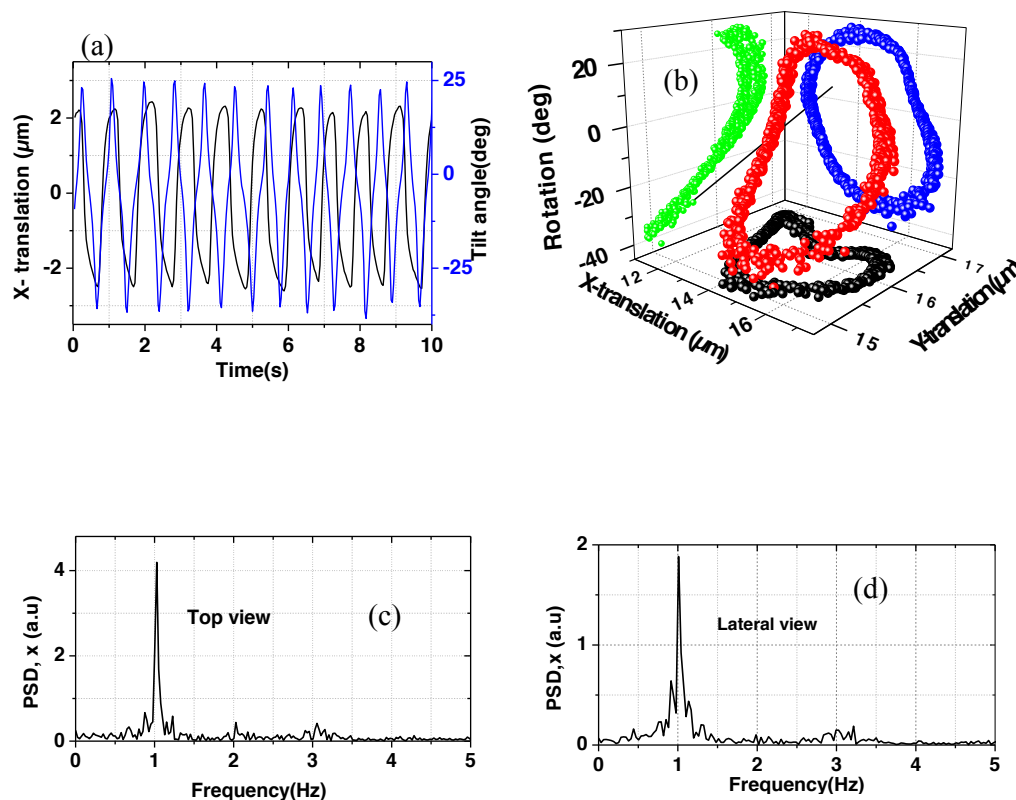


Figure A-III.10: Particle aspect ratio: $k = 4.5$; data obtained from video images. (a) Black curve: particle horizontal x -translation. Blue curve: particle tilt (rotation). (b) The corresponding trajectory in 3d phase space with 2d projections showing a limit cycle. (c and d) The power spectral density of the particle horizontal motion as observed from both directions. Oscillation frequency is close to 1 Hz at laser power of 11 mW.

Below (Fig. A-III.11) we show another example of a presumably periodic motion, based on a photodiode signal, and the associated Fourier power spectrum.

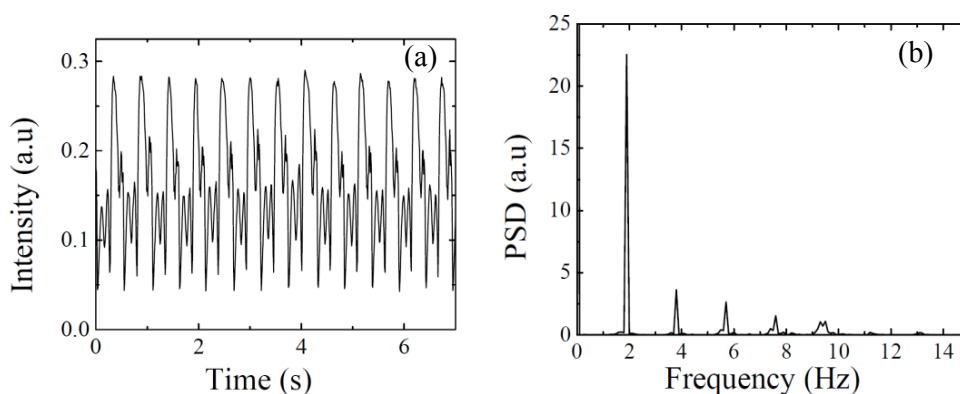


Figure A-III.11: Data recorded with a ($k_1 = k_2 = 3.8$) particle. (a) Modulation of the on-axis laser power recorded with the photodiode and (b) corresponding power spectrum density showing peaks at integral multiple of the fundamental frequency ≈ 2 Hz. Laser power :19 mW.

Influence of the laser power on the particle dynamics

Here we investigate the effect of changing power on the dynamics of the particle. The conclusion, drawn from observations of periodic motions, is very simple: the frequency of oscillation just scales linearly with the laser power. Changing the power does not change the dynamical state qualitatively. The latter conclusion is illustrated in Fig. A-III.12. The figure shows the effect of increasing the power from 9.1 mW (top row) to 22.3 mW (bottom row).

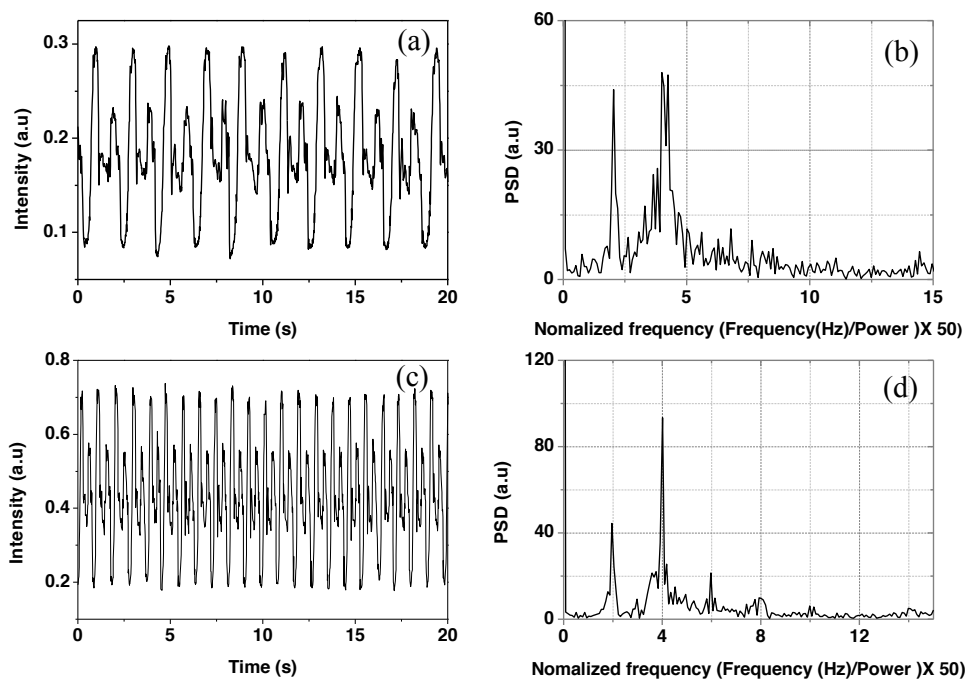


Figure A-III.12: Photodiode signal from (close) periodically oscillating particle ($k=4.1$) at two different powers. (a&c): Time series at 9.1 mW and 22.3 mW respe. The graphs at (b&c) are the corresponding power spectral densities (PSD). For clarity, the frequency has been normalized by the laser power.

The signal keeps the same morphology, while the period is divided by 2.44, the ratio of involved powers. We repeated the same test for different particles and reached the same conclusion, see Fig. A-III.13 for a summarizing graph.

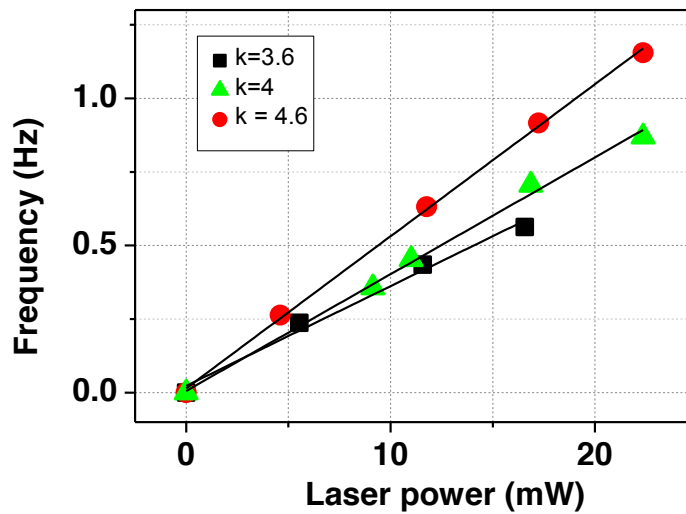


Figure A-III.13: Proportionality of laser power and oscillation frequency of the particle. Tests with 3 ellipsoids of different aspect ratios.

Effect of fluid viscosity

The particles in our experiments and their velocities within the laser beam are small enough for inertial effects to be negligible¹. We then guess that the observed dynamics only involve laser radiation pressure forces and Stokes drag forces and torques. The former are proportional to the laser power, and the latter are proportional to the fluid shear viscosity η .

¹ We verify that this condition is well satisfied in our experiments by estimating the particle Reynolds number, $Re = \rho v a / \eta$, with $\rho = 1.05 \text{ g.cm}^{-3}$, $\eta \cong 0.01 \text{ Poise}$. v is the particle velocity, which we estimate as $v \approx a \cdot f$, where f is the frequency of the main peak in the power spectrum. With $a = 15 \text{ }\mu\text{m}$ and $f \leq 5 \text{ Hz}$, we obtain $Re \approx 10^{-3}$. Then inertia forces and torques are completely negligible.

Experimentally we may check the validity of this statement by changing the viscosity and observing the corresponding change in the particle dynamics. Practically, we must change the viscosity of the medium without significantly changing the index of refraction. This can be achieved by varying the temperature of the medium, as the viscosity of the liquid decreases with increasing temperature.

The relation between temperature (T) and the viscosity may be given by [Bansal 2006]:

$$\eta = \eta_o \left(\frac{1}{1 + \alpha t + \beta t^2} \right) \quad , \quad (\text{A-III.1})$$

where α and β are constants depending on the type of liquid. For water, and temperature in Celsius degrees: $\eta_o = 1.79 \cdot 10^{-3}$ mPa.s, $\alpha = 0.03368$ and $\beta = 0.000221$.

We changed the temperature of the medium from 10 to 60 °C, resulting a viscosity change from 1.2 to 0.3 mPa.s (a x3 decrease of the viscosity), whereas the change in index of refraction is insignificant (< 0.5%). The temperature was regulated by circulating water and thermocouple was used to measure the temperature of the water medium inside the sample cell. We measured the oscillation frequencies of a few ellipsoids as a function of the sample temperature. We found a linear relationship between viscosity of the medium and period of oscillation, within statistical scatter (Fig. A-III.14.b).

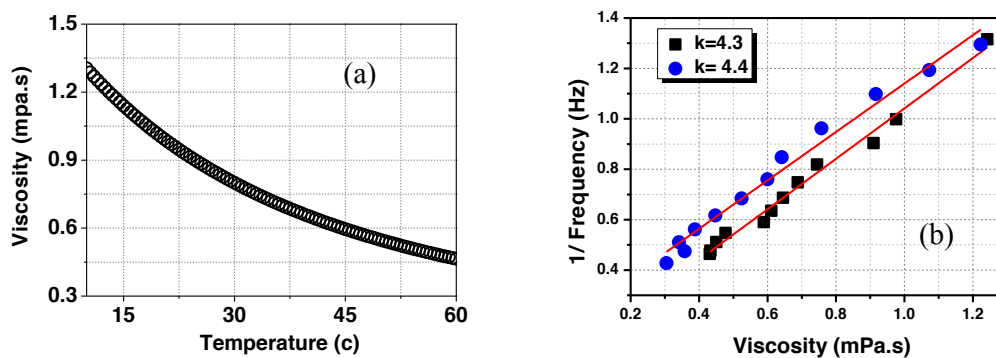


Figure A-III.14: (a) the viscosity of water at different temperatures plotted using eqn.A-III.1. (b) Two sets of data showing the proportionality of the viscosity of the fluid to the inverse of particle oscillation frequency.

In summary, we performed series of experiments by changing the laser power and viscosity of the medium and it did not change the dynamical state, qualitatively. It only changed the main frequency, which is found simply proportional to P/η .

Irregular dynamics

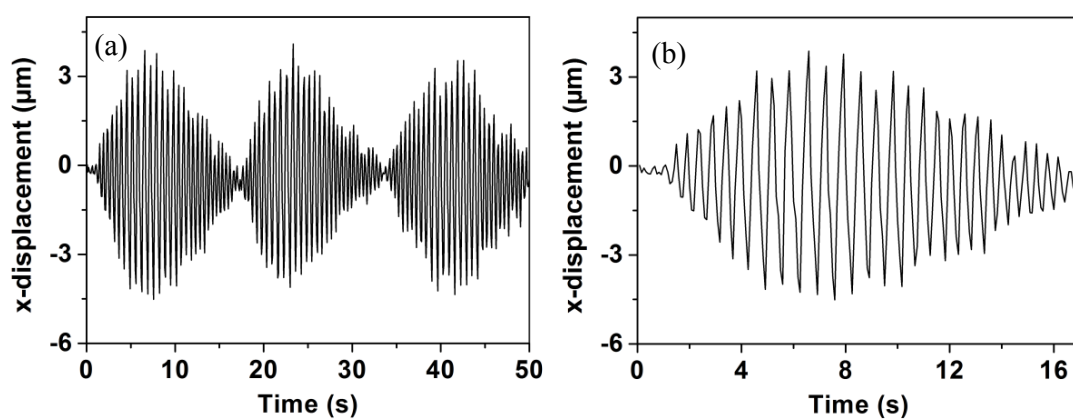
The dynamics of levitated ellipsoids is strongly affected by the symmetry of particles. In the previous sections we have only considered approximately (cylindrically) symmetric ellipsoids. In this paragraph we show that a slight amount of asymmetry causes different dynamics.

Below we report the dynamics of a non-symmetric ellipsoid, namely $k_1 = 4.2 \pm 0.05 \neq k_2 = 4.0 \pm 0.05$, from the image analysis of the video recording.

This particle is seen to oscillate in a complex way:

- i. The amplitude of oscillation is modulated in time, Fig. A-III.15a, b&c.
- ii. The plane of oscillation changes continuously, Fig. A-III.15d.

We define the plane of oscillation Π_{osc} from the x, y coordinates of the particle center. Fig. A-III.15d below shows the successive positions of Π_{osc} . Fig. A-III.15a and Fig. A-III.15b show the envelope of oscillation that repeats itself.



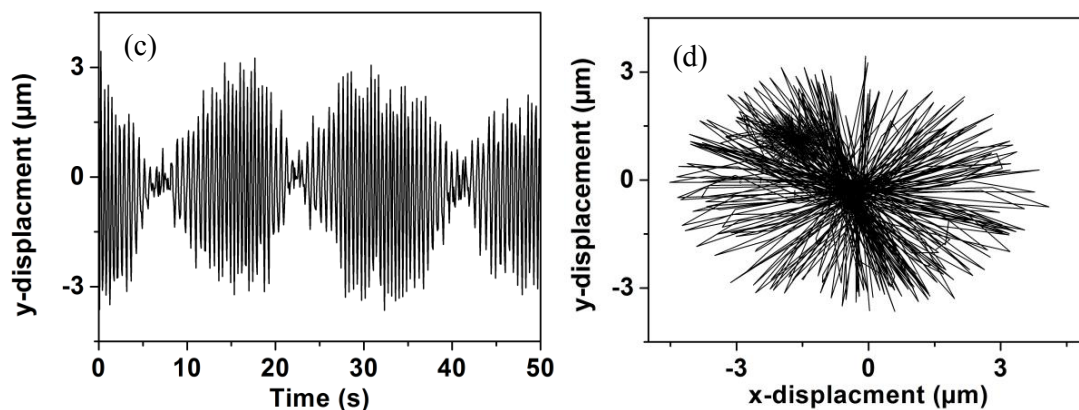


Figure A-III.15: Tracking the position of the ellipsoid in time. The graphs show the change in position of the particle in x (a&b) and y (c) coordinates with time. The x, y trace (d) reveals the fluctuating orientation of π_{osc} . Laser power :12 mW.

An alternate analysis of the same dynamics was carried out from the photodiode signal, Fig. A-III.16.

The change in plane of oscillation revealed in the above plot is accompanied by modulation in oscillation frequency. This modulation as it can be seen from the frequency time plot (Fig. A-III.16c) repeats itself. As the spectral content of such dynamics evolves in time, it is necessary to analyze the frequency content of the dynamics in time.

Fourier transform analysis of a time domain signal masks the time evolution of the physical phenomenon, as it provides the spectral content of the signal integrated over time. One way of avoiding this is by calculating the time-frequency distribution of a signal, using short time Fourier transform (STFT) analysis. This is achieved by using a sliding window function that moves with time, and calculating the Fourier transform of the function within the window. Mathematically, given a time series $x(n)$, the STFT at time n and frequency ν is given as :

$$x(n, \nu) = \sum_{m=-\infty}^{\infty} x(m) \cdot W(n-m) e^{-j2\pi\nu m} \quad , \quad (\text{A-III.2})$$

where $W(n)$ is the window function and the window $x(m) \cdot W(n-m)$ is a short time section of the signal $x(m)$ [Quatieri 2002].

Below we report our analysis of the dynamics of the system through a joint time-frequency representation of the signal. The STFT (Fig. A-III.16 c) shows how the frequency of the particle changes with time.

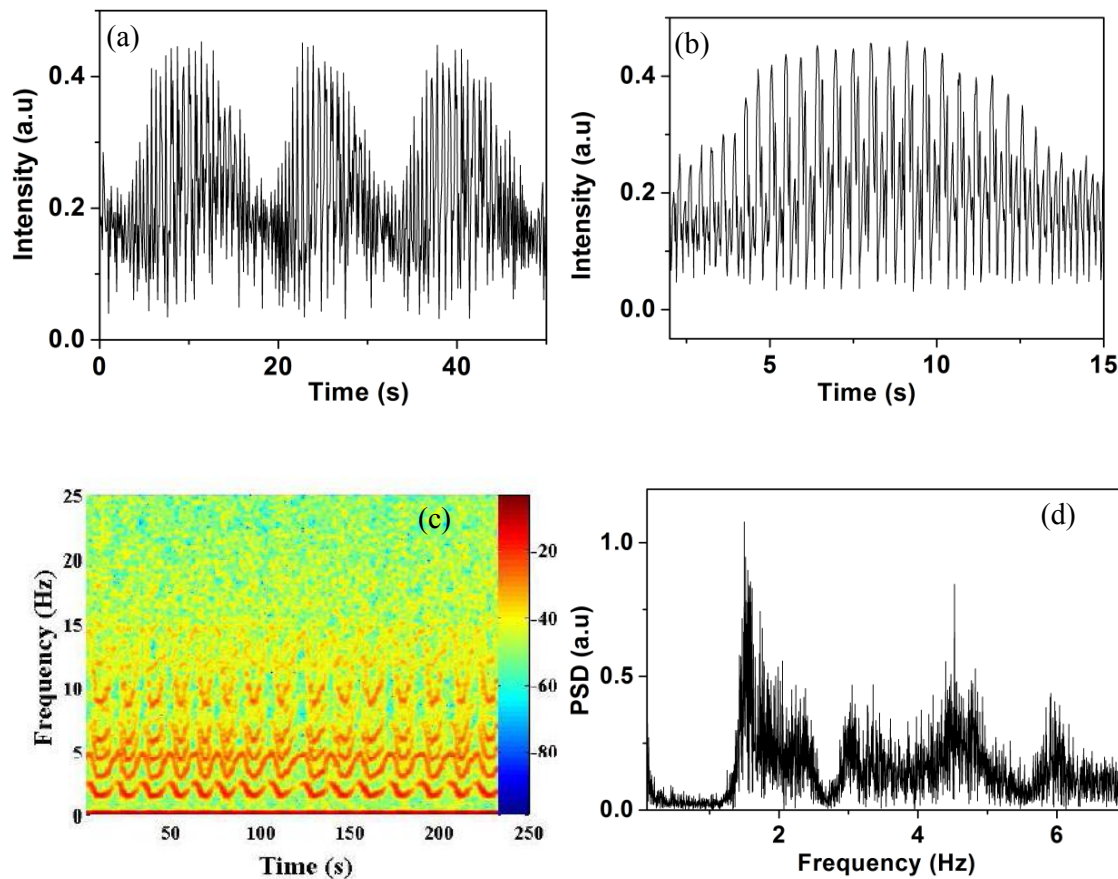


Figure A-III.16: A photodiode signal for a non-symmetric ellipsoidal particle, $k_1=4.2 \pm 0.05$, $k_2 = 4 \pm 0.05$. (a): time domain signal with modulated amplitude of oscillation. (b): short time domain signal (zoom over a few seconds). (c): Frequency time plot (spectrogram) of the signal. It shows the time modulation in frequency. (d): PSD of the whole signal. Note the broad range of the frequencies involved in the dynamics of such particles.

We carried out many more observations with a variety of elongated non symmetrical particles, and obtained a whole wealth of complex oscillation dynamics, which we analyzed with specific tools of non linear dynamics analysis. This work is the matter of Section A-IV.

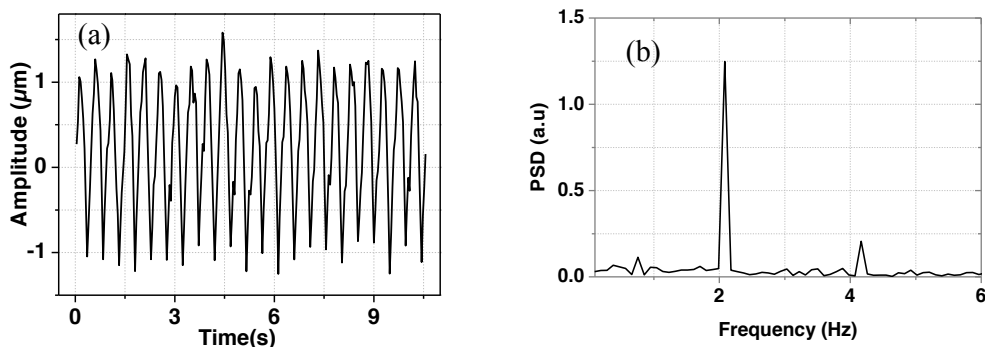
A-III.2b.3: Damped oscillations, resonance and influence of polarization

Short (small- k) ellipsoids simply align with their symmetry axis on the laser beam axis, while longer ones ($k > k_C \approx 3.0$) show sustained oscillations. k_C is the threshold of the bifurcation between static equilibrium and oscillations. In this paragraph, we deal with the case of “sub-critical” particles, meaning ellipsoids whose aspect ratio is only slightly less than k_C . Such particles are below the bifurcation threshold and then do not permanently oscillate, but they are very “susceptible”: when such a particle is slightly pushed away from the beam axis in x or y , it comes back to vertical equilibrium through a few damped oscillation cycles⁴. The damped oscillations occur at a characteristic frequency $\nu_{car}(P)$ that depends on the laser power, similarly to sustained oscillations above k_C .

The perturbation in x or y can be achieved very simply by moving the glass cell a little bit aside, using the translation stages. An alternate and equivalent method consists in shifting the laser beam over a few microns in either x or y by means of the galvanometric mirrors. If the beam is moved back and forth periodically, at frequency ν_{scan} , we excite oscillations of the particle. We can then measure the amplitude (A) of the forced oscillation, which is the response of the particle to the perturbation at this frequency.

Resonance in the oscillation of levitated ellipsoids

In this experiment, we varied the scan frequency and measured $A(\nu_{scan})$. Fig. A-III.17 below indicates the characteristics of the beam motion. The beam was scanned by about $\Delta x = \pm 1 \mu\text{m}$ along x . The graphs represent the horizontal motion of the laser spot in the top view, from video analysis.



⁴ This behavior is reminiscent of pretransitional effects in second-order phase transitions (e.g. the magnetic susceptibility in the paramagnetic state becomes very large close to the Curie temperature).

Figure A-III.17: Oscillation of laser light stirred by a couple of mirrors. (a) Time domain. (b) The corresponding PSD shows that the driving frequency is 2.1 Hz.

In this example, scanning was operated at 2.1 Hz. The corresponding spectral density is displayed in panel (b).

Once a particle of appropriate aspect ratio is picked and levitated to the top of the cell, then the levitating laser beam is scanned at constant power (here $P = 14$ mW), for different values of ν_{scan} . We then observe the induced particle oscillation. The latter is characterized by two amplitudes, one in translation, $A_{trans}(\nu_{scan})$, and one in tilt angle, $A_{rot}(\nu_{scan})$. An example of the induced particle motion due to laser scanning is shown below, Fig. A-III.18 & 19. In Fig. A-III.18a, the amplitude of oscillation of $\sim 3\mu\text{m}$ is the response to a driving frequency $\nu_{scan} = 1.4$ Hz.

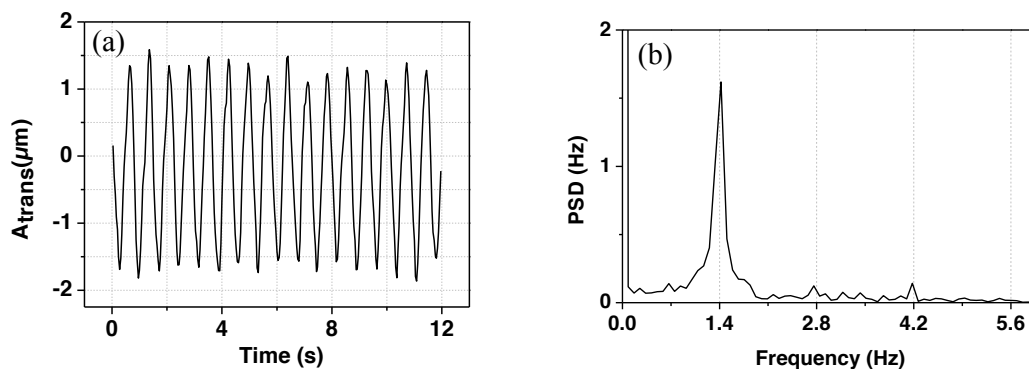


Figure A-III.18: Oscillation (x motion) of an ellipsoidal particle, $k \sim 3$, excited by laser beam scanning. (a) Time series of the particle oscillation showing $A_{trans} \sim 3\mu\text{m}$, at $\nu_{scan} = 1.4\text{Hz}$. (b) The corresponding power spectrum.

Changing the driving frequency systematically causes a change in the amplitude of oscillation (both translational and rotational). Repeating the experiment at different driving frequencies gives a peak in oscillation amplitude, revealing a resonant response. The resonance frequency is about 2.1 Hz for the tested particle. Fig. A-III.19 below shows the particle translational and rotational responses at this frequency. Signatures of the resonant responses are displayed in Fig. A-III.20.

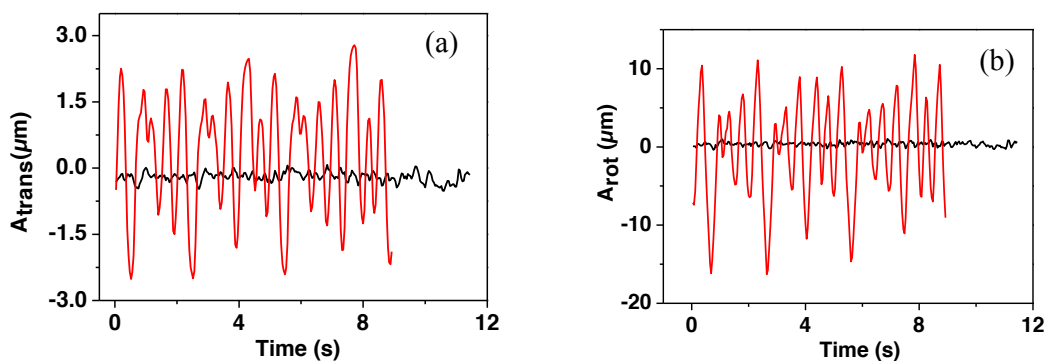


Figure A-III.19: The state of the particle before (black line) and after (red line) scanning the laser light at $v_{\text{scan}} = 2.1$ Hz. (a) represents translational oscillations while (b) represents rotational oscillations.

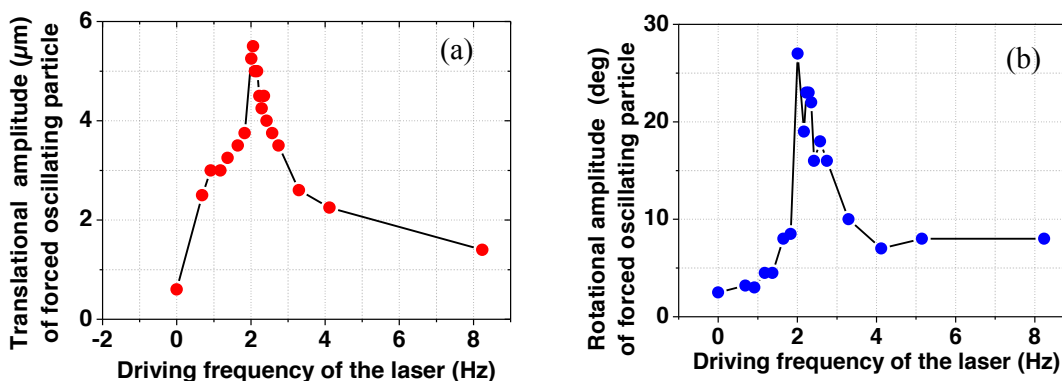


Figure A-III.20: Resonance in oscillation of sub-critical ellipsoids. (a) translational resonance. (b) rotational resonance.

Effect of light polarization on the dynamics of the ellipsoid

Up to now, we have not specified the polarization state of the laser beam. As we move the laser beam in a given direction (x), there may be a difference in the particle response according to whether the beam is polarized either parallel or perpendicularly to x . Potential

differences may show up in the resonance frequency, in oscillation amplitudes and in the orientation of the oscillation plane (Π_{osc}).

In ordinary experiments, the polarization of the beam is linear ($\|\hat{\mathbf{e}}\|$). We looked for polarization effects on the particle oscillation patterns by rotating $\hat{\mathbf{e}}$. The test was carried out with a few sub-critical ellipsoids. We noticed no feature that definitely depended on the polarization state. More precisely, there was no definite correlation between the plane of oscillation (Π_{osc}) and the polarization, and similarly with the amplitudes. See the example displayed below (Fig. A-III.21). We thus conclude that polarization effects are weak, meaning not measurable within the resolution of these observations. Recall that the ellipsoids are only very weakly birefringent.

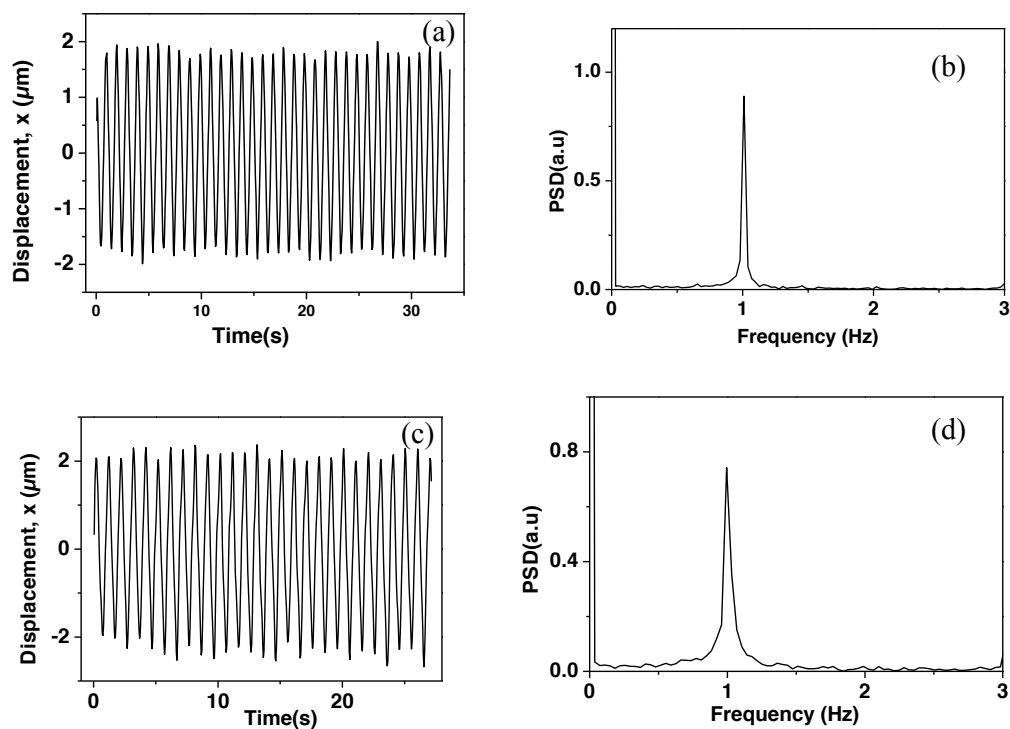


Figure A-III.21: *The particle considered here has aspect ratio 3 and is subjected to laser power of 13 mW. (a) Time series for linear polarization, electric field along x axis. (b) The corresponding PSD. (c) Time series for linear polarization, electric field along y axis. (d) corresponding PSD.*

A-III.2b.4: State diagram ($Z=0$)

The state diagram summarizes the dependence of the dynamical state on particle shape parameters. Fig. A-III.22 gathers the experimental data by specifying only k_1 and k_2 as control parameters, since the laser power is not essential. Note that the displayed diagram only holds for ellipsoids whose centers are about in the beam-waist plane ($z=0$). The top right quarter corresponds to prolate ellipsoids. Increasing $k_{1,2}$ denotes particles which are more and more elongated. Points close to the diagonal indicate particles that are about cylindrically symmetrical, while those well outside of the diagonal are far from symmetrical. The bottom left quarter corresponds to oblate ellipsoids. In this case, small $k_{1,2}$ values refer to particles that are very flat.

Solid red circles correspond to particles which are stably trapped by the laser beam. In this class, nearly symmetrical particles simply do not move (apart from very small Brownian fluctuations), and stay in on-axis configuration.

The transition to oscillations happens at $k_{1,2} \cong 3$ (prolate) and $k_{1,2} \cong 0.33$ (oblate). Solid black squares correspond to sustained dance while solid blue triangles correspond to “pre-transitional”, or “sub-critical”, behavior, meaning that such ellipsoids ultimately come to rest but are very sensitive to excitation (§A-III.2b.3).

Oblate ellipsoids show behaviors that are similar to prolate particles. Particles with $0.33 < k < 1$ stays static in the beam, whereas the highly flattened ones ($k < 0.33$) show sustained oscillations in the beam. Oblate ellipsoids near the critical aspect ratio also exhibit “pre-transitional” behavior.

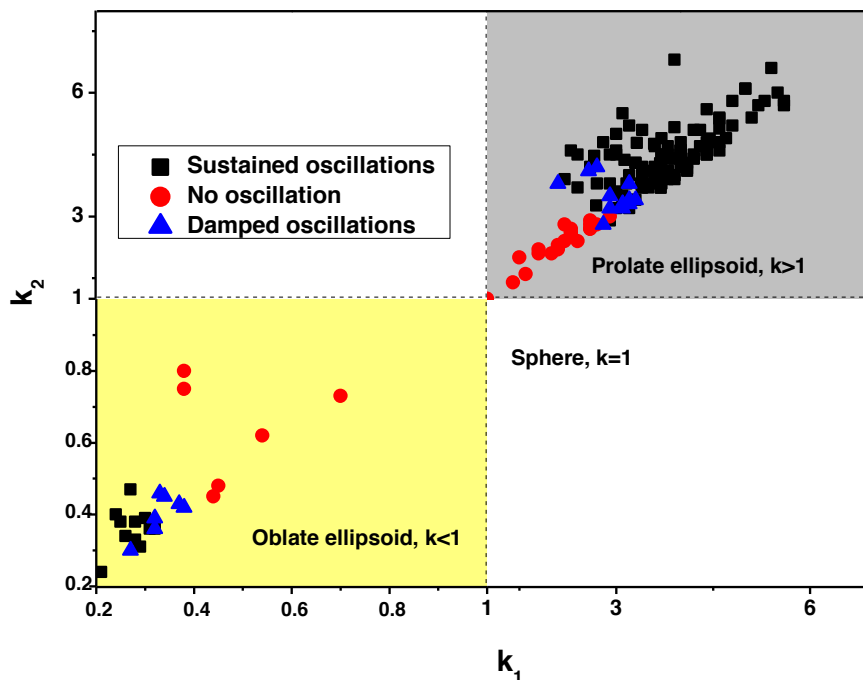


Figure A-III.22: State diagram, summarizing the dependence of the dynamical state on particle shape parameters. All data of the diagram correspond to $Z=0$, i.e. particle centers were approximately at the altitude of the laser beam waist.

A-III.3 Particle in contact to water-glass interface, at variable Z

A Gaussian beam has minimum in beam diameter at its focused point, called the beam waist ($2\omega(Z=0)=2\omega_0$, Fig. A-III.23); and the beam diverges away from this point. In this section we shall investigate the effects of changing the beam diameter on the dynamics of levitated ellipsoids.

From the Gaussian beam diffraction law, $\omega(z) = \omega_0 \sqrt{1 + z^2/z_R^2}$ (Eq. (1.6)), we can calculate $2\omega(Z)$ for varying Z . Values relevant to the experiments are displayed in the table below.

$Z(\mu\text{m})$	Beam diameter (μm)
0	1.95
10	2.72
20	4.26
30	6
40	7.77
50	9.67

60	11.52
70	13.39
80	15.26
90	17.14

Table 2: The beam diameter values (μm) for the corresponding Z values (μm). We used the values: $\omega_0 = 1.3 \mu\text{m}$, $z_R = \pi\omega_0^2/\lambda = 13.8 \mu\text{m}$. Note that $2\omega(Z)$ is even in Z .

In our experiments, the particle is always in contact to the glass cell top surface, and observation is focused in this plane. We vary Z by shifting the laser beam waist vertically to a position either below ($Z > 0$) or above ($Z < 0$) the observation plane. Consequently, the particle is exposed to increasingly wider beams when $|Z|$ is increased, see Fig. A-III.23.

We start (§A-III.3a) with a description of what happens when a particle, initially at the beam waist, is moved to progressively higher $|Z|$ (either >0 or <0). As we will see, a moderate increase in $|Z|$ do not considerably modify the particle behavior, but it does change details of the dynamics. The second paragraph (A-III.3b) describes the drastic transition (vertical to horizontal equilibrium) that occurs when the beam width becomes comparable to the particle (large) size.

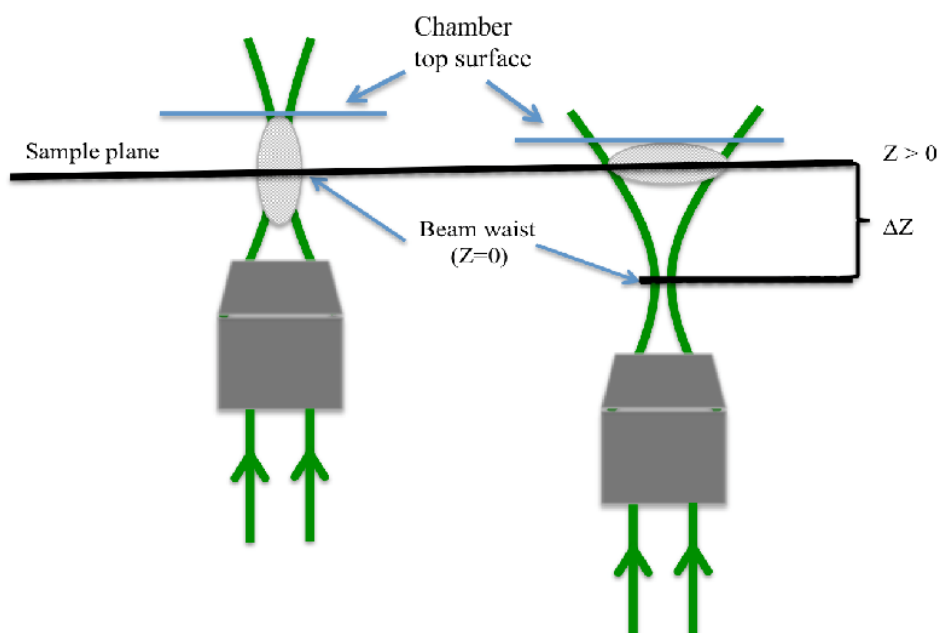


Figure A-III.23: Particle orientation for different beam widths. Left: ellipsoidal particle located at the beam waist. In average, the long axis of particle is aligned parallel to the beam

axis. Short particles ($k < 3$) keep locked on beam axis, while longer ones ($k > 3$) oscillate. Right: the same particle, when far enough from the beam-waist, switches to horizontal static equilibrium.

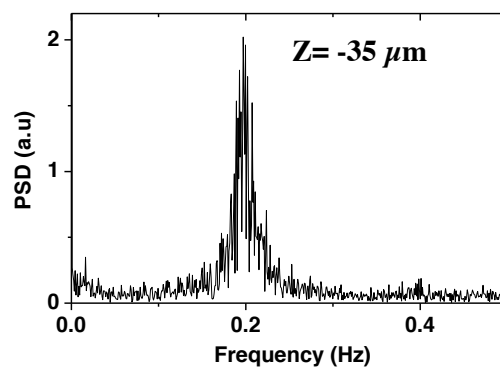
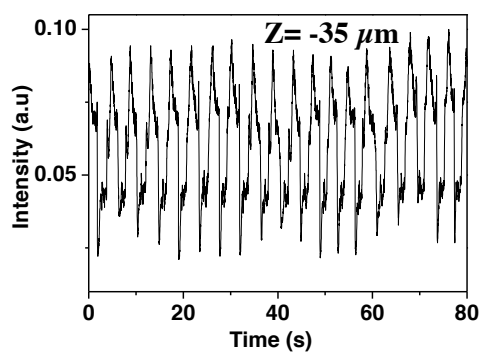
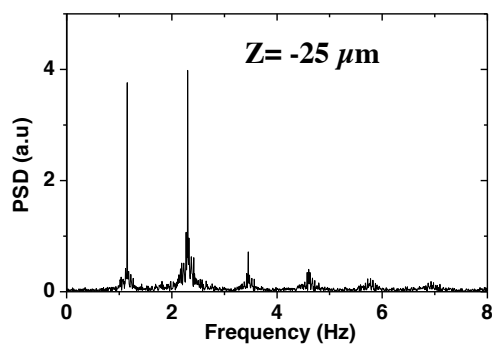
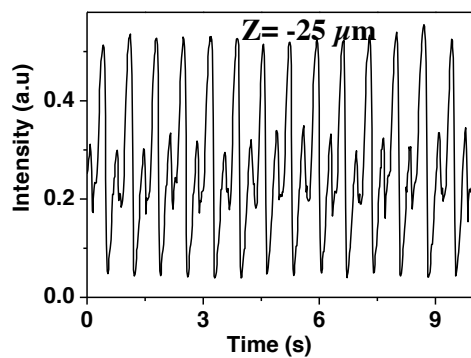
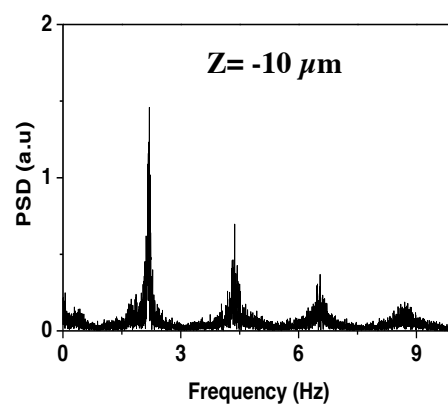
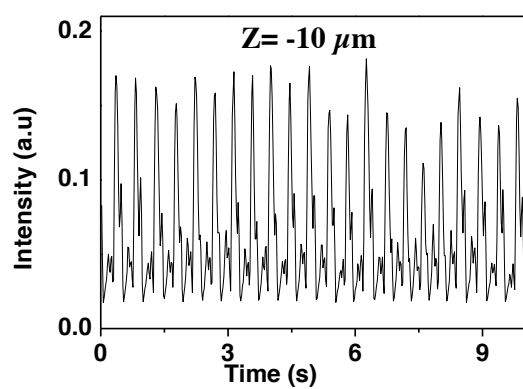
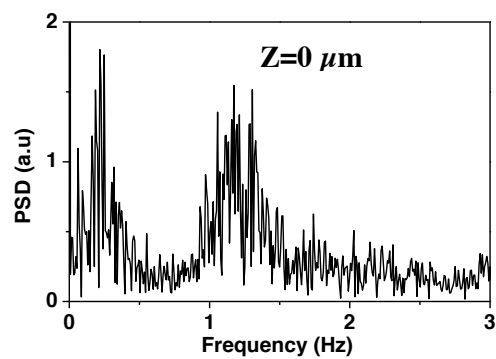
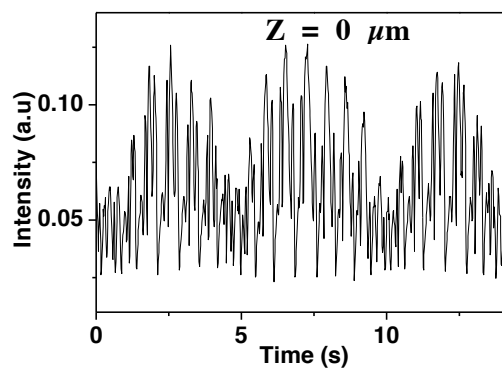
A-III.3a: Influence of varying beam diameter on particle oscillation

In this paragraph, we only consider prolate ellipsoids, which are long enough to oscillate at $Z=0$. Our goal is just to provide a few qualitative trends about the influence of the beam diameter, and possibly beam divergence, on oscillations. We will come back to some of the examples reported below in Section A-IV, to provide more elaborate, quantitative descriptions of the particle trajectories.

Starting with a particle that oscillates at $Z=0$, and increasing Z , we systematically observe a gradual slowing down of the ellipsoid oscillation, down to no oscillation at all when Z is large enough. This trend is not surprising, if we realize that only a small fraction of the beam power is intercepted by the particle at large Z . For instance, $2\omega(Z = 90 \mu m) = 17.14 \mu m$, comparable to the particle long axis length. Consequently the effective power felt by the particle decreases with Z , and so does the oscillation frequency.

More importantly, changing Z has an impact on the qualitative features of the particle dynamics. As we will see from the data below, increasing the beam width may change the particle dynamics from irregular to approximately periodic or reversely.

We start with two examples (I and II) corresponding to the type of oscillatory motion discussed in §A-III.2b.2. As we explained, this kind of dynamics is observed at beam waist for slightly non-symmetrical moderate aspect ratio ellipsoids. As a general feature of such particles, the direction of the oscillation plane fluctuates, and the photodiode signal is clearly non periodic. In I (Fig. A-III.24), Z is negative, meaning that the particle is located upstream of the beam waist. The time series changes from modulated amplitude type of motion at the beam waist to quasi-periodic motion at broader beam width. This trend is more evident from the Fourier analysis where the broadband spectrum at $Z=0$ changes to well discernible discrete peaks (e.g at $Z=-25$).



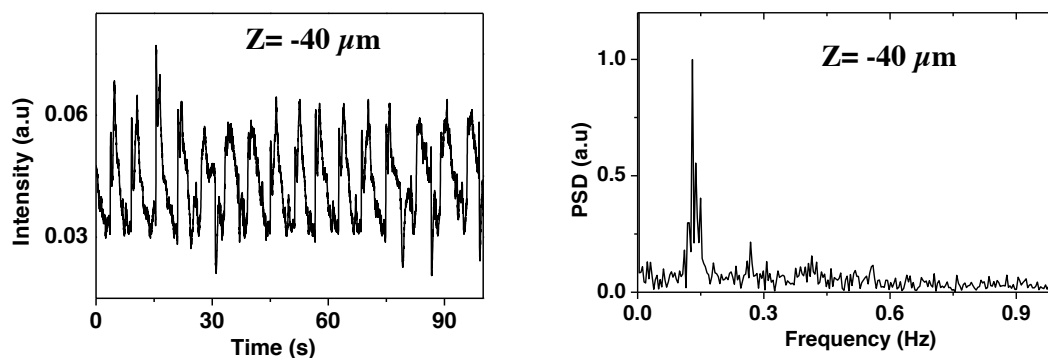
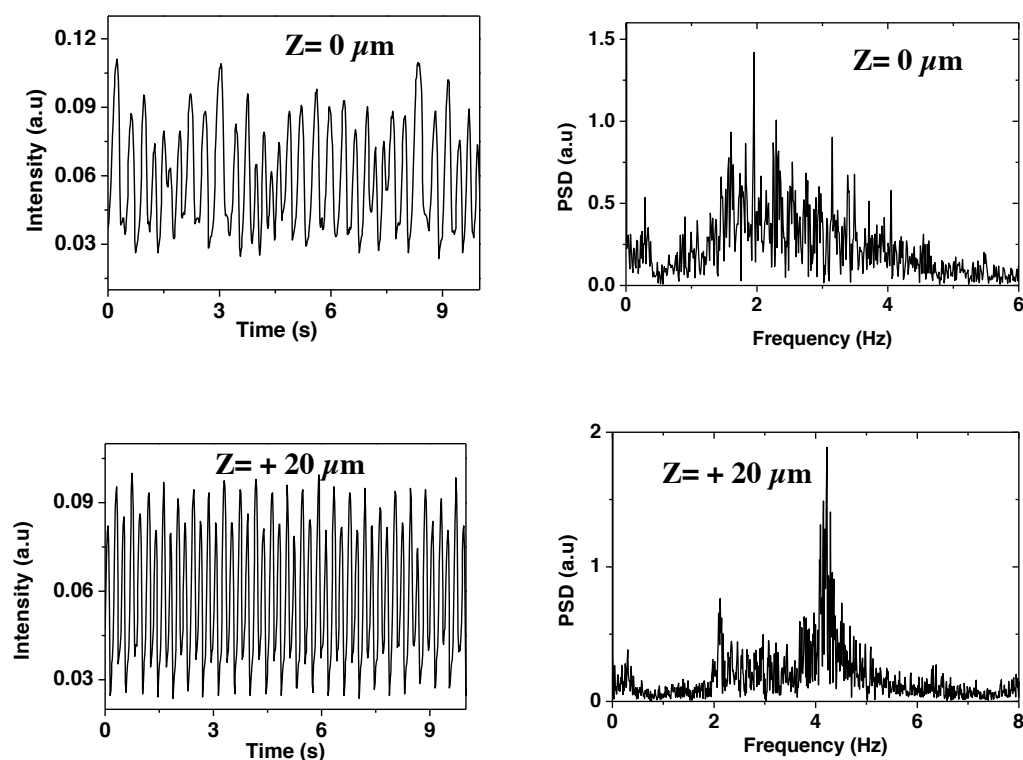


Figure A-III.24: Example I: oscillating non-symmetrical ellipsoid ($k_1=4$, $k_2=3.6$) at different beam widths. Left column: Time series signal from photodiode. Right column: corresponding Fourier power spectrum density.

A similar evolution is observed in the next example (II, Fig. A-III.25), now with $Z > 0$. The irregular dynamics recorded at the beam-waist changes to more regular dynamics when Z increases, with a concomitant stabilization of the oscillation plane. The sequence is limited to $Z \leq 75 \mu\text{m}$; beyond this value, the particle switches to horizontal equilibrium.



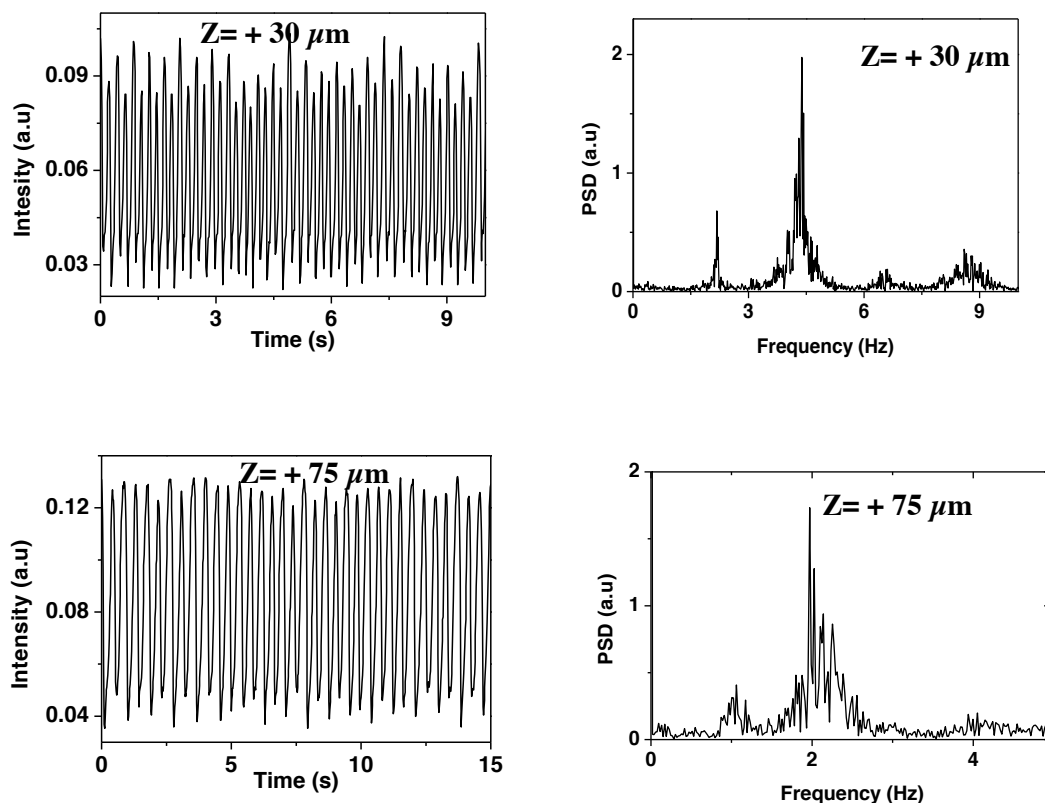
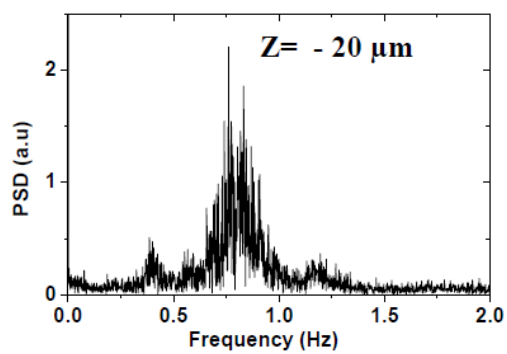
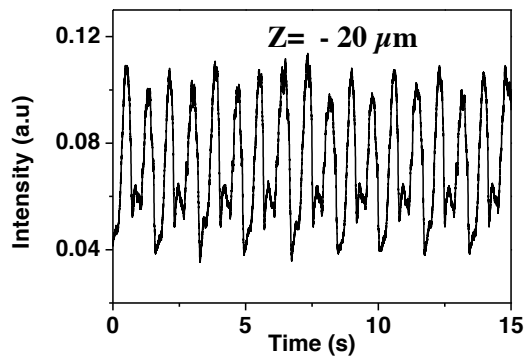
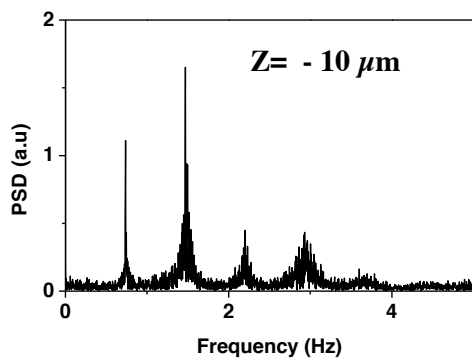
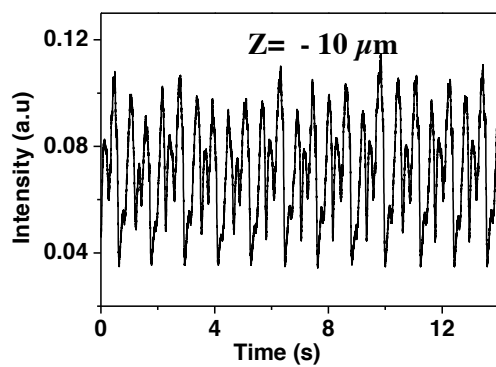
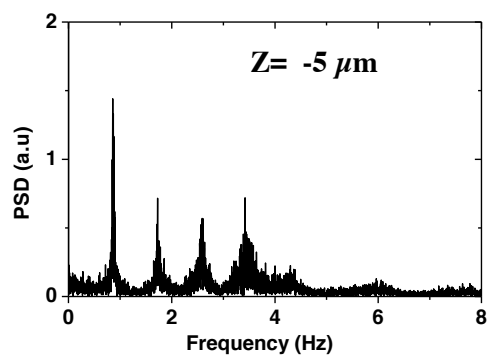
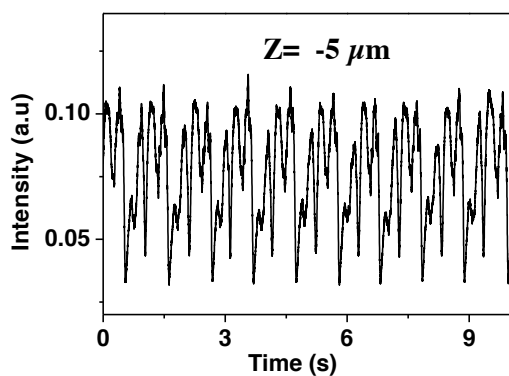
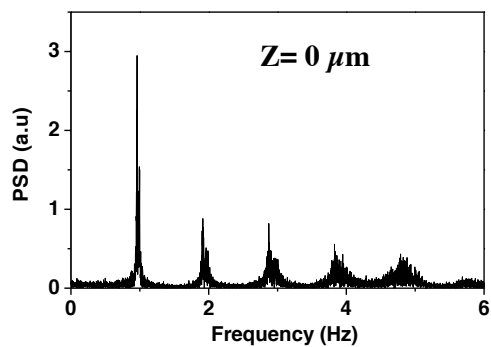
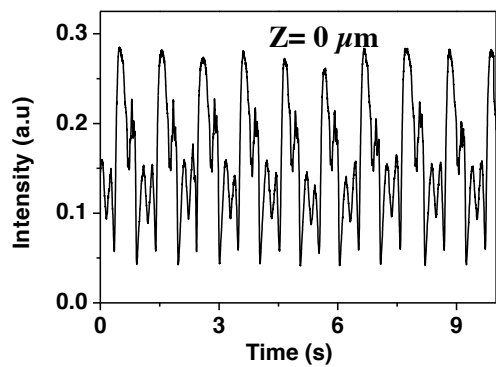


Figure A-III.25: Example II: oscillating ellipsoid at different positive Z values ($k_1=4.1$ and $k_2=3.8$). Time series photodiode signals (left column) and corresponding power spectrum densities (right column). Laser power: 10 mW.

The following third (III, Fig. A-III.26) and fourth (IV, Fig. A-III.27) examples consist of groups of ellipsoids whose motions do not involve significant fluctuations of the oscillation plane (unlike the above two examples). Here the change in oscillation dynamics due to varying beam width is less pronounced at moderate Z , and opposite at large Z , meaning that increasing the beam width leads to more *irregular* dynamics.



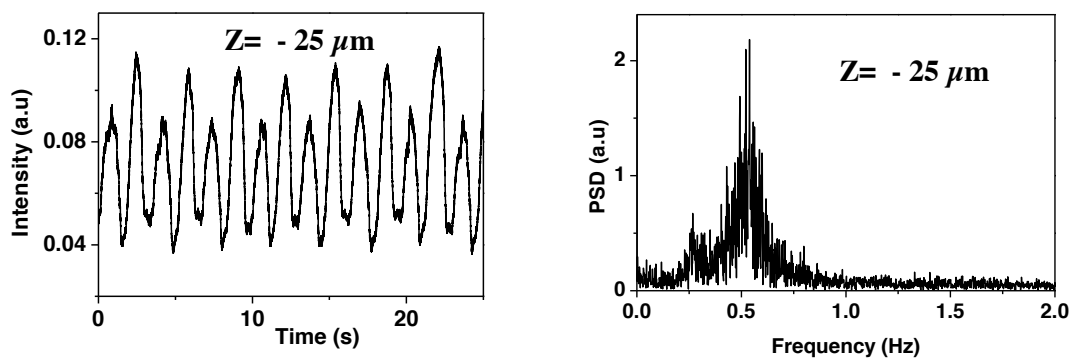
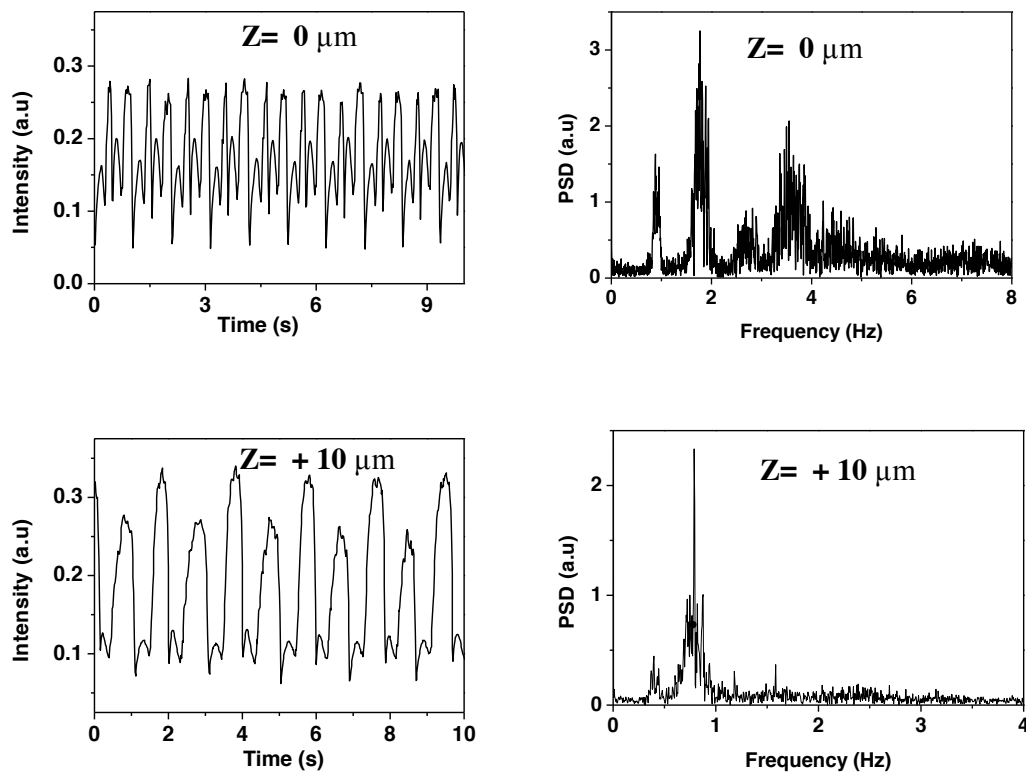


Figure A-III.26: Example III: oscillations of a symmetrical ellipsoid ($k=4$) at various negative Z values. Time series photodiode signals (left column) and corresponding power spectrum densities (right column).



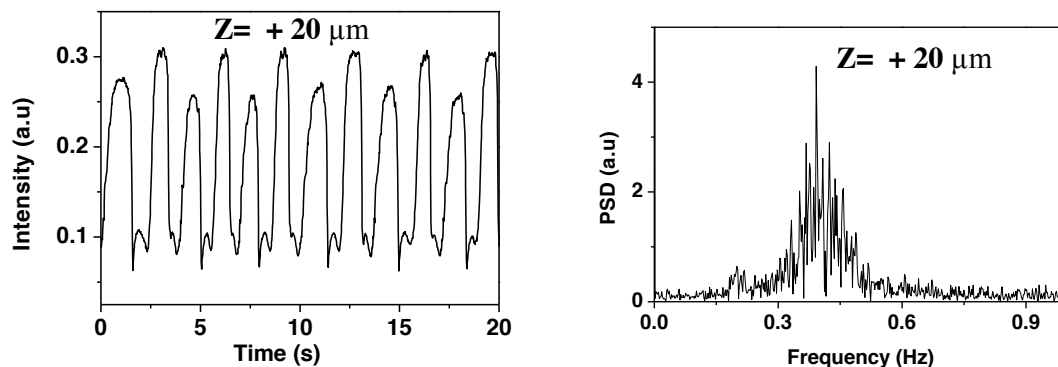


Figure A-III.27: Example IV: oscillations of a slightly non-symmetrical ellipsoid ($k_1 = 4.18$ and $k_2 = 4.11$) at three different positive Z values. Time series photodiode signals (left column) and corresponding power spectrum densities (right column).

A-III.3b: Vertical to horizontal transition

The Vertical-to-Horizontal (V-to-H) transition occurs at large Z , when the beam diameter becomes broader. Observations can be summarized as follows:

- i. Short aspect ratio ellipsoids ($k < 3$) align their long axes along the beam axis at the beam waist ($Z=0$), and flip horizontal at large beam width. Note that these particles do not oscillate in both cases.
- ii. At the beam-waist, longer ellipsoids ($k > 3$) still keep vertical, but only in time average, since they oscillate around the beam axis (z). At large Z , the same particles switch to horizontal static equilibrium, similarly to short ellipsoids.

The transition is illustrated below (Fig. A-III.28). The photos are top views, showing an elongated particle ($k \approx 4.9$). Z was initially tuned to $Z_i \approx 50 \mu\text{m}$, a configuration where the particle was permanently oscillating. The sequence shows the response of the particle dynamics to an increase in Z , up to $Z_f \approx 80 \mu\text{m}$. The particle still goes through a few slow oscillations (top row) and then comes to rest in horizontal equilibrium (bottom row).

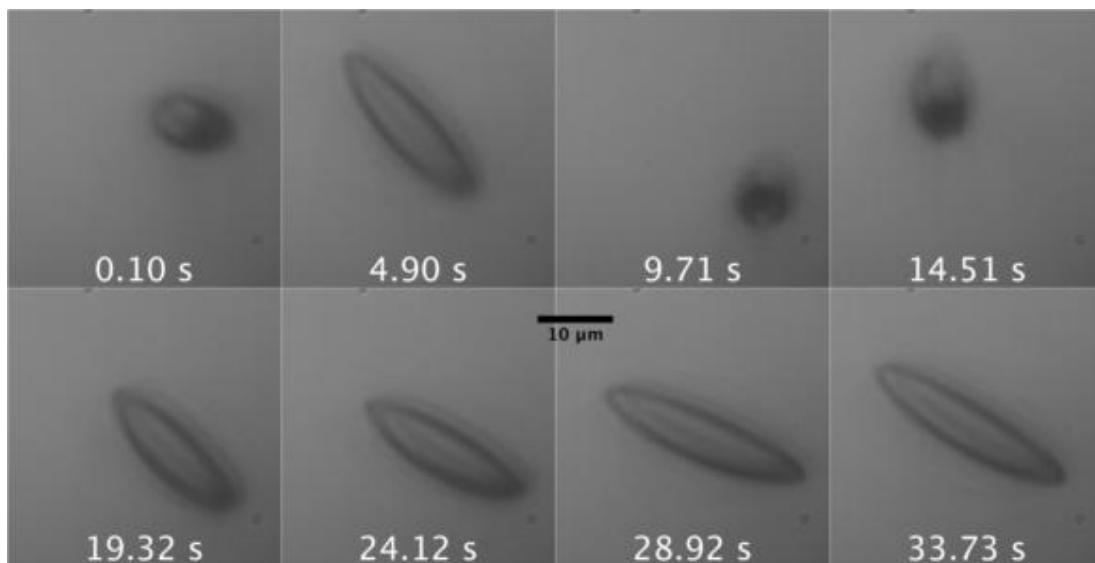


Figure A-III.28: Consecutive images of a prolate ellipsoid showing a transition to horizontal orientation. Once the particle is lying flat on the interface, it does not show any form of sustained oscillation.

The V-to-H transition, i.e. the change in orientation of spheroids from vertical to horizontal alignment in response to increasing beam width, holds for both oscillating and non-oscillating prolate ellipsoids. But the particular Z value, Z_{VH} , and the corresponding beam width, $2\omega_{VH} = 2\omega(Z_{VH})$, which causes the particle to flip horizontal, vary from particle to particle; see the few examples in the table below. To help comparison, the table includes the particle length ($2a$) and the beam diameter $2\omega(Z_{VH})$.

k_1	k_2	Z_{VH}	$2a$	$2\omega(Z_{VH})$
2	1.8	- 70 μm	17.6	13.5
4.3	3.5	\sim -100 μm	27	19
4.1	3.8	\sim +90 μm	28	17
2.45	2.45	+70 μm	21	13.5
4.2	3.6	+80 μm	26.6	15

Table 3: Few examples for V-H transition.

We shortly investigated the influence of the beam polarization on the horizontal equilibrium. The conclusion is similar to that drawn for oscillating states, i.e. we did not notice any clear correlation. H configurations of prolate ellipsoids were randomly oriented.

A-III.3c: Summary

Whatever the type or shape of the particle, the oscillation disappears for large enough beam width. Thus, the necessary conditions for the oscillations to exist are:

- the particle should be elongated enough ($k > 3$),
- the beam width should not be too large ($Z < |Z_{max}| = Z_{VH}$)

whereas the type of dynamics is controlled by :

- the symmetry and aspect ratio of the particle
- the beam width.

The above statements are gathered into the graph below, Fig. A-III.29. Note that the dotted lines are only indicative. Boundaries between the different regimes have not been accurately determined yet.

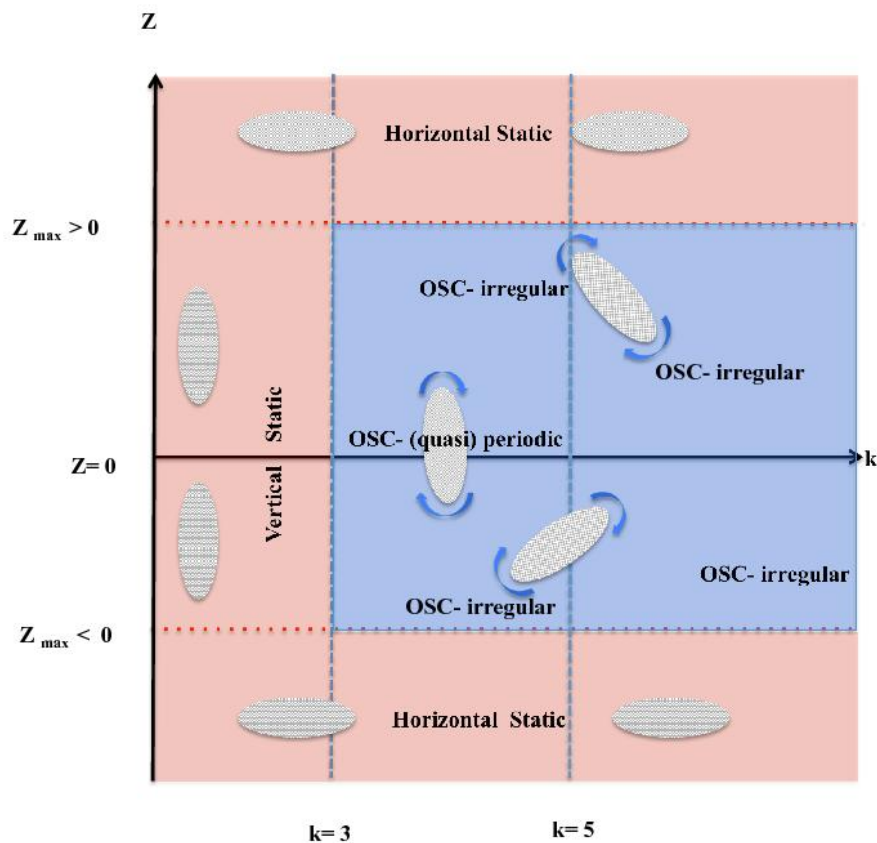


Figure A-III.29: State diagram for different dynamics of prolate ellipsoids. Here k is simply the average of k_1 and k_2 . OSC means “oscillations”.

In Fig. A-III.29, the sketches in the column at left represent static configurations of short prolate ellipsoids ($1 < k < 3$), or oblate particles with $0.4 < k < 1$, approximately. Particles of both categories can be trapped in static *vertical* equilibrium at moderate Z . Here “vertical” means that the particle lies with its long axis along the beam axis. This observation is in line with the prediction by S.H. Simpson and S. Hanna [Simpson 2007] and others, as discussed in A- I. Particles that may be termed “thin”, because they are long (large k) or very flat (very small k), oscillate in a more or less complicated manner. At large $|Z|$, all particles lie flat along the top glass surface.

A-IV: Analysis of oscillations

The present Section is devoted to an in-depth analysis of some of the temporal signals reported in section A-III.3. Most generally, the system constituted by the solid particle has 6 degrees of freedom, namely 3 translational variables and 3 angles. Below we restrict the analysis to the cases where the particle is in contact to the top surface; consequently we are left with 5 variables (x , y , and 3 angles), which we may gather into a 5-coordinate vector \mathbf{s} . Equations that govern the motion of the particle may be cast in a simple form:

$$\boldsymbol{\zeta} \cdot \dot{\mathbf{s}} = \mathbf{F}(\mathbf{s}) \quad (\text{A-IV.1})$$

Here \mathbf{F} is a generalized force, including the force and torque components due to laser radiation pressure. The left hand side, $\boldsymbol{\zeta} \cdot \dot{\mathbf{s}}$, is the a generalized hydrodynamic drag force due to translational and rotational motion of the particle inside water. $\boldsymbol{\zeta}$ is the friction matrix, whose coefficients are proportional to the water viscosity (η), and $\dot{\mathbf{s}}$ is the generalized velocity of the particle. The above equation is valid in the Stokes limit, where inertia is negligible (see page 41).

At this stage, we have no quantitative knowledge of how \mathbf{F} depends on \mathbf{s} , but we can be sure that the dependence is strongly nonlinear. We base this statement on well established results about spherical particles; see e.g. [Ren 1994]. Then Eq. (A-IV.1) is a set of non linear ordinary differential equations, of dimension $d=5$. Control parameters are the beam characteristics, which are determined by ω_0 and z , and the particle sizes (a, b, c). The latter may be replaced by the aspect ratios $k_{1,2}$, since all particles used in the experiments are derived from the same type of polystyrene sphere. Based on experimental observation, we may anticipate that the dynamical system (DS) Eq. (A-IV.1) has solutions of different types, namely fixed points (corresponding to a stably trapped particle), limit cycles (periodic motion) and possibly deterministic chaos (non periodic motion).

The purpose of this Section is to examine experimental time series and identify the attractors corresponding to such different types of motion, using standard tools of nonlinear analysis. Below we report the results that we obtained using the TISEAN package, which is a widely used and freely available analysis tool (http://www.mpipks-dresden.mpg.de/~tisean/Tisean_3.0.1/index.html). We do not provide an introductory overview of nonlinear dynamics in general, a task that would be much beyond the volume of this Section and our own expertise. The interested reader is of course referred to the abundant literature in this field; see e.g. [Hegger 1999] and the many useful references therein. We opt for a simply practical

presentation, meaning that we only shortly describe the main steps of the analysis and provide results for different values of the control parameters.

A-IV.1 Phase space reconstruction

The full experimental characterization of the real DS involves measuring 5 parameters, which generate a trajectory in a 5-dimensional phase space. In reality, we can at most measure 3 of them, namely x , y and θ , using video means and image analysis (A-II, A-III). Note that the corresponding time series are strongly limited in information, because the sampling frequency is upper bounded by the available video rate (< 40 Hz). Conversely, the photodiode signal, $I(t)$, can be sampled up to 10^5 Hz, but it only provides a 1-dimensional information. Of course, the bare $I(t)$ signal cannot properly reflect the 5-dimensional trajectory of the real DS. Fortunately, however, the missing information can be recovered, or “unfolded”, from time delayed copies of the original signal if certain requirements are fulfilled. The method, called the “*method of delays*”, is one of the most important and widely used techniques for phase space reconstruction.

Basically, we construct a time-delay series, namely the m -dimensional vector $X(t) = [I(t), I(t+\tau), \dots, I(t+m\tau)]$, with $m \leq d$. The integer m is the “embedding dimension”, and τ is the delay time. If the value of τ is “adequate” and if m is large enough, the obtained m -dimensional trajectory and the corresponding attractor are known to be equivalent to their real counterpart in the full d -dimensional phase space. Here the equivalence essentially means that both representations have the same topological properties [Bergé 1986, Thomson 1986].

Choice of the delay time: An adequate value of the delay time τ is such that the time delayed variables $I(t), I(t+\tau), \dots, I(t+m\tau)$ are about independent. The latter criterion may be satisfied by considering the value of autocorrelation function that yields linear independence (zero autocorrelation) of coordinates. Numerically, this amounts to calculate

$$c(T) = \frac{\langle x(t)x(t+T) \rangle}{\langle x^2(t) \rangle}, \quad (\text{A-IV.2})$$

Thus, the delay time, τ , is the value of T such that $c(T)/c(0) \approx e^{-1}$ [Lai 2003].

An alternate and more elaborate technique, is based on the “mutual information” function $S(\tau)$ that non-linearly correlates the signal with itself, see Eq. (4) in [Hegger 1999]. A well-marked minimum in $S(\tau)$ provides a good choice for the delay time. Both methods are complementary and are routinely used in parallel to determine the most appropriate delay time.

Choice of the embedding dimension: m should be ≥ 3 to reveal chaotic behavior through the structure of the associated strange attractor. One may be tempted to directly choose $m=3$, to limit the volume of data to be handled and simplify graphic representation. Whether this choice is acceptable may be verified through general techniques to determine the minimal sufficient embedding dimension. One of them, called “False nearest neighbors” [Kennel 1992], is available in the TISEAN package and was used for our application. The principle, described in [Hegger 1999], is based on the fact that projecting the real trajectory onto a low dimensional space brings together regions of the attractors that are otherwise well separated, thus generating false neighbors. The methods amounts to detecting false neighbors and counting them when m increases from 1 up to d .

The figure below is an illustration of the above procedures to determine τ and m . In this example the delay time is suggested to be 190 ms and the false-neighbor test for $m=3$ is positive.

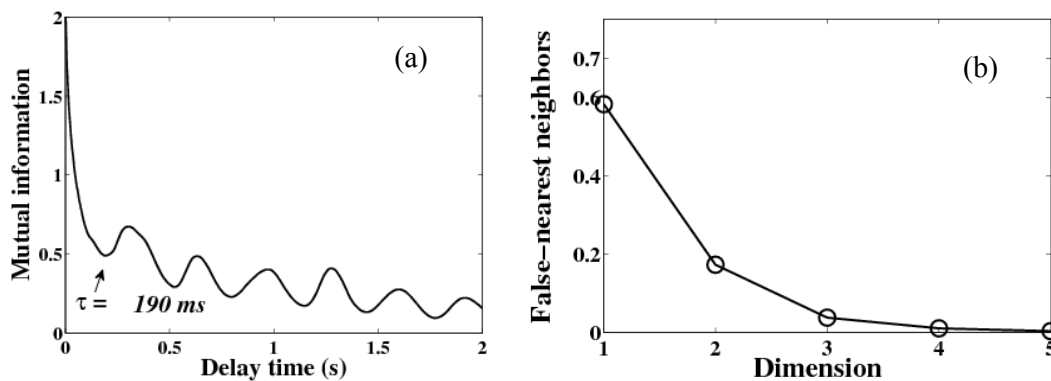


Figure A-IV.1: A photodiode signal of an oscillating ellipsoid ($k_1=4.5$, $k_2=4.1$, $Z=0$). (a) Determination of the delay time using mutual information method. The test suggests $\tau=190\text{ms}$. (b) Fraction of false neighbors, versus the embedding dimension. In this example, the false-neighbor test for $m=3$ is acceptable.

We found that $m=3$ was acceptable with many other time series that we examined, but not with all of them. In a few cases, the test even indicated $m > 5$, a definitely non physical result!

The test should then be taken with some reservation. In cases where the test indicated $m=4$ or 5, we brought the reconstructed trajectories back to 3-dimensional versions using projections. The problem of finding “adequate projections” is handled by a dedicated tool in the TISEAN package, based on the “principal component” technique [Hegger 1999 and ref31 therein]. An example of projected trajectories, generated from our data, is displayed below (Fig. A-IV.2).

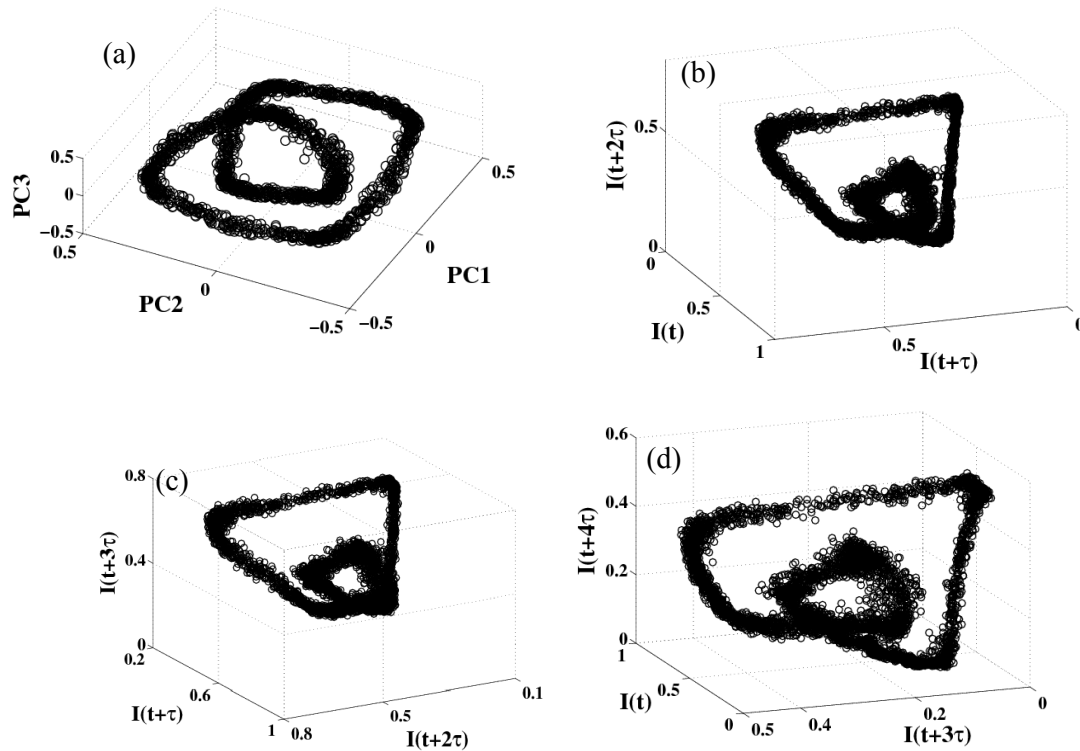


Figure A-IV.2 : Phase space representation of an oscillating ellipsoid ($k_1=4.1$, $k_2=3.8$, $Z=-25 \mu\text{m}$). (a) Constructed from three main principal components (PC1,2,3), this includes the three main contributors for the phase space. (b-d): Reconstructed phase space using delay method. (b): 3d phase space. (c): 3d projection of 4d phase space. (d): 3d projection of 5d phase space. All phase spaces are rotated at different angle to show their similarity.

Clearly, finding the adequate embedding dimension is not straightforward. In practice, we draw conclusions about the nature of particle dynamics from 3-dimensional trajectories, either directly generated from $[I(t), I(t+\tau), I(t+2\tau)]$ sequences, or from projections of higher dimension versions (Fig. A-IV.2 c & d). As we will see, this procedure turned out sufficient to reveal structures of chaotic attractors, a result that we take as an *a posteriori* argument that we did not miss the essential information about the nature of the dynamics.

Poincaré section: The Poincaré section is a graphic tool that helps determining the nature of the trajectory and of the related attractor. The general definition is the intersection of the trajectory with a given $(m-1)$ -dimensional hyperplane. In our application, with $m=3$, the section amounts to a collection of points inside a simple plane located somewhere across the trajectory. Of course the content of the section depends on the position and orientation of the cutting plane. A general recommendation is that the section should maximize the number of intersections, and maximize the variance of the data therein [Hegger 1999]. In practice, we used simple visual criteria: we chose the plane to intercept as much as possible of the trajectories, and we looked at the distribution of intersection points.

Typical features of Poincaré sections are:

- (i) A single point or a few isolated points: this indicates a periodic regime, with a limit cycle that ever cuts the plane through the same points.
- (ii) A closed curve: this happens with a quasi-periodic time series, resulting from two incommensurable frequencies.
- (iii) A cloud of points: the dynamics is non periodic.

For a non-periodic or chaotic motion, there is no repetition in the intersection points; and these no longer lie on a unique curve (as seen above for periodic and quasi-periodic cases) but generally spread “laterally” and form an “extended”, often layered-like, pattern such as the one shown in Fig. A-IV.3. The structure of this pattern can be either very complex or simple in appearance depending on the regime and the degree of resolution used to build it; see the textbooks by Bergé et al. [Bergé 1986] and Thomson & Stewart [Thomson 1986]. For our qualitative study, we will content ourselves by saying that an extended, “surface-like”, Poincaré section, with the characteristic layered structure as in Fig. A-IV.3, is typical of chaos in a dissipative DS.

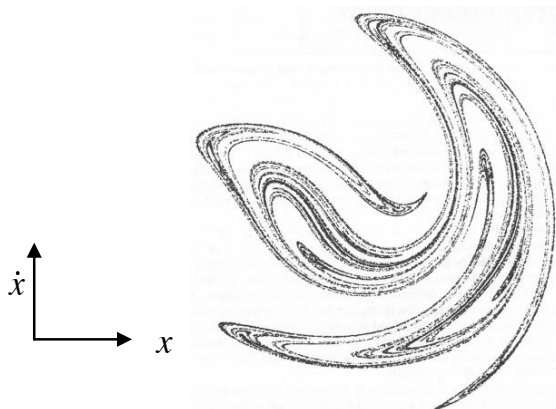


Figure A-IV.3: *High-resolution Poincaré section for one of Ueda's chaotic attractors [Ueda 1980].*

A-IV.2 Dynamics of ellipsoidal particles - Experimental results

In this section, we deal with the analysis of the experimental signals using the tools of the TISEAN package. A variety of dynamical regimes of the particle could be generated either by changing the ellipsoid aspect ratio or the beam diameter. In the next two paragraphs, we examine in detail the influences of these two parameters.

Of course we are interested in the cases where the particles undergo sustained oscillations, e.g. when $k_{1,2} > 3$ for $Z=0$. Nevertheless the “static” cases are a useful source of information as they may be exploited to estimate the importance of noise in general. Indeed the signal (either video images or photodiode) from a stably trapped particle is not strictly constant in time.

Signal fluctuations have an extrinsic part due to the measurement technique, i.e. the electronic noise in video images or in the photodiode signal. This is the source of stochastic errors, whose consequence is presumably not more than a finite amount of blur along the reconstructed trajectories. Indeed this source of noise is well visible as a statistical scatter of points in all figures displaying trajectories and Poincaré sections, see below.

The other source of randomness is intrinsic to the physical system, as it is related to the Brownian excursions of the particle in water. Strictly speaking, thermal noise modifies the DS equations into:

$$\zeta \cdot \dot{\mathbf{s}} = \mathbf{F}(\mathbf{s}) + \mathbf{b}(\mathbf{s}) \quad , \quad (\text{A-IV.3})$$

where $\mathbf{b}(\mathbf{s})$ is the random force at the origin of Brownian motion. In theory, if $\mathbf{b}(\mathbf{s})$ is large, the presence of the random force may have deep consequences on the dynamics of the system [Horsthemke 1984]. However, we always observed that random excursions of trapped particles were very small compared to laser driven excursions. We then presume that $\mathbf{b}(\mathbf{s})$ is “small”, with the consequence that it does not change the main features of the dynamics and that it only contributes a small amount of blur in the trajectories, similarly to electronic noise. Based on this reasoning, we conclude that measurements carried out with stably trapped particles may be exploited to estimate uncertainties in trajectories. In video images of axially trapped particles, we determined uncertainties in x, y, θ from the dispersion of the values obtained by the image analysis procedure. Similarly, we measured rms fluctuations in $I(t)$ for trapped particles and supposed that this quantity still represents the uncertainty in $I(t)$ in general.

A-IV.2a: Influence of ellipsoid aspect ratio

In this paragraph, we concentrate on the influence of k_1, k_2 , while the particle is maintained at $Z \cong 0$ (altitude of beam-waist). We start with examples of simple periodic motion discussed in A-III .2b.2 and move to irregular dynamics in the second part.

Periodic motion: Periodicity is suggested by the well-marked harmonic series in the power spectra, and is confirmed by the properties of 3-dimensional trajectories. The latter are obtained gathering x, y, θ data from video image analysis, or from the photodiode signal, using the above described phase space reconstruction techniques.

The 3d trajectory (x, y, θ) of the example displayed below is shown in Fig. A-III.10b. In Fig. A-IV.4 we show the reconstructed 3d trajectory for the same particle using the photodiode signal. The 3d phase space reconstructed from three main principal components shows a limit cycle, see Fig. A-IV.4a. The corresponding Poincare section shows isolated packets of points. The packet has size comparable to the error bar.

The limit cycle in both phase spaces (Fig. A-III.10b & Fig. A-IV.4a) and the closely packed points in the Poincare section lead to the conclusion that the motion is periodic.

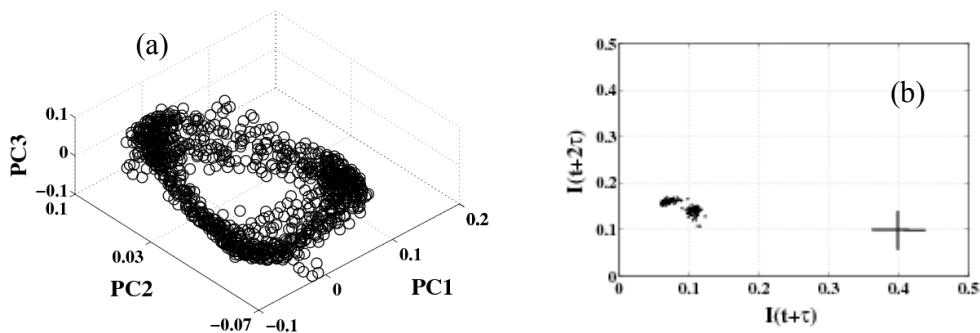


Figure A-IV.4: Non linear signal analysis of photodiode signal for an ellipsoid with aspect ratio $k_1=k_2=4.5$, $Z=0$. (a) Reconstructed 3d phase space using principal component method, $\tau = 120$ ms, PC1,2,3 represents the three main principal components respectively. (b) The corresponding Poincaré section. The cross represents the estimated signal uncertainty. One can conclude that the motion is periodic, within experimental uncertainty.

Fig. A-IV.5 shows the analysis of the photodiode signal displayed in Fig. A-III.11. The time series and the corresponding frequency spectrum suggested periodic motion. This presumption is confirmed by the limit cycle in the 3d phase space (Fig. A-IV.5a) and the Poincare section (Fig. A-IV.5b), similarly to Fig. A-IV.4b.

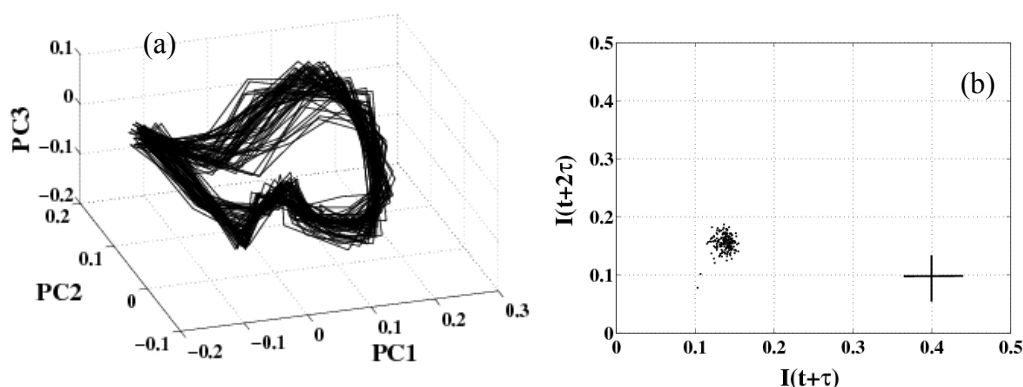
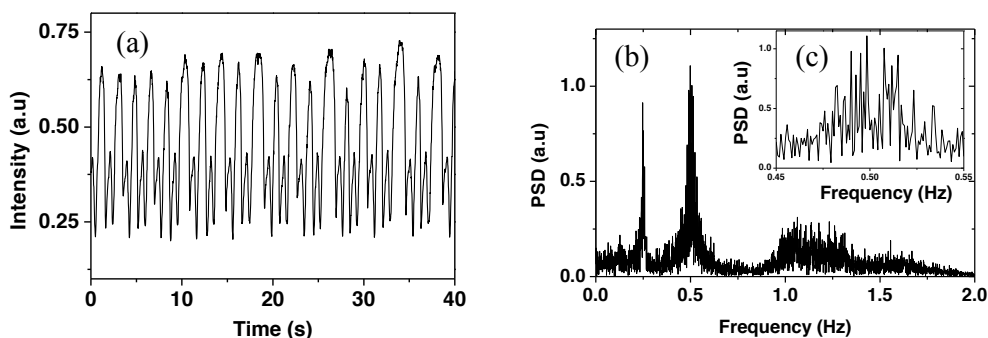


Figure A-IV.5 : *Non linear signal analysis of photodiode signal for an ellipsoid with aspect ratio $k_1=k_2=3.8$, $Z=0$. (a) Reconstructed 3d phase space using principal component method, $\tau =120$ ms. (b) The corresponding Poincaré section provides evidence for a periodic motion, within experimental uncertainty.*

Non periodic motion: We now come to irregular dynamical behaviors. The example displayed below (Fig. A-IV.6) was obtained from a photodiode signal of an ellipsoid with a $k_1=6$, $k_2=5$, still at $z=0$. The Fourier spectrum in Fig. A-IV.6b features multiple peaks with some continuous parts, indicating strongly irregular motion. The reconstructed 3d phase space and two (2d) Poincaré sections are displayed in Fig. A-IV.6d&f. The Poincare section reveals a 2d distribution of points, which is a strong qualitative signature of the presence of chaotic dynamics.



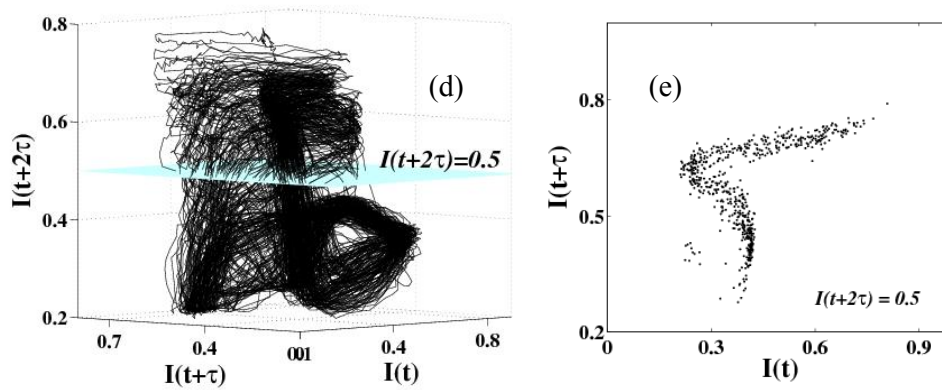
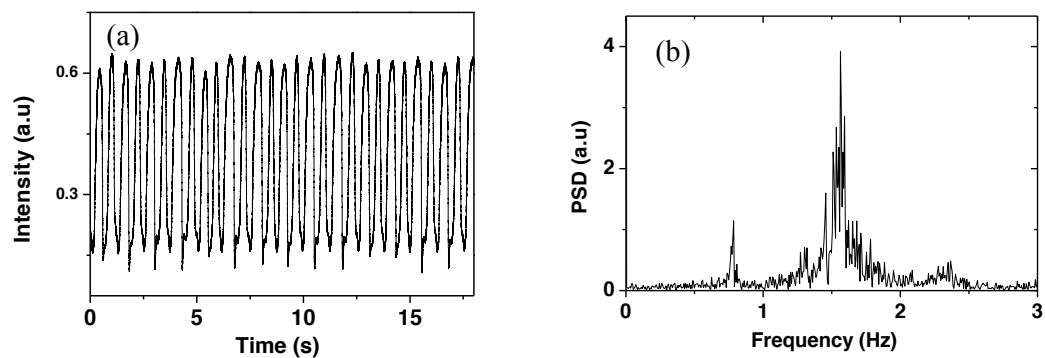


Figure A-IV. 6: Analysis of an irregular signal for an ellipsoid with $k_1 = 6$, $k_2 = 5$. (a) Time series. (b) Fourier power spectrum. (c) Magnified version of the power spectrum to emphasize the presence of multiple peaks in the spectrum. (d) Reconstructed 3d phase space using the time delay method, $\tau = 0.5s$. The faint blue plane marks the location of the Poincaré section displayed in panel (e).

Below we provide more examples of chaotic behaviors obtained for different prolate ellipsoids located at beam waist. All the time series were recorded with the photodiode. Note the layered structure of the section in Fig. A-IV.7d, a clear signature of trajectory folding in chaotic attractors (see Fig. A-IV.3).



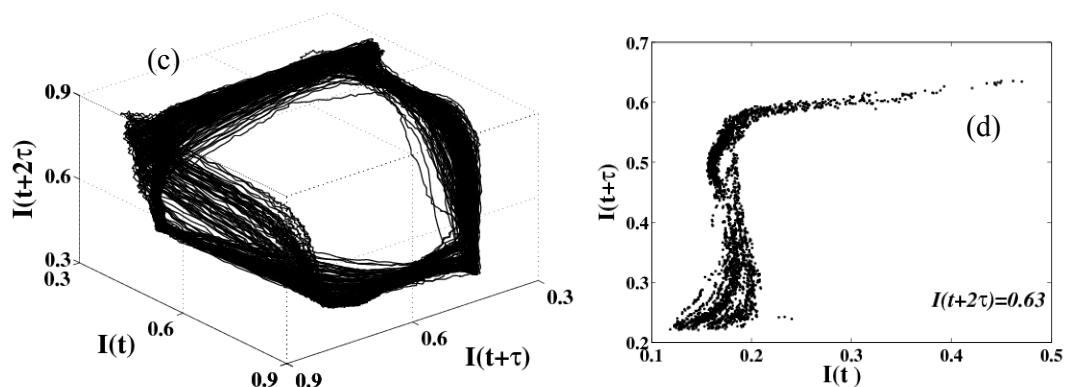


Figure A-IV.7: Ellipsoid aspect ratios: $k_1=4.5$, $k_2=4.1$, $Z=0$. (a) Time series. (b) Corresponding power spectrum. (c) Reconstructed 3d phase space using the time delay method, $\tau=190ms$ (d) Poincaré section computed by placing the cutting plane at $I(t+2\tau)=0.63$.

Another example, with a very elongated ellipsoidal particle, is displayed below (Fig. A-IV.8). The layered structure is very apparent (Fig. A-IV.8e).

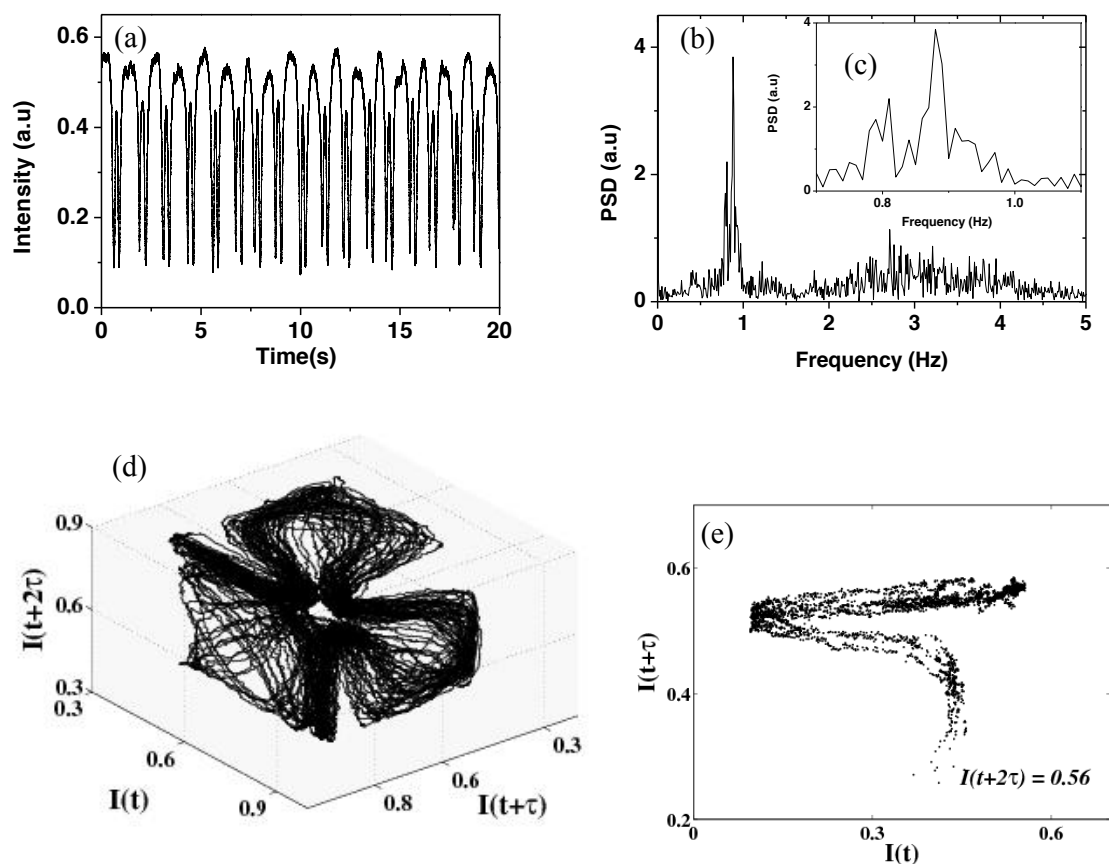


Figure A-IV.8: $k_1=8.9$, $k_2=5.8$. (a) Time series. (b) Corresponding power spectrum. (c) Magnified version of the power spectrum to emphasize the presence of multiple peaks in the spectrum. (d) Reconstructed 3d phase space using the time delay method, $\tau=240\text{ms}$. The 3d phase space is rotated to an angle to show the flower shaped attractor of the dynamics. (e) Poincaré section computed by placing the cutting plane at $I(t+2\tau) = 0.56$.

A-IV.2b: Influence of the beam diameter (parameter Z)

The data analyzed in this paragraph were obtained with the same particle ($k_1=4$ and $k_2=3.6$, see Fig. A-III.24), which was located at varying altitudes near and below the beam-waist. Essentially we want to examine the reconstructed trajectories corresponding to the first and third rows in Fig. A-III.24.

The motion of the ellipsoid reported on Fig. A-III.24 at $Z=0$ features both amplitude and frequency modulated dynamics. The corresponding reconstructed 3d phase space, together with the broad distribution of points in the Poincaré section, reveals complex irregular dynamics.

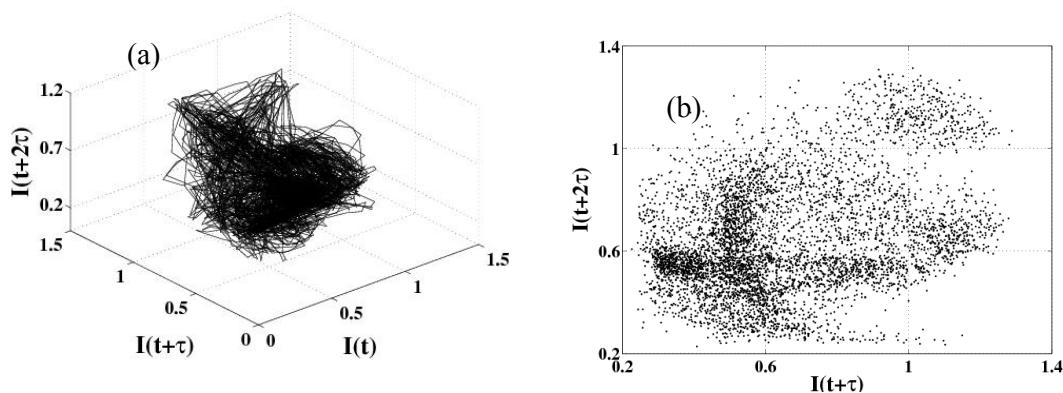


Figure A-IV.9 : (a) Ellipsoid parameters: $k_1=4$, $k_2=3.6$ and $Z=0$, the time series and PSD are reported in Fig. A-III.24. The 3d reconstructed phase space using time delay method ($\tau=0.2\text{s}$) for irregularly oscillating ellipsoid. (b) The corresponding Poincaré section computed with the cutting plane placed at $I(t) = 0.6$.

Note worthily, the dynamics changes to a (close) periodic motion at $Z=-25\ \mu\text{m}$ where the phase space shows a limit cycle consisting of two loops of different sizes. The Poincaré section obtained by putting the cutting plane at $I(t+2\tau)=0.5$ feature two closely packed clouds of points indicating the presence of two characteristic periods in the dynamics.

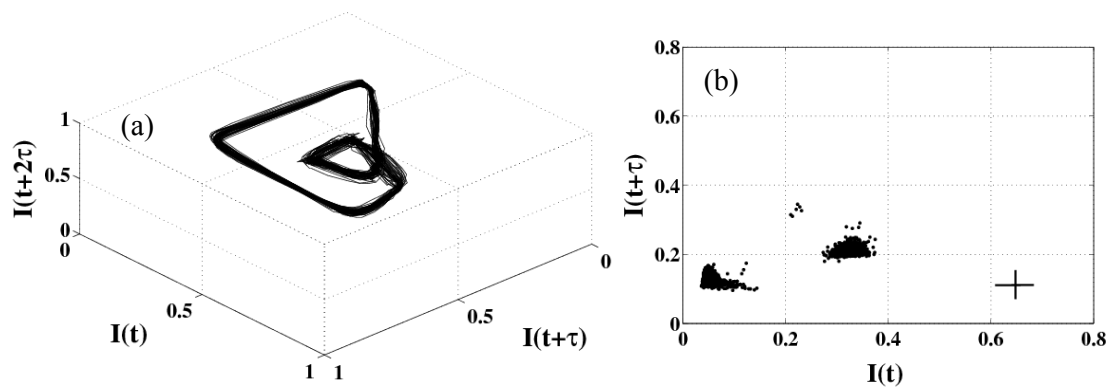
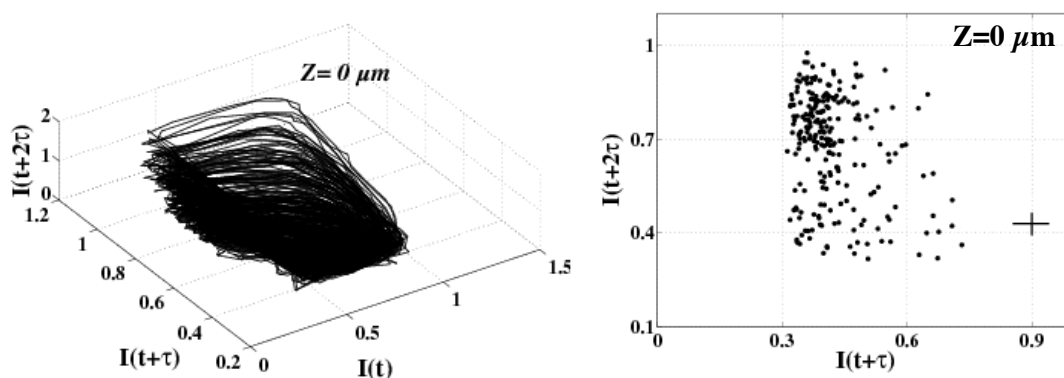


Figure A-IV.10: Ellipsoid parameters: $k_1=4$, $k_2=3.6$ and $Z=-25\mu\text{m}$, the time series and PSD are reported in Fig. A-III.24. (a) The 3d reconstructed phase space using time delay method ($\tau=0.12\text{s}$). (b) The corresponding Poincaré section computed with the cutting plane placed at $I(t+2\tau)=0.5$.

Comparing the phase space and the Poincaré sections of Fig. A-IV.10 & Fig. A-IV.11 reveals that changing Z changes the dynamics from irregular motion to (close) periodic motion. The dependence of the dynamics on Z is very sensitive.

The second example showing the effect of beam diameter is the one shown in Fig. A-III.25. A qualitative evolution of the dynamics can be seen from the change in the shape of the reconstructed phase portrait and the corresponding Poincaré section. A few of them are displayed below for different Z values. As in a previous example, the particle dynamics seems to become more and more regular as Z increases.



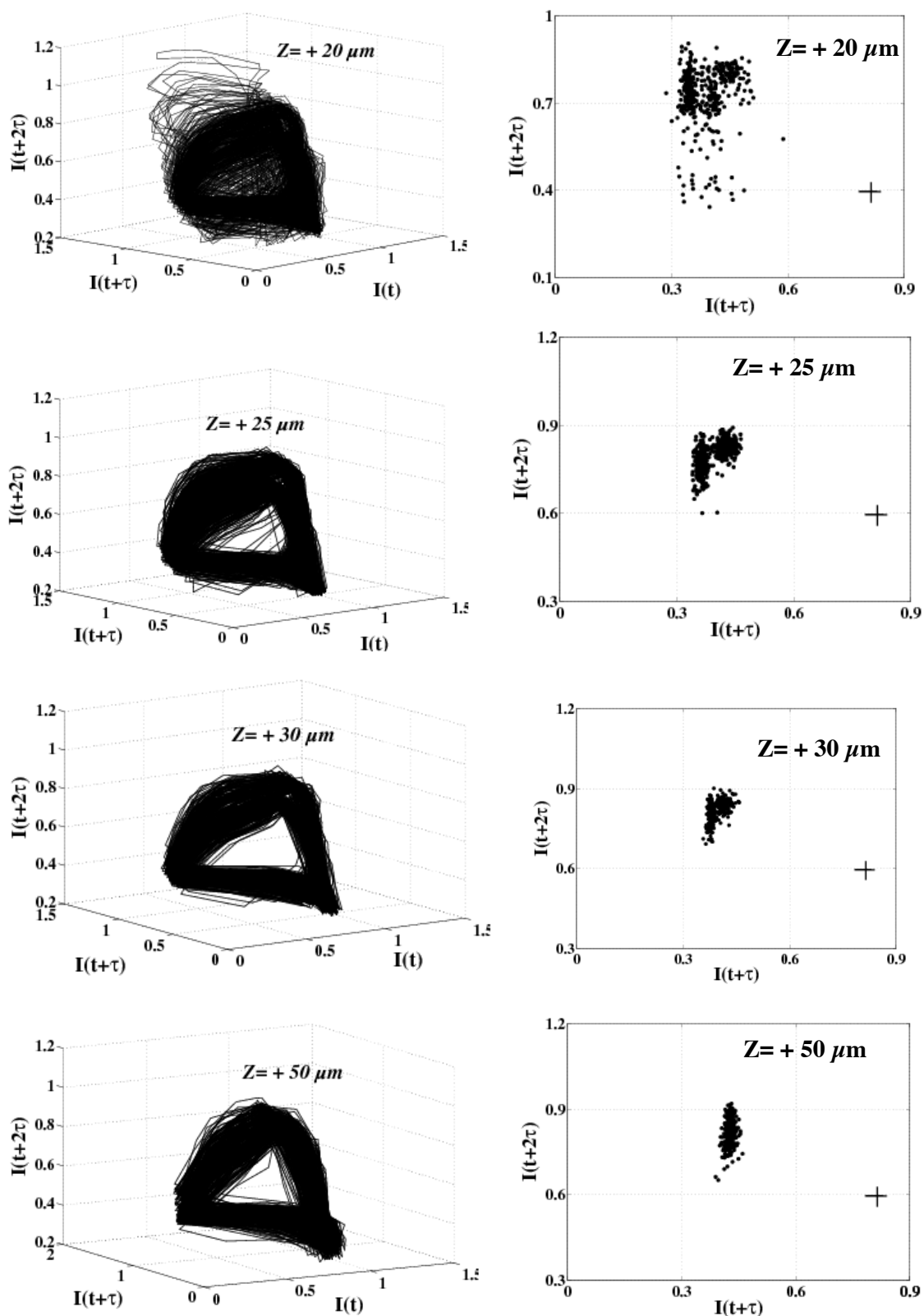


Figure A-IV.11 : The dynamics of an ellipsoidal particle ($k_1 = 4.1$ and $k_2 = 3.8$) subjected to different beam diameters, the time series and PSD are reported in Fig. A-III.25. (left column)

The 3d reconstructed phase space using time delay method. (right column). The corresponding Poincaré sections computed with the cutting plane placed at the average $I(t)$ crossing. The Poincare section evolves from broadly distributed points at $Z=0 \mu\text{m}$ to small packet of points at $Z= +50\mu\text{m}$.

As evidenced from both the phase space and Poincare section, the dynamics oscillating ellipsoids is strongly affected by the beam diameter.

A-IV.3 Conclusion

The phase space reconstruction techniques that we applied to the photodiode signals allowed us to reveal characteristic features of the particles' dynamics. In several examples, we found trajectories that were limit cycles in 3 dimensions, meaning that the motion was periodic. This result did not come as a surprise, as the corresponding power spectra were made of well marked peaks, at frequencies that were integer multiples of a fundamental frequency. Other examples instead revealed clearly non periodic motions. As we could see from the Poincaré sections, the reconstructed trajectories had characteristics of strange attractors, meaning that the particle motion pertained to deterministic chaos. A few other examples gave Poincaré sections with no discernable structures, leaving the impression of extreme complexity akin to turbulence.

A rather unexpected outcome of this study is the fact no simple relation seems to exist between the control parameters, namely k_1 , k_2 and z , and the nature of the dynamics. As we saw, ellipsoids of moderate aspect ratio, i.e. $k \approx 4$, undergo periodic, chaotic and even turbulent-like dynamics at $z = 0$, depending on the chosen particle. Chaos is observed at $z = 0$ equally with moderate ($k \approx 4$), medium ($k \approx 6$) and large ($k \approx 8$) aspect ratios, and no clear tendency emerges when a given particle is brought at different altitudes, i.e. at constant k and variable z . This diversity of behaviors leaves us with some frustration, because we would have liked to find a simple route from periodicity to chaos, for instance through a sequence of period doubling [Thamilmaran 2002]. This possibly simple route might be searched as a line in the space of control parameters (k_1 , k_2 , z). Unfortunately we cannot vary the aspect ratios in the course of an experiment, since we can only pick up a particle of given dimensions. We first hoped that simply varying z for a few given examples of (k_1, k_2) might be enough, but we did not meet a complete periodic to chaotic sequence using this method yet. Nevertheless, such a sequence may exist and it will be worth accumulating more data to find it.

A-V: Ray-optics 2d model

The goal of this chapter is to set up a simulation of the ellipsoidal particles' oscillations, using a very simple optical model based on ray-optics.

To simulate the particle's response, we must first calculate the optical force \mathbf{F} and torque $\mathbf{\Gamma}$ acting on the particle in a laser beam of given characteristics. In a rigorous version, the problem amounts to calculating the electromagnetic field scattered by the particle. In theory, \mathbf{F} and $\mathbf{\Gamma}$ can then be obtained from the Maxwell stress tensor of the whole e.m. field (incident+scattered) by integration on a surface that surrounds the particle [Jackson 1975, Jonáš 2008].

When the particle is a few micrometers in size, the wave nature of the e.m. field must be taken into account. The case of a sphere that scatters light from a focused laser beam has been the matter of many dedicated works since the eighties. Rigorous solutions to this problem have been obtained and are known as "Generalized Lorenz-Mie theory" (GLMT) [Gouesbet 1988, Ren 1994]. The GLMT has been extended to spheroidal shapes (i.e. cylindrically symmetrical ellipsoids) by Xu et al. [Xu 2007]; these authors computed radiation pressure forces and torques for particle aspect ratios (k) up to 1.5.

In general, calculation of the scattered field by particles of more complex shapes is a very difficult task that can only be performed using numerical techniques. Different methods have been proposed to be applicable to about any particle shape, namely the discrete dipole approximation (DDA) [Draine 1994, Yurkin 2007, Chaumet 2002, Bonessi 2007, Simpson 2011a&b], the finite difference time domain (FDTD) [Benito 2008, Qin 2009], the vector finite element [White 2000], multilevel multipole [Song 1995, Sheng 1998] and T-Matrix methods [Varadan 1980]. A numerical tool box using the latter method has been proposed for application to optical tweezers geometries, for different kinds of laser beams [Nieminen 2007].

Calculating the field scattered by our ellipsoidal particles, of large aspect ratio and several 10 μm in size, is currently at the limit of possibilities of existing numerical methods⁵. In the course of our PhD project, we opted for a very simplified analysis based on ray-optics (RO), in two dimensions. The assumptions made in the model are rough, meaning that the simulation has no pretention to be quantitatively accurate. In spite of these limitations, we hope that the model still captures essential trends of the particle's mechanical response to the

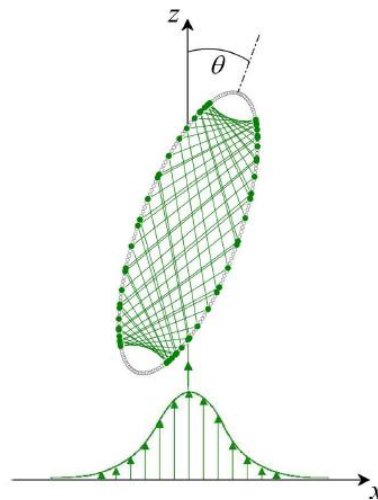
⁵ This work is scheduled as a future work in the frame of AMOCOPS project, headed by Prof. F. Ren (CORIA, Rouen. AMOCOPS acronym stands for "Advanced Methods for Optical Characterization of Complex Particle Systems".

laser beam. Most importantly, we want to know whether RP forces alone are sufficient to produce the kind of oscillations seen in the experiments. We do reach this conclusion, as we will see.

In the next paragraph, A-V.1, we explain the basis of the RO model and the reasoning made to obtain particle trajectories. As the development of the numerical routine was not my job (this work was done by J.C. Loudet), I will not dwell on details of numerical techniques and programming, and will directly focus on the results of the simulation, in the form of force-torque maps and particle trajectories. The reasons why the computed forces and torques lead to particle oscillation are analyzed in the second paragraph, A-V.2. We base the analysis on a simplified representation of the force-torque maps, which we call “4-pole force / 2-pole torque model”.

A-V.1: 2-dimensional ray-optics model

Figure A-V.1: *2d ray optics (RO) model in the (x, z) - plane. The ellipsoid’s long axis makes an angle θ with respect to the z -axis. 60 reflections inside the ellipsoid are shown here for illustration. The laser beam has a Gaussian intensity profile.*



The RP force and torque acting on an ellipsoid can be calculated using the simplified picture of Fig. A-V.1. The laser beam is supposed to be constituted by a collection of parallel rays, propagating along z . The intensities of rays follow a Gaussian distribution along x . Here we only address the problem in 2-dimensions; consequently rays keep inside the same plane during propagation. The procedure to calculate RP forces and torques is the same as in refs [Ashkin 1992, Walz 1992, Xu 2008, Sosa-Martínez 2009, Hinojosa-Alvarado 2010]. Each ray becomes reflected and refracted many times along the ellipsoid’s boundary, at points M_i . Each

scattering event contributes an elementary force \mathbf{f}_i , proportional to $dP_i \cdot (n_1 \hat{\mathbf{i}}_i - n_1 R_i \hat{\mathbf{r}}_i - n_2 T_i \hat{\mathbf{t}}_i)$, where $\hat{\mathbf{i}}_i, \hat{\mathbf{r}}_i, \hat{\mathbf{t}}_i$ are unit vectors denoting, respectively, the incident, reflected and transmitted rays' directions at M_i . n_1, n_2 are the refractive indices in the corresponding media, and R_i, T_i are the Fresnel power reflectance and transmittance. dP_i is the energy of the i th incoming ray at M_i . We follow the propagation of a given ray inside the particle using a standard ray-tracing technique [Glassner 1989], and stop propagation when the ray's power has decreased by about 10^3 . We checked that pushing the computation further ($>10^3$) did not significantly change the final values of force and torque.

Medium 1 is water ($n_1=1.336$) and medium 2 is polystyrene ($n_2=1.583$). As the Fresnel coefficients depend on polarization, we suppose that the beam is linearly polarized, in TE configuration, i.e. perpendicular to the figure. Taking the ellipse centre C as the reference point, \mathbf{f}_i contributes an elementary torque $\boldsymbol{\tau}_i = \mathbf{C}M_i \times \mathbf{f}_i$. We obtain the total RP force and torque by vector summation of all scattering events for each ray, and on all rays that compose the Gaussian beam. The calculation is worked out for different configurations of the ellipsoid, $|x| \leq x_{\max}, |\theta| \leq \theta_{\max}$, with a corresponding (121 x 36) resolution. Note that the calculation is not restricted to small excursions, meaning that the ellipsoid may move almost completely out of the beam, as observed in the experiments. We thus obtain maps of \mathbf{F} and $\boldsymbol{\Gamma}$ for different configurations of the ellipsoid with respect to the laser beam. An example of such maps is shown in Fig. A-V.2.

In addition to RP forces, the particle in water experiences hydrodynamic friction forces and torques, both in translation (\mathbf{F}_{Hx}) and rotation ($\boldsymbol{\Gamma}_{H\theta}$), and a contact force (\mathbf{F}_c) along the chamber ceiling. Inertia forces are negligible, due to the small particle size and velocity. To a first approximation, we may suppose

$$\mathbf{F}_{Hx} = -\gamma_x \dot{x} \hat{\mathbf{x}} \quad , \quad (\text{A-V.1a})$$

$$\boldsymbol{\Gamma}_{H\theta} = \gamma_\theta \dot{\theta} \hat{\mathbf{y}} \quad , \quad (\text{A-V.1b})$$

$$\mathbf{F}_c = F_z \hat{\mathbf{z}} \quad , \quad (\text{A-V.1c})$$

with $F_z = \mathbf{F} \cdot \hat{\mathbf{z}}$, the vertical component of the RP force. In eq. (A-V.1), we supposed that translational and rotational friction were decoupled and that contact along the top surface did

not significantly modify the hydrodynamic friction. Our point is that the oscillations are general, be the particle located in bulk or in contact to the top surface. Therefore the model should be able to reveal oscillations, even if hydrodynamic effects related to the proximity of the solid surface are ignored. A specific lubrication term such as that elaborated in [Cheng 2003] may well play a role in reality but is not essential in the model. With the above assumptions, the contact force is simply vertical (Eq. A-V.1c).

We obtain the equations for particle motion by writing that the total force and torque (RP + hydro. + contact) acting on the particle are null. Here we give the simplified form of the equations, which holds in the limit of small particle tilt angle ($\theta \ll \pi/2$):

$$\mathbf{F} \cdot \hat{\mathbf{x}} = \gamma_x \dot{x} \quad (\text{A-V.2a})$$

$$\mathbf{\Gamma} \cdot \hat{\mathbf{y}} + \tilde{R} \theta \mathbf{F} \cdot \hat{\mathbf{z}} = -\gamma_\theta \dot{\theta} \quad (\text{A-V.2b})$$

In eq. (A-V.2b), \tilde{R} is a length given by $\tilde{R} = Rk^{-4/3}(k^2 - 1)$. The second term in eq. (2b) is the torque exerted by the RP force around the point of contact of the particle to the top surface.

We numerically integrated eqs. (A-V.2) using a standard fourth order Runge-Kutta algorithm. As we needed values for the friction coefficients, we adopted those which have been derived for prolate ellipsoids in 3d for translation and rotation perpendicular to the symmetry axis. A standard formulation reads: $\gamma_x = 6\pi\eta b G_x$ and $\gamma_\theta = 6\eta V G_\theta$. Here V is the ellipsoid volume, η is the viscosity of water ($\cong 1 \text{ m.Pa.s}$ at room temperature), while G_x and G_α are geometrical factors which only depend on k . Both increase with k . We used the explicit formulas for G_x and G_α derived from Perrin's equations and given in [Happel 1983]. Note that V is constant in our problem, since this is the volume of the mother sphere from which all ellipsoids are derived (Fig. 3): $V \cong 524 (\mu\text{m})^3$.

Results of the integration are shown in Fig. A-V.3 for two different values of the particle aspect ratio. For the chosen parameter values, the model features a bifurcation between static on-axis equilibrium and oscillating states. The computed threshold is $k_c \cong 4.085$. Short ellipsoids ($k < k_c$) are predicted to be stably trapped in vertical position (Fig. 11A,B), while longer ones ($k > k_c$) may either keep on-axis or permanently oscillate, as illustrated in Fig. 11C,D. Note that computed oscillations (Fig. 11A,C) are far from sinusoidal. The bifurcation is of "sub-critical" type [Katok 1995], meaning that the amplitude of the limit cycle (Fig. 11D) discontinuously jumps from zero at $k < k_c$ to finite at threshold, and that 2 dynamical

states co-exist above k_c . Though stationary motions only appear above k_c , ellipsoids just below k_c show transient oscillations. In practice, a particle of that kind is expected to be stable on axis, but very susceptible to mechanical perturbations. If for instance the particle is laterally pushed a few μm off-axis, it should return back to the stable configuration through a few damped oscillations.

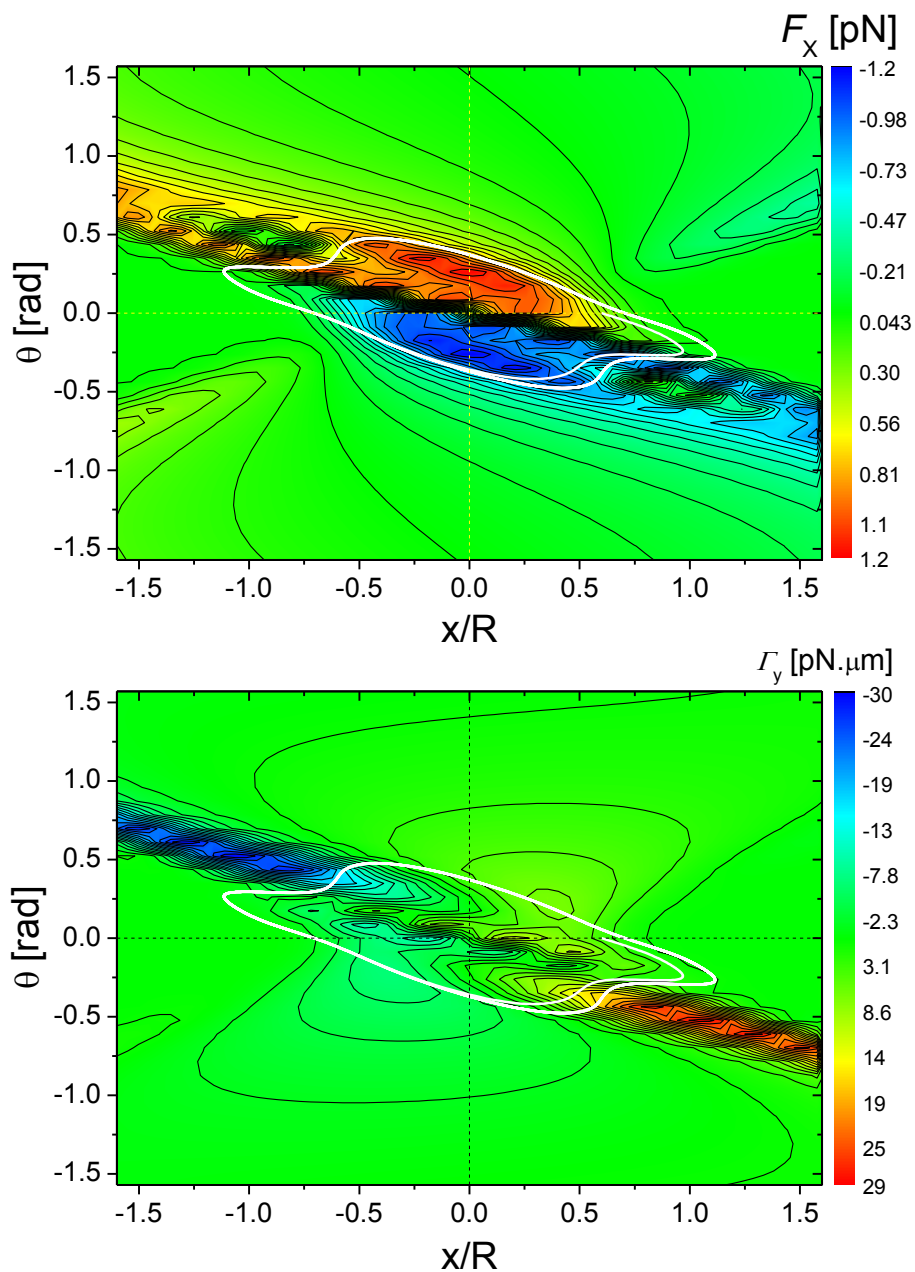


Figure A-V.2: Maps of total force (F_x) and torque (Γ_y), as functions of off-centring (x/R) and tilt (θ) of the ellipsoid (TE polarization mode; R is the sphere radius from which the ellipsoid is derived). The white solid curves superimposed on both graphs locate the computed limit cycle. Shape parameters of the particle are $a = 10.37 \mu\text{m}$, $b = 2.41 \mu\text{m}$, giving $k = 4.3 (>k_C=4.085)$. Those for the laser beam are the same as in the experiment ($\lambda = 514 \text{ nm}$, $\omega_0 = 1.3 \mu\text{m}$). The total power of the laser beam is 1 mW .

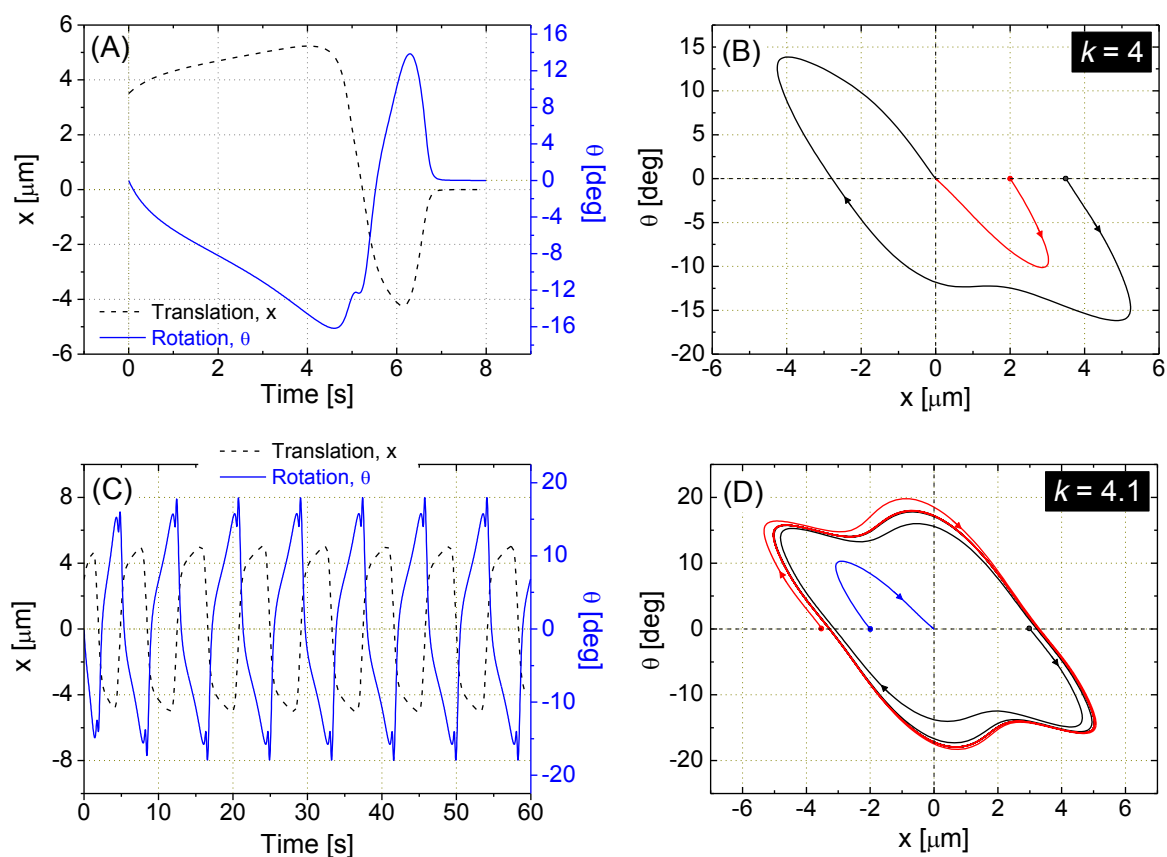


Figure A-V.3 : (a, b, c, d): Computed particle dynamics from Eqs. (2). (a) & (b): damped oscillations obtained with $k=4$ (below k_C). (c) & (d): sustained periodic oscillations for $k=4.1$ (above k_C). (a) & (c) show the temporal evolutions of the ellipsoid's centre in translation and of the axis orientation. (b) & (d) show the corresponding trajectories in phase space with two different initial conditions. In (b), $k=4$ (below k_C) and point $(0,0)$ is the stable configuration. For $k=4.1$ (just above k_C), the system bifurcates to a limit cycle, as shown in (d) (black and red curves), provided the starting coordinates (black and red dots, color online) are far

enough away from point $(0,0)$. Otherwise, the system chooses the other attractor, i.e. point $(0,0)$, as illustrated by the blue curve (color online).

A-V.2: 4-pole force / 2-pole torque model

We worked out calculations of force-torque maps for increasing values of the aspect ratio, from 1.5 up to 4.5. Not surprisingly, the main features of the maps are very different for short ellipsoids ($k \ll k_C$) (Figs. A-V.4 & 5) and long ones ($k > k_C$) (Fig. A-V.2). Below we focus our analysis on the maps corresponding to $k \approx 4$, i.e. close to the threshold for oscillation in TE polarisation. The maps just below and just above threshold (at k_c^- and k_c^+ , respectively) look about almost the same, not surprisingly either. However the dynamics are very different (trapped particle and oscillation, respectively). We want to identify what minor difference in the maps has resulted in very different particle behaviours.

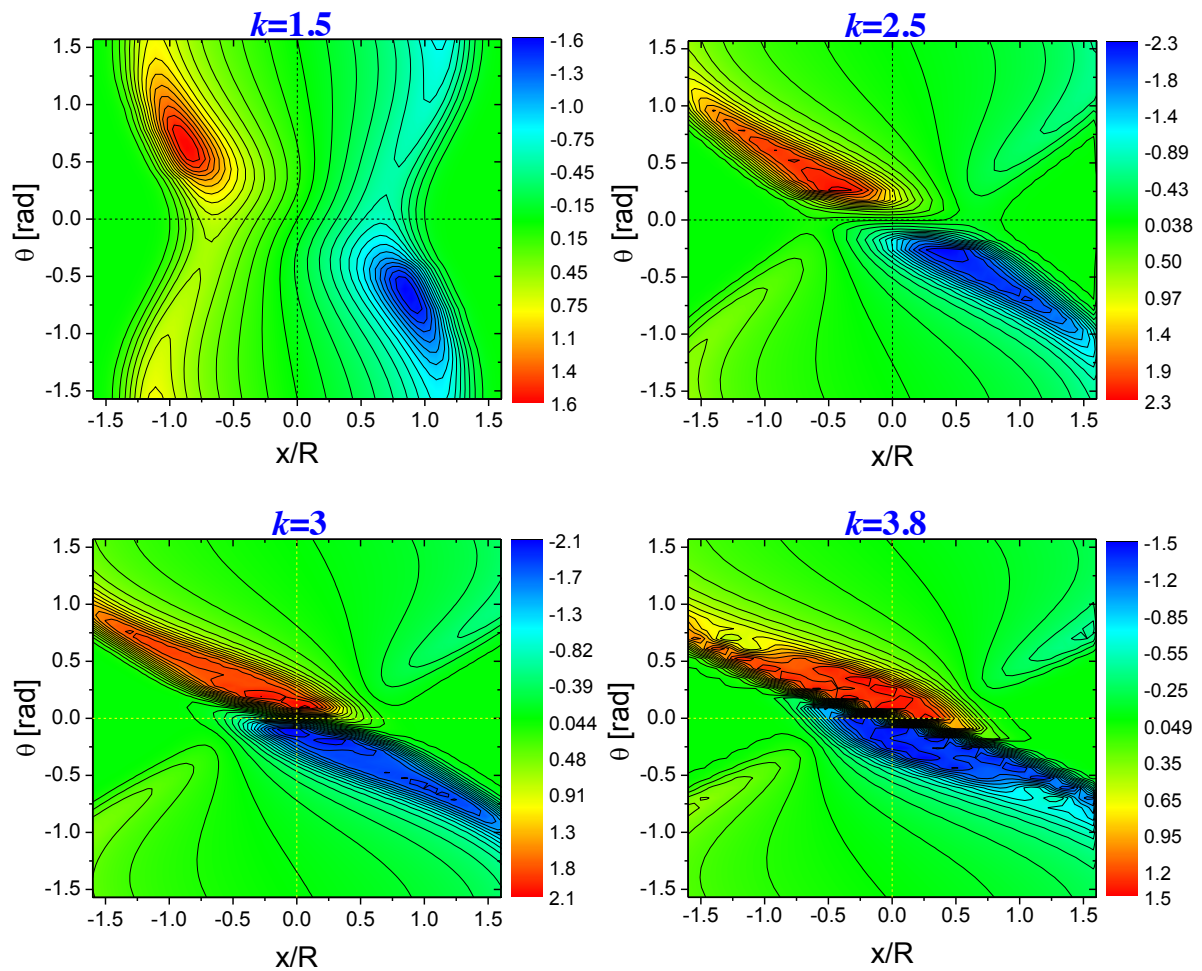


Figure A-V.4 : Force maps (F_x [pN]) computed from the RO model as functions of off-centring (x/R) and tilt (θ) of the ellipsoid for several aspect ratios $k < k_C = 4.085$ (TE polarization; R is the sphere radius from which the ellipsoid is derived).

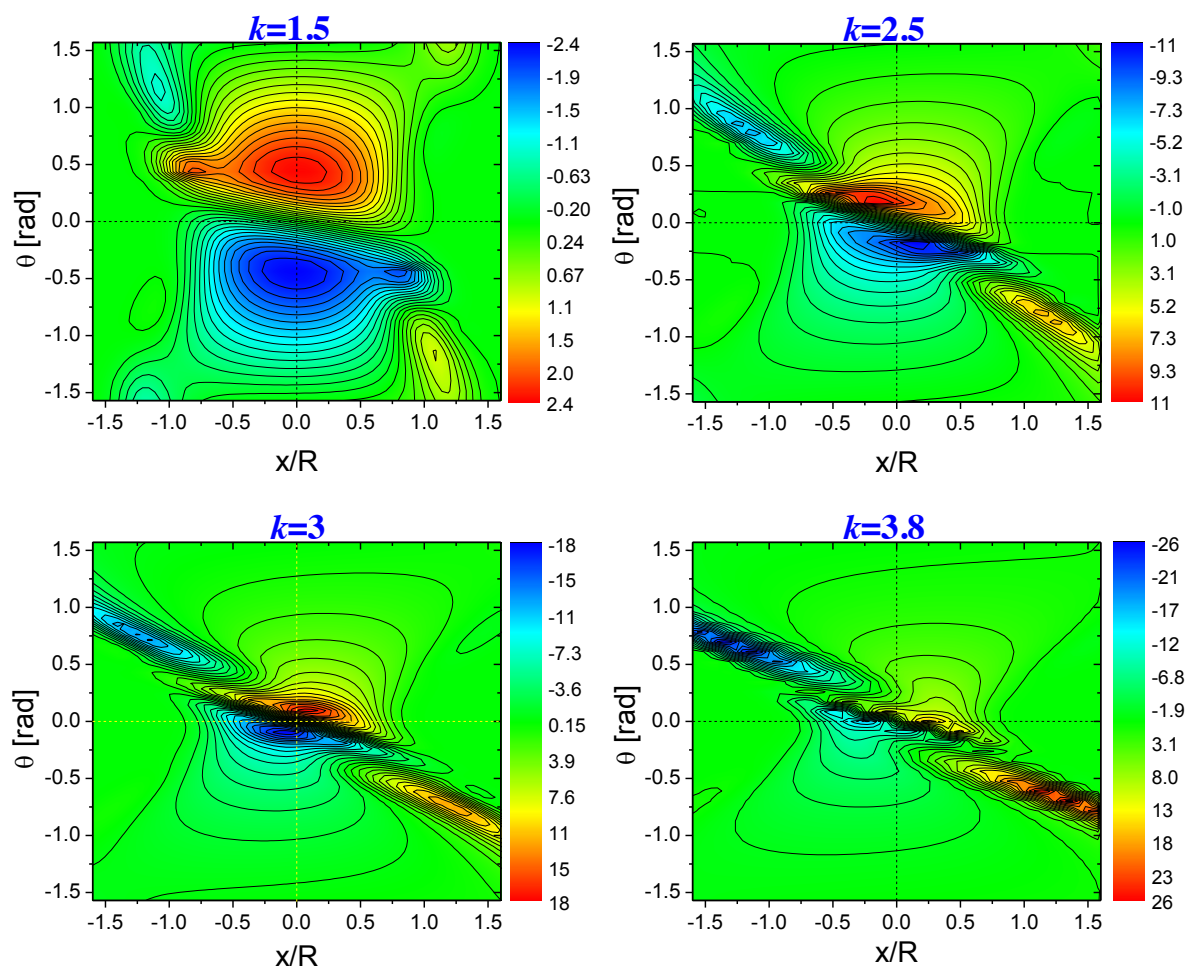


Figure A-V.5 : Torque maps (Γ_y [$pN \cdot \mu m$]) corresponding to the force maps shown in Fig. A-V.4 for the same aspect ratios k (the other parameters are equally defined).

As aforesaid, drastic changes occur in the structure of the computed force and torque maps when increasing the aspect ratio (Figs. A-V.2, 4 & 5). When k approaches k_C ($=4.085$ for the TE polarization mode), we may clearly identify red ($F_x, \Gamma_y > 0$) and blue ($F_x, \Gamma_y < 0$) areas that are well-aligned along some preferred direction in the (x, θ) plane.

For $k \approx k_C$, the main features of force-torque numerical maps therefore may be sketched as in the cartoon presented in Fig. A-V.6a where we have superposed the force and torque elements, with the conventions defined in the panel at right. The sketch is obviously a very simplified view, but we hope that it contains the key features to explain the bifurcation. The sketch only contains large scale features; we will come later to some details of the maps such as the fine structure close to the $(0, 0)$ fixed point. In the representation of Fig. A-V.6, the force map is made of a main “dipole”, namely the pair of large spots on the θ axis, and a secondary dipole, namely the pair of very elongated spots, at about right angle from the main dipole. The axes of both dipoles go through the origin $(0, 0)$.

The torque map is sketched as a couple of elongated spots too, but, these do not coincide with the secondary force spots. The one at left is shifted upwards, and that at right is symmetrically shifted downwards.

We note that the 6-pole structure is slightly tilted from the frame axes, but we suppose that the tilt is not essential. We similarly suppose that contracting the x -axis may transform the elongated spots into circular ones. We thus obtain the simplified structure displayed in Fig. A-V.6b, where θ has been re-labelled as y .

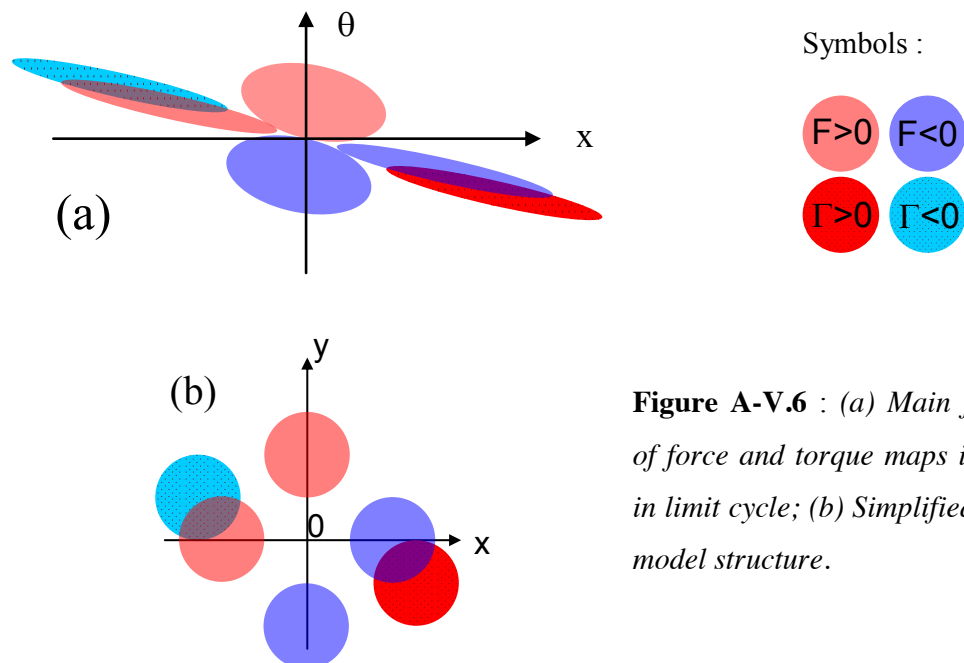


Figure A-V.6 : (a) Main features of force and torque maps involved in limit cycle; (b) Simplified 6-pole model structure.

Equations corresponding to the above sketch may be written as:

$$\begin{aligned}\dot{x} = X(x, y) &= G(x)G(y-1) - G(x)G(y+1) - G(x-1)G(y) + G(x+1)G(y) \\ -\dot{y} = Y(x, y) &= A \cdot [G(y+u)G(x-t) - G(y-u)G(x+t)]\end{aligned}\quad (\text{A-V.3})$$

$G(x)$ may be defined as a simple Gauss function.

$(0, \pm 1)$ and $(\pm 1, 0)$ are the coordinates of the force poles.

$(t, -u)$ and $(-t, u)$ are the coordinates of the torque poles, with $t \geq 1$ and $0 < u < 1$.

The A parameter represents the amplitude of the torque, which increases with k .

The Jacobian matrix of (A-V.3) near $(0, 0)$ is:

$$J = 4 \begin{bmatrix} -e^{-1} & e^{-1} \\ -At \cdot e^{-(t^2+u^2)} & Au \cdot e^{-(t^2+u^2)} \end{bmatrix}\quad (\text{A-V.4})$$

We find that the system bifurcates from spiral stability to spiral instability at $A = A_c = u^{-1}e^{-1+t^2+u^2}$.

Below (Fig. A-V.7) we show results from numerical resolution of the above dynamical system, obtained by Runge-Kutta (order 4) integration. We show a few examples with $(t=1, u=0.5)$. With these values, the torque poles have same abscissas as those of the horizontal force dipole. We checked that this case had nothing special by testing with other values ($t > 1, u \neq 0.5$). Computation time considerably increases with t , but we find the same trends (bifurcation and limit cycles) in all cases.

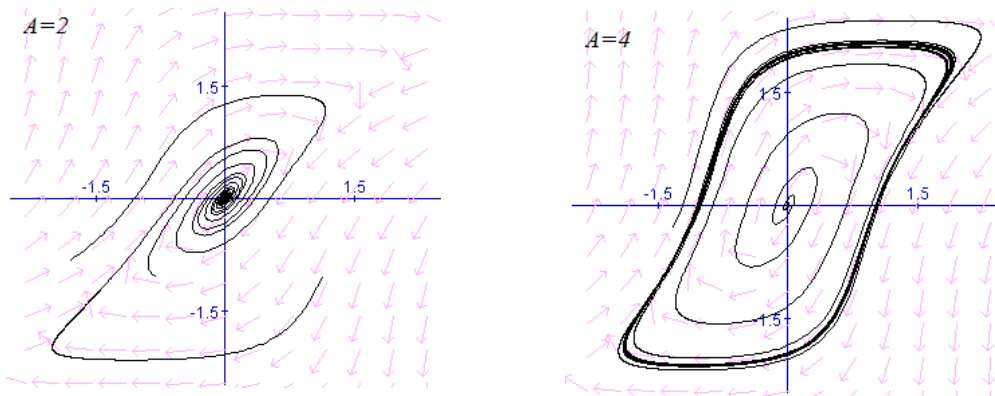


Figure A-V.7: Trajectories obtained by integration of Eqs (A-V.3), below (a) and above the transition (b). Here $(t=1, u=0.5)$.

For $A=2$, the central point $(0,0)$ is spirally stable. Destabilization occurs at $A_c \approx 2.57$. For $A > A_c$, $(0, 0)$ is spirally unstable. The divergence saturates on a limit cycle, whose amplitude

increases with A . For $A=4$, the cycle encompasses the $(0, \pm 1)$ force poles, and gets through the $(\pm 1, 0)$ force poles.

We also made a few tests by replacing the Gauss function by a Lorentzian function. The substitution changes A_C values and amplitudes of the limit cycles, but the trends are similar. It then seems that G only has to be bell-shaped for the model to capture the essential features of the system dynamics.

Summarizing, the 4-pole force / 2-pole torque model, represented by Eq. (A-V.3), produces the kind of bifurcation that has emerged from the simulation. The key parameter that drives the bifurcation is the amplitude of the torque, represented by the A parameter in Eq. (A-V.3). When the aspect ratio is slightly increased, from k_c^- to k_c^+ , the torque increases from A_c^- to A_c^+ . The $(0, 0)$ fixed point becomes unstable and the system switches to an oscillating state.

Note that the bifurcation, in the above model, is continuous (of super-critical Hopf type), meaning that the extent of the limit cycle grows continuously starting from zero at $A = A_C$. The simulation instead indicates a discontinuous transition, with possibly coexisting static and oscillating states above A_C (see Fig. A-V.3D). The difference may be explained if we now take into account details of the force-torque maps near $(0, 0)$, which are not present in Fig. A-V.6. Force-torque maps near $(0, 0)$ have a complex structure, and it is not clear whether structural fine details are physically relevant or partly due to numerical uncertainty. Nevertheless, the force and torque field distributions are unambiguously different, suggesting a 2-dipole structure as below:

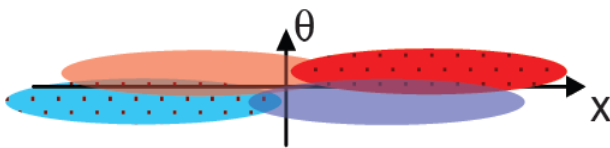


Figure A-V.8 : *Minimum representation of the force and torque maps close to $(0, 0)$ fixed point. Same graphic conventions as in Fig. A-V.6.*

In the same spirit as before, we model the distribution as:

$$\begin{aligned} \dot{x} = X(x, y) &= G(x+s)G(y-1) - G(x-s)G(y+1) \\ -\dot{y} = Y(x, y) &= A \cdot [G(x-1)G(y-1) - G(x+1)G(y+1)] \end{aligned} \quad (\text{A-V.5})$$

$(1, 1)$ and $(-1, -1)$ are the coordinates of the torque poles.

$(-s, 1)$ and $(s, -1)$ are those of the force poles, with $0 < s < 1$.

The Jacobian matrix of the above system near $(0, 0)$ is:

$$J = 4e^{-2} \begin{bmatrix} -s \cdot e^{1-s^2} & e^{1-s^2} \\ -A & -A \end{bmatrix} \quad (\text{A-V.6})$$

We find that $(0, 0)$ is a stable fixed point, whatever the values of A (>0) and s . Due to the fine structure of the force-torque maps near the origin, we expect the $(0, 0)$ configuration (ellipsoid on axis) to be stable. Gathering this result with that from the large scale structure, we expect that $(0, 0)$ and the limit cycle should coexist as attractors. This is in line with the results from the full RO model.

A-V.3: Conclusion and prospects

We worked out a calculation of RP forces and torque acting on an elliptical body in 2 dimensions. We proposed a model where the RP force and torque are balanced by corresponding Stokes drag force and torque and we were able to produce a simulation of ellipsoidal particles dynamics in the optical levitation experiment. Compared to reality, the model was greatly simplified, as it was limited to 2d and within the ray-optics approximation. Nevertheless this scheme predicts behaviours strikingly similar to those observed in experiments. The model indeed predicts a bifurcation between static and oscillating states. The difference between calculated and measured thresholds ($k_C^{calc} > k_C^{exp}$) is presumably not essential, in view of the approximations made. Examination of the calculated force-torque maps allowed us to identify the amplitude of the optical torque as the key parameter that drives the bifurcation.

One of the limitations of the model, at the current stage, is our assumption of a collimated beam (parallel rays). This assumption amounts to supposing that the laser beam structure is invariant along z . This is not exactly so in the experiment because the beam-waist ($\approx 2.6 \mu\text{m}$) is small enough for diffraction to be well visible on the scale of particles lengths (the diffraction length is about $15 \mu\text{m}$). Diffraction effects are not included in the RO model (by definition), but we may simulate a focused beam, over an aperture about equal to that of the real laser beam in the far-field. This extension of the model is currently in progress.

Beyond the work reported here, it would of course be most interesting to elaborate a 3d version of the RO model. At the current stage, we are not able to estimate the influence of the wave nature of light; we just keep to the vague argument that our particles are large enough for ray optics to make sense. The argument mainly holds for the large dimension of the

ellipsoid particles (20 μm , typically), but is questionable if one considers the short axes lengths. Interestingly, we may envisage introducing interference effects within the RO description, following the recent theory of [\[Ren 2011\]](#) (“Vectorial complex ray model”). We currently work along these lines.

**Part B: Wetting dynamics of micron sized particles
on water air interface**

B-I: Introduction

In this part B, we come back to the initial problem which motivated this PhD work, namely the transition from total to partial wetting of ellipsoidal particles. Our primary goal is to investigate the effect of well-controlled non-planar contact lines on the binding dynamics of ellipsoids as they emerge through a fluid interface.

The historical context and motivations for this study were already mentioned in the general introduction of the manuscript. We may just recall here that the wetting dynamics of non spherical particles at fluid interfaces is a general issue which is still quite open nowadays both experimentally and theoretically. Yet, it is of direct relevance to master the making of potentially useful particle stabilised materials such as emulsions, foams or capsules [Binks 2002, 2006, Dinsmore 2002, Aveyard, 2003, Velikov 2007, Destribats 2010].

To set the stage, we shall first consider the basic situation sketched in Fig. B-I.1 prior to specifying the issues we wish to address at the end of this section.

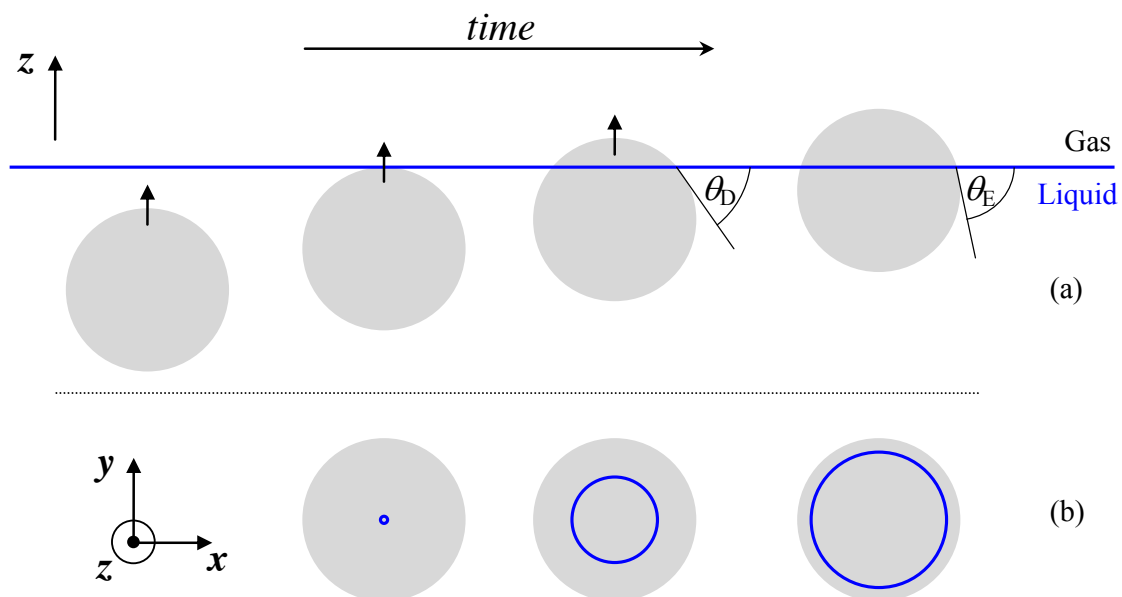


Figure B-I.1: Schematic illustration of the binding dynamics of a sphere at a liquid-gas interface. (a) Variation of the vertical position of the particle over time. θ_D (resp. θ_E) is the dynamic (resp. equilibrium) contact angle. (b) Corresponding sketches of the contact lines viewed from above.

Figure B-I.1 is a schematic illustration of the adsorption trajectory of a sphere to a liquid-gas interface. The sphere is initially completely wetted in water and rises towards the interface thanks to, for example, a weak radiation pressure force exerted by a laser beam. With an ideal sphere, i.e. whose surface is smooth and clean, we may surmise that the emersion process proceeds through a continuous sequence of circular contact lines growing from infinitesimal to the radius corresponding to the equilibrium contact angle (Fig. B-I.1b). In this case, simple thermodynamic arguments suggest that the sphere likes to go to the interface because of the large reduction in surface energy on binding. Indeed, the equilibrium position of the sphere is determined by the minimum of the total surface free energy F which can be written as (see appendix A for details)

$$F = \gamma\pi a^2 (\cos\theta - \cos\theta_E)^2 = \gamma\pi h^2, \quad (\text{B-I.1})$$

where θ_E is the equilibrium contact angle, θ an arbitrary polar angle specifying the position of the contact line at the particle surface and h the height measured with respect to the reference configuration and given by $h = a(\cos\theta - \cos\theta_E)$ (see Fig. A1 in appendix A). Plotting F as a function of h/a (see Fig. B-I.2) reveals the presence of a minimum at $\theta = \theta_E$. It is therefore thermodynamically favourable for the sphere to adsorb at the interface instead of remaining fully immersed in either bulk phase. The free energy barrier ΔF for detachment of the particle from the interface can be millions of times the thermal energy $k_B T$ for micrometer-sized colloids.

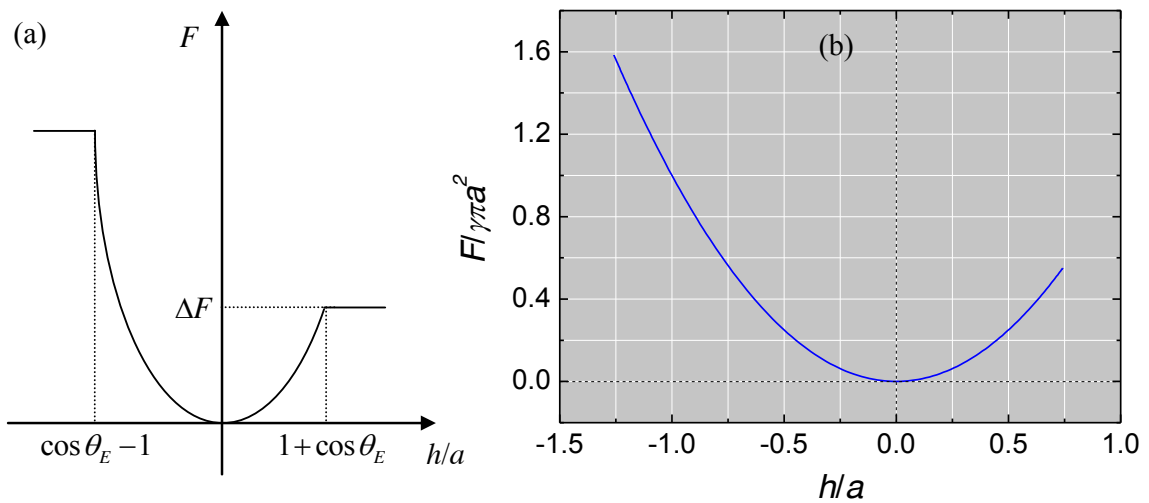


Figure B-I.2: (a) Schematic representation of F as a function of the height h of the particle above the interface (see appendix A for details). (b) Example of a graph obtained with $\theta_E = 75^\circ$.

However, as mentioned in the general introduction, reality shows significant deviations from this simple thermodynamic picture. Early [Bobadova 1995; Danjean 1996] and very recent [Kaz 2012] experiments with latex spheres showed that the particles actually do not easily adsorb and when they occasionally breach the interface, a surprising very slow relaxation dynamics towards equilibrium occurs. This behaviour is displayed on the semi-log plot of Fig. B-I.3 with data extracted from [Danjean 1996]. It exhibits a logarithmic variation of the dynamic contact angle θ_D as time elapses.

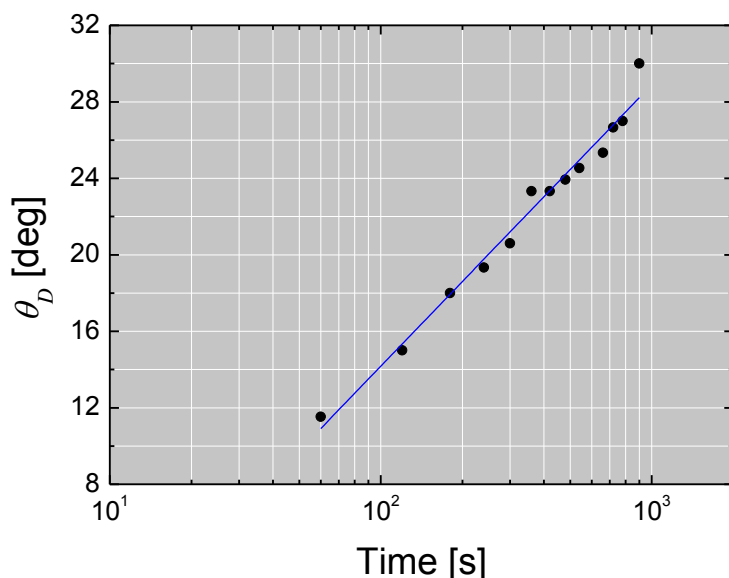


Figure B-I.3: Evolution of the dynamic contact angle θ_D as a function of time for polystyrene spheres trapped at the water-air interface. The data exhibit a logarithmic behaviour. Adapted from [Danjean 1996].

Why is the wetting dynamics so slow ?

What are the forces at work driving the system towards equilibrium and what are the mechanisms for the motion of the contact line ?

These questions were recently addressed in the recent study of Kaz *et al.* [Kaz 2012]. Let us briefly summarize the main physical ideas.

The motion of the contact line is driven by surface tension forces. When these forces are imbalanced (the mechanical equilibrium is not realized), a net force, F_γ , pulls the contact line

down the particle. Assuming a flat interface⁶, such a force (per unit length) may be written as [de Gennes 2005, Kaz 2012, Supp. Inf.]

$$F_\gamma(t) = \gamma [\cos \theta_D(t) - \cos \theta_E].$$

As long as θ_D differs from θ_E , F_γ is not null and the contact line moves. The rate of equilibration will depend on how fast it straddles the particle surface. Now, because the Reynolds number is small (of order 10^{-3} [Kaz 2012]), the motion of the contact line is viscously damped at any time (Stokes regime)⁷. Balancing the damping with the instantaneous work done by F_γ leads to the time evolution of θ_D . A well-known damping mechanism comes from the diverging viscous dissipation due to the shear flow in the highly confined region near the moving contact line especially for small contact angle values (see Fig. B-I.4a and appendix A, §A-2, for more details) [Guyon, Hulin, Petit, 2001, de Gennes 2005]. This diverging dissipated energy slows down the contact line motion and could be responsible for the observed slow relaxation of interfacial particles. However, Kaz *et al.* found out that this hydrodynamic dissipation fails to explain their data. The slow logarithmic wetting dynamics (together with other aspects) turned out to be rather well-explained by another damping mechanism consisting of a thermally-activated hopping of the contact line over tiny surface defects. Although the contact line has an average circular (planar) shape at the micron scale, it is nevertheless likely to be randomly rugged at the nanoscale because it is pinned on surface defects due to either roughness or chemical heterogeneities (see Fig. B-I.4b) [Chen 2005]. In this scenario, the thermal energy $k_B T$ is the engine that drives the depinning of the contact line and controls its motion.

These important findings suggest that interfacial colloids may well be out of equilibrium on experimental timescales (equilibration may take months) and would further rationalize the fact that a rather broad distribution of contact angles values may be found for adsorbed identical colloids.

⁶As mentioned in [Kaz 2012], buoyancy and radiation pressure forces are much smaller than interfacial forces. Since the particle-interface system is isolated and cannot impose a force on itself, the interface must be flat.

⁷In principle, a bulk viscous dissipation due to the motion of the particle in water must also be considered. However, this contribution is small compared to the dissipation generated by the motion of the contact line [de Gennes 2005].

Note that it has been known for a long time that the surfaces of macroscopic solid substrates are far from ideal. Droplet spreading or film dewetting experiments revealed that both chemical and physical defects anchor the contact line and hinders its motion leading to hysteresis phenomena [de Gennes 2005, Seveno 2009]. At the colloidal scale, Kaz *et al.* suggested that surface defects also control the binding dynamics of colloids to fluid interfaces.

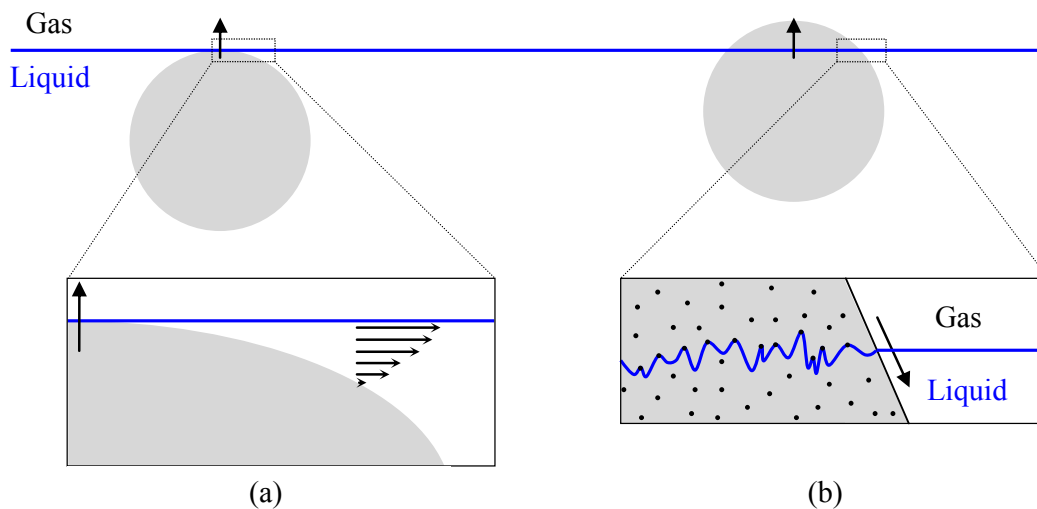


Figure B-I.4: Schematic illustration of the two main damping mechanisms for the motion of the contact line. (a) Hydrodynamic damping. The flow from the wedge created between the particle and the interface dominates the dissipation. (b) Thermally-activated hopping of the contact line over surface defects (black dots). The downwards black arrow indicates the motion of the contact line. Adapted from [Kaz 2012].

Next, concerning anisotropic colloids, and to the best of our knowledge, we are not aware of any experimental report dealing with such dynamic processes. The only work we know about is the one by de Graaf *et al.* [de Graaf 2010] who numerically investigated adsorption trajectories of anisotropic bodies through a fluid interface. The authors calculated how the surface energy would vary as a function of the particle configuration, with the assumption that the interface remains flat (planar) throughout the emersion. However, these authors did not consider the contact line motion and the associated dissipation which, as we just saw, is of paramount importance for the binding dynamics. Consequently, this work turns out to be of limited interest and, as we will see in the discussion part, predicts “strange” adsorption trajectories for prolate ellipsoids.

Hereafter, we shall report on experiments pertaining to the wetting dynamics of ellipsoids. Let end this section by specifying the issues we would like to address.

As already stated in the general introduction, the main point of interest is to probe the influence of well-defined non planar contact lines on the wetting dynamics. Will it matter if the contact line features a large scale curvature as is the case with prolate ellipsoids ? (see inserted image in Fig. B-I.5). More basically, what is the adsorption trajectory of an initially fully immersed static (i.e. non oscillating) ellipsoid in water ? And how is the adsorption mechanism altered with an oscillating particle ? (see Fig. B-I.5).

We first consider the case of spheres with the aim of reproducing the trends highlighted in [Kaz 2012] in order to validate our experimental methods and tools. In a second part, we focus on both prolate and oblate ellipsoids.

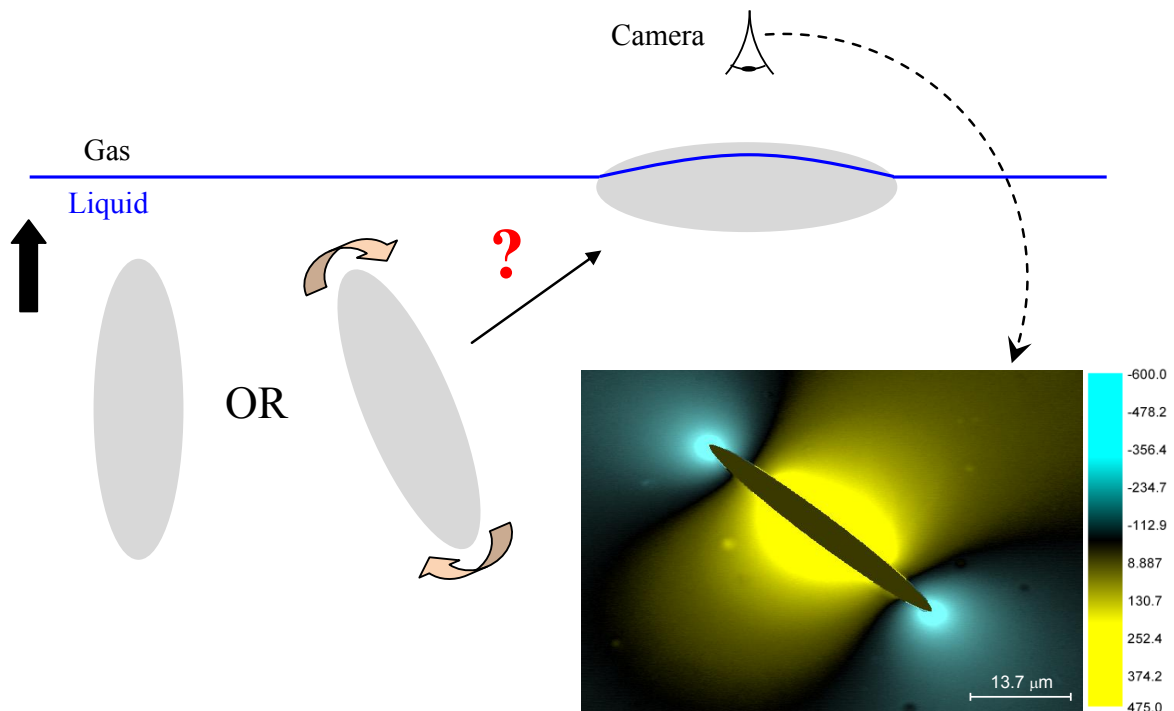


Figure B-I.5: Sketch: Question about the adsorption trajectory of a static (resp. oscillating) ellipsoid to a liquid-gas interface. When trapped at a fluid interface, a prolate ellipsoid features a non-planar saddle-like contact line of quadrupolar symmetry (hence the deformed blue contact line on the sketch). These distortions are clearly evidenced on the appended color-coded image which represents an experimentally determined interfacial profile $z=h(x,y)$ thanks to interferometric measurements (adapted from [Loudet 2006]) Color bar: $h(x,y)$ [nm]. Scale bar: $13.7 \mu\text{m}$.

B-II: Experimental methods

In this paragraph, we first elaborate on sample preparation before mentioning some special features used to probe the wetting dynamics of spheres and ellipsoids.

B-II.1 Sample preparation

As in part A, the samples either consist of polystyrene (PS) spheres (diameter 10 μm) or ellipsoids that are initially dispersed in water. The preparation of ellipsoids follows the same procedure as the one already described in part A. However, it is worth mentioning here that the spheres underwent the same chemical and thermal treatment as the ellipsoids except that they were not stretched. Indeed, as already specified in part A, the preparation of ellipsoids involves a dispersion step in a polyvinyl alcohol (PVA) solution. We know that part of the PVA (although we have not quantified it) remains adsorbed at the ellipsoids surfaces, despite the numerous washing cycles. PVA adsorption makes the particles more hydrophilic and therefore changes the surface chemistry compared to the pristine, untreated spheres from the manufacturer which have not “seen” the PVA. The “PVA treatment” for spheres was therefore necessary to insure that, on an average, all types of particles have the same surface chemistry. This is rather important since wetting phenomena are generally very sensitive to surface properties.

Unlike the levitation experiments described in part A, we used a specifically designed cell to ensure a relative flatness of the water-air interface. The cell consists of two circular rings (inner diameter: 1.5 cm; height: 2.5 mm) made of *glass* glued one on top of each other. The ensemble is further glued on a glass cover slip to allow for transmission observation (see Fig. B-II.1a). The cell is carefully filled with an aqueous particle dispersion (weight fraction $< 0.01\%$) so that the water level just reaches the boundary separating the two rings. This results in a pinning of the water-air interface and minimizes problems related to curved interfaces because of the presence of menisci at the outer edges. Once filled, the cell is painstakingly placed on the sample holder (Fig. B-II.1b) and wetting experiments can start.

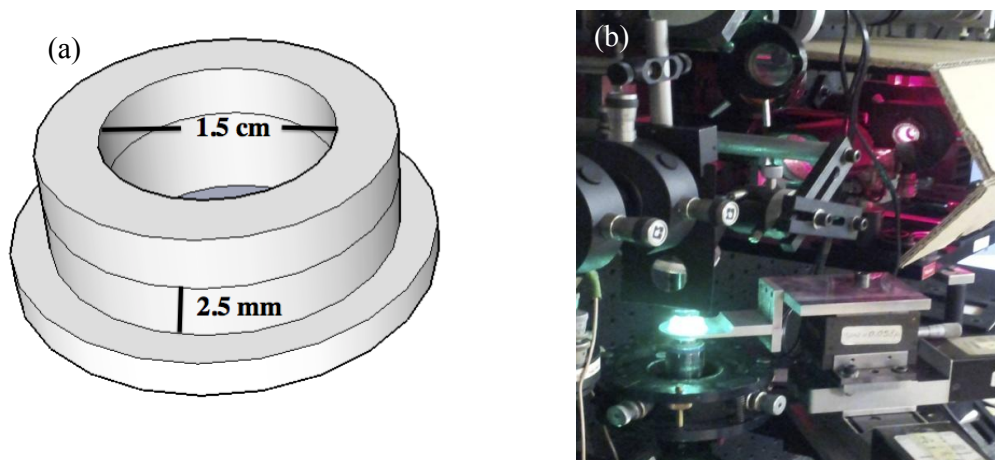


Figure B-II.1: (a) Sketch of sample cell holder used for the wetting dynamics experiments at the water-air interface (b) Zoomed-in view of the cell placed on the sample holder. As in part A, the levitating beam is moderately focused by the objective located just underneath the cell.

B-II.2 Setup

Similarly to [Kaz 2012], we use a weak radiation pressure force (power ~ 10 mW \Leftrightarrow force \sim a few pN) to levitate the particles (both spheres and ellipsoids) all the way up to the water-air interface. We mainly used video means to detect the (approximate) moment when a particle breaches the interface and take images of growing contact lines. In some of the experiments we used the photodiode signal to better resolve the initial step when breaching starts.

The microscope was operated either in transmission or reflection modes. The illumination, in reflection mode, is provided by a red diode. A system was fitted on the setup to instantly switch between both modes. Images in transmission are ideal to visualize the particle body below the W/A interface. In reflection mode, the water surface and the dry part of the particle are well discernible, due to differences in reflectivity and collection efficiency through the aperture of the microscope objective. In general the dry part appears dark, except on the very top part of the particle, while the W/A interface appears in medium grey. The contact line can be located as the boundary between both zones.

A partial sketch of the experimental setup is illustrated in Fig. B-II.2.

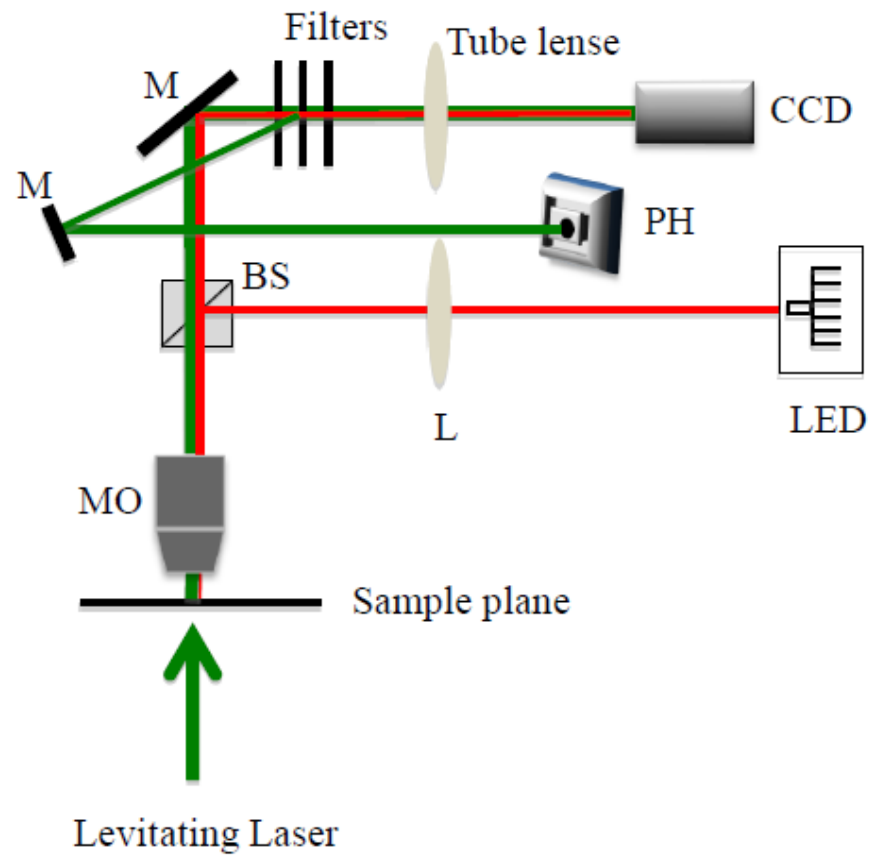


Figure B-II.2: Partial sketch of experimental set-up for the wetting dynamics experiments. *MO: microscopic objective, BS: Beam splitter, LED: light emitting diode, L: lens, PH: photodiode, M: Mirror and CCD: camera.*

B-III: Wetting dynamics of spheres

In this section, we report experimental observations of the wetting dynamics of micrometer-sized spheres at the W/A interface. As mentioned above, our goal here is to recover the main results of [Kaz 2012] to validate our approach.

Results and discussion

The experiments were conducted in pure deionized water and started by levitating a sphere all the way up to the interface. In most cases, we noticed that the spheres remained trapped just below the interface without actually crossing it. Indeed, turning off the laser made the particle sediment. As pointed out by Mbamala & von Grunberg [Mbamala, 2002], the apparent repulsion from the interface may be due to electrostatic interactions: when dispersed in aqueous solutions, the surfaces of polymeric particles are indeed always charged due to the dissociation of some chemical groups. These charges are likely to interact with similar charges in the vicinity of the interface or with image charges. As in [Kaz, 2012], we checked that adding a given amount of salt increases the proportion of spheres breaching the interface, likely because of a strong charge screening. However, we have not tried to investigate the effect of salt in detail and all our experiments were performed in pure water.

Then, occasionally in a few cases, the spheres were actually seen to cross the interface and a transition to a partial wetting configuration occurred with the presence of a clearly visible contact line (see § B-II.2). In this case, switching off the laser had no effect on the particle position which remained well in focus.

The recorded images, either in transmission or reflection mode (§ B-II.2) provide a direct way of estimating contact angle values as a function of time. For example, Fig. B-III.1a shows that the area of the particle that protrudes in the air (central dark region with a bright spot) increases over time: it clearly illustrates the contact angle dynamics. From such pictures, we can easily extract the particle diameter, $2R$, and the diameter of the protruding part in air, $2r(t)$, at some time t . The (dynamic) contact angle $\theta(t)$ is then given by $\theta(t) = \arcsin[r(t)/R]$ and the height $h(t)$ of the sphere above the interface may be computed through $h(t) = R[1 - \cos \theta(t)]$ (Fig. B-III.2). Using such a procedure, Fig. B-III.1b displays four partially wetted spheres which all exhibit different contact angle values.

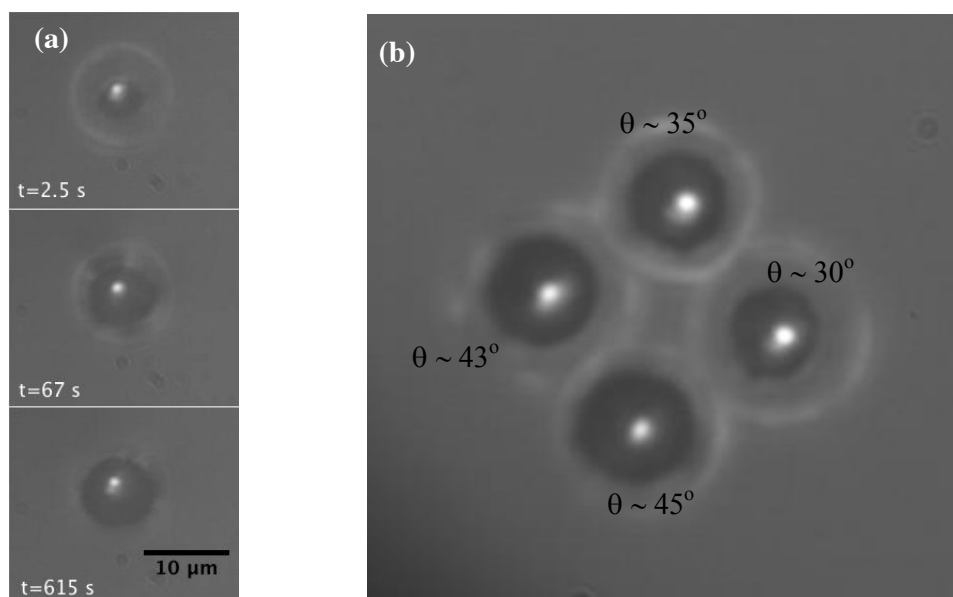


Figure B-III.1: *Partially wetted spheres at the W/A interface imaged using reflection microscopy. (a) Series of images illustrating the wetting dynamics: The area of the particle that protrudes in the air (central dark region with a bright spot) clearly increases over time. (b) A group of spheres showing a distribution of contact angle values. The outer bright halo indicates the actual particle diameter.*

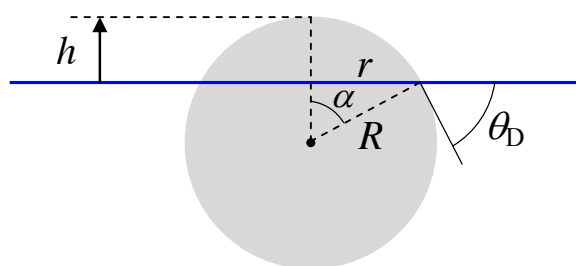


Figure B-III.2 : *Sketch to illustrate the calculation of the dynamic contact angle θ_D from a partially wetted spherical particle. α is the polar angle defining the location of the contact line. Since the interface is flat, $\alpha = \theta_D$.*

We have measured the time evolution of the contact angle for a bunch of spheres that breached the W/A interface. The results are gathered in the graphs of Fig. B-III.3. Similarly to Kaz *et al.*, the wetting dynamics features an initial fast increase of $\theta(t)$ followed by a much slower relaxation as time elapses. All data exhibit the logarithmic behavior mentioned in the introductory part (with some scattering in the slopes) which, as aforesaid, is consistent with a model describing a thermally-activated hopping of the contact line over nanoscale surface defects [Kaz 2012].

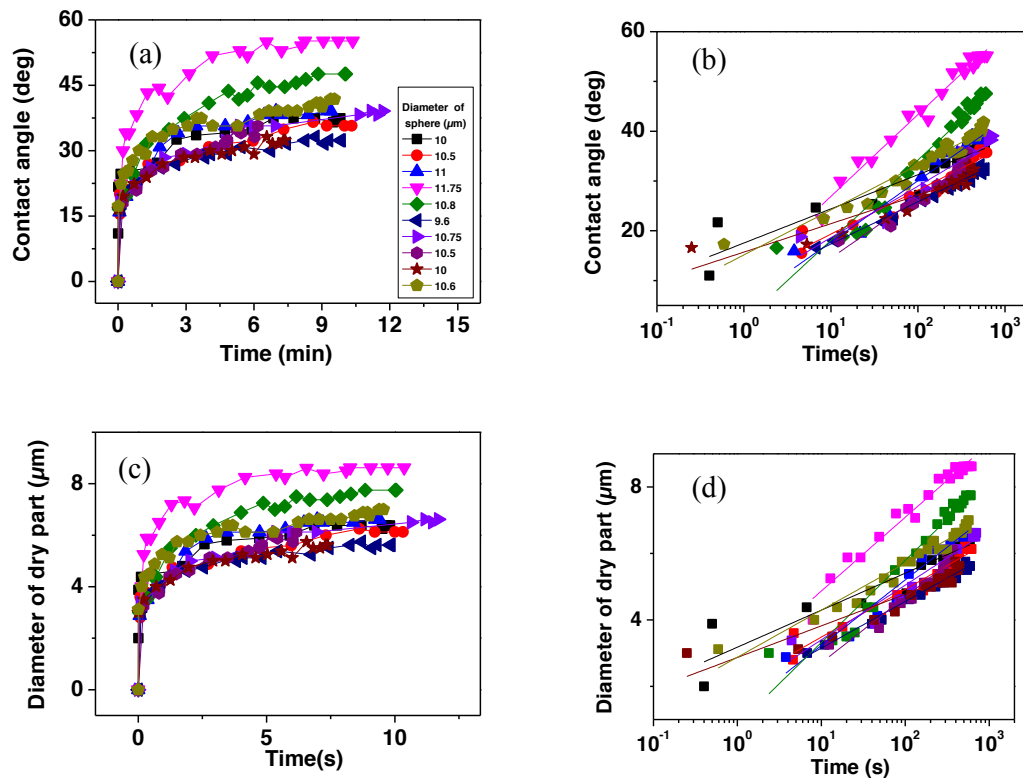


Figure B-III.3: Wetting dynamics data for a collection of spheres. (a) Contact angle versus time right after breaching the W/A interface. (b) Semi-plot of (a). (c) Diameter of the dry part of the sphere versus time right after the breach. (d) Semi-log plot of (c). The graphs in (b) & (d) exhibit the logarithmic dependence mentioned in the text.

Having qualitatively reproduced the main trend observed in previous studies for spheres, we shall now tackle the case of both prolate and oblate ellipsoids.

B-IV: Wetting dynamics of prolate and oblate ellipsoids

The used procedure is exactly the same as that described previously for spheres: the ellipsoids are initially picked up by the laser beam and raised all the way up to the W/A interface. Video microscopy is used to extract most of the useful information. Occasionally though, the photodiode signal was used to record fast dynamical phenomena that could not be resolved at the video rate.

B-IV.1 Results for prolate ellipsoids

Figure B-IV.1 is a typical xz schematic view of the levitation and consequent wetting of a sub-critical (static) ellipsoid. The dashed green line indicates the position of the levitating beam. The vertically aligned particle moves upwards before stalling just underneath the W/A interface. It then begins to tilt, say clockwise, slides sideways from the beam axis, flips horizontally and continues to rotate before breaching the interface with the tip opposite to the one which first started to tilt. As the contact line grows over time, the particle progressively equilibrates and eventually lies flat with its long axis parallel to the interface.

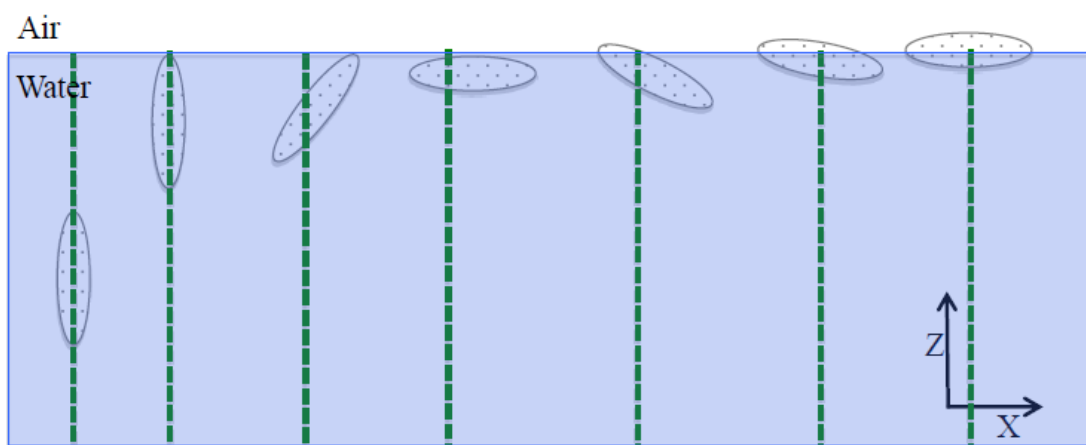


Figure B-IV.1: Sketch of the levitation and wetting dynamics of a sub-critical (static) ellipsoid from the bulk to the W/A interface. The dashed green line corresponds to the laser beam position.

The adsorption trajectory for oscillating ellipsoids ($k_{1,2} > 3$) is qualitatively the same as that described above for sub-critical ones. The particle may oscillate for a while just below the interface prior to slowing down and eventually coming to rest at an angle just as it is depicted in the third sequence of Fig. B-IV.1 above. The subsequent steps are then the same as those mentioned for sub-critical particles.

Therefore, the presence of oscillations does not seem to alter the qualitative picture of the adsorption trajectory. We only noticed that, as the particle is located just below the interface, the crossing of the interface tends to occur faster in the presence of oscillations.

A typical contact line evolution is presented in the time sequence of Fig. B-IV.2 for an initially oscillating ellipsoid ($k_1=3.5$, $k_2=3.2$). Note that the contact line first appears very fast, in a discontinuous manner, close to one of the ellipsoid tips and then grows over time towards the other tip.

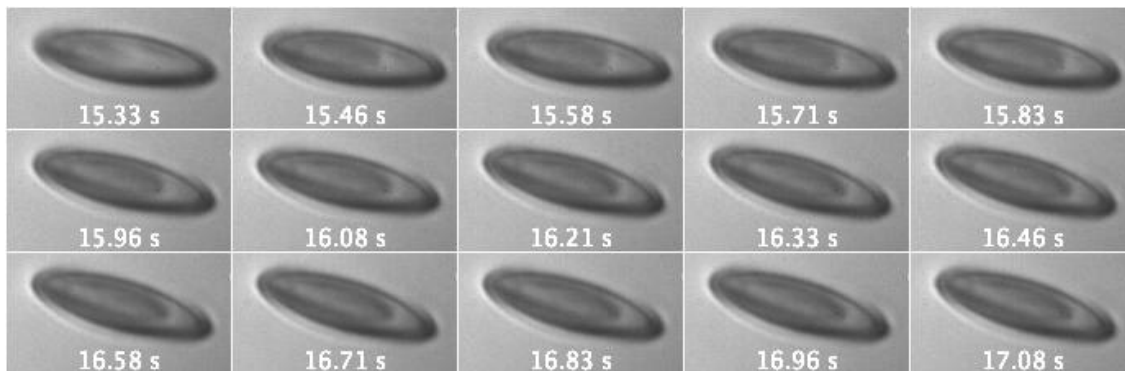


Figure B-IV.2: Time series of images showing the contact line growth on an ellipsoidal particle right after breaching the interface ($k_1=3.5$, $k_2=3.2$). The “central” dark region stands for the dry part of the ellipsoid that protrudes in the air. The boundary separating the dark region from the brighter one may be identified as the contact line.

The photodiode signal was sometimes used to accurately detect the first time the particle breaches the interface. This is evidenced in Fig. B-IV.3 by the sharp drop in signal intensity. From the photodiode signals, we can estimate that the breaching occurs within a time scale of ~ 0.1 s.

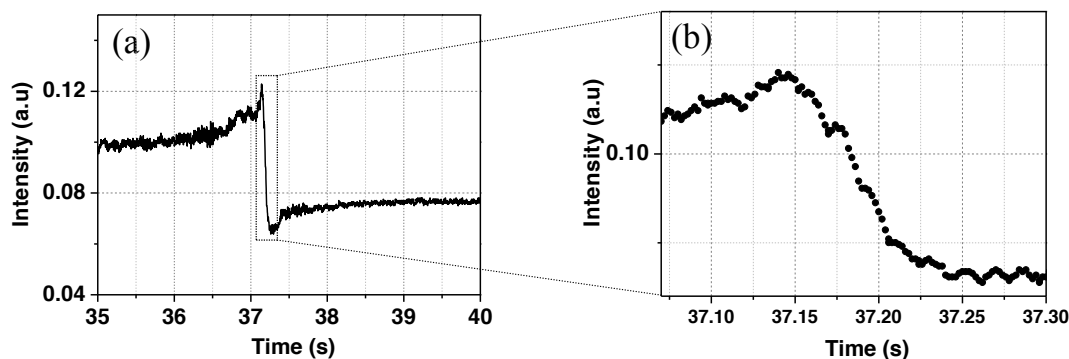


Figure B-IV.3: Photodiode signals recorded for an ellipsoid that crosses the W/A interface (acquisition frequency: 500 Hz). (a) Signal recorded for an ellipsoid with $k_1 \approx k_2 = 3.5$. (b) A zoomed-in view of the region where the signal intensity sharply drops.

As for spheres, we have analyzed the wetting dynamics of a bunch of prolate ellipsoids (both static and oscillating). However, for ellipsoids, the relationship between the protruding area in air, also named “dry part” in the following, and the contact angle is not so simple as it is for spheres because the contact line is non-planar here [Loudet 2006, Lehle 2008]. In addition, the aforementioned tilt of the particle, as it crosses the interface, further complicates the analysis. Numerical computations of contact lines on prolate ellipsoids, such as those reported in [Loudet 2011], might have been useful here but, given the exploratory nature of our experiments, we have not tried to push the analysis too far for the moment. Consequently, we have only measured the dimensions of the elliptical dry parts (long and short axes) of ellipsoids as a function of time. These data nevertheless reflect the wetting dynamics and some results are displayed in the graphs of Figs. B-IV.4 & 5. At short times, the vertical position of ellipsoids changes abruptly before slowing down as time evolves (Fig. B-IV.4). Overall, part of the data seem to follow the same kind of logarithmic relaxation as already pointed out for spheres (Fig. B-IV.5) while some other points do not even span one decade in time and one therefore should be careful. Furthermore, the slope, i.e. the rate of relaxation, changes significantly from particle to particle. According to the model developed in [Kaz 2012] for spheres, the slope of the trajectory is related to the average area of defects which varies with surfaces bearing different functional groups. In our experiments, the surface chemistry is supposedly the same for all particles. Clearly, more data are needed before drawing more definite conclusions.

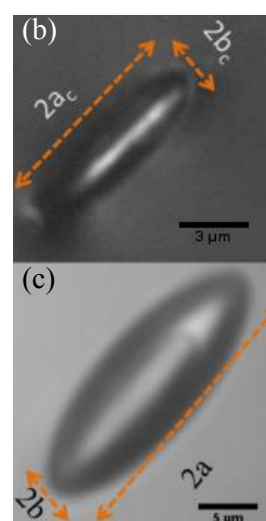
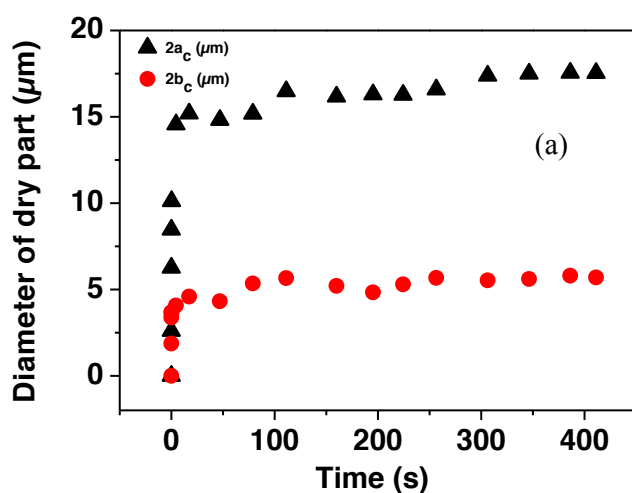


Figure B-IV.4: (a) Time evolution of the protruding elliptical areas (long axis: $2a_c$; short axis: $2b_c$) in air for a sub-critical ellipsoid ($k_1=k_2=2.8$) Black triangles: Long axis. Red circles: short axis. Optical microscopy pictures obtained in reflection (b) and transmission (c) modes.

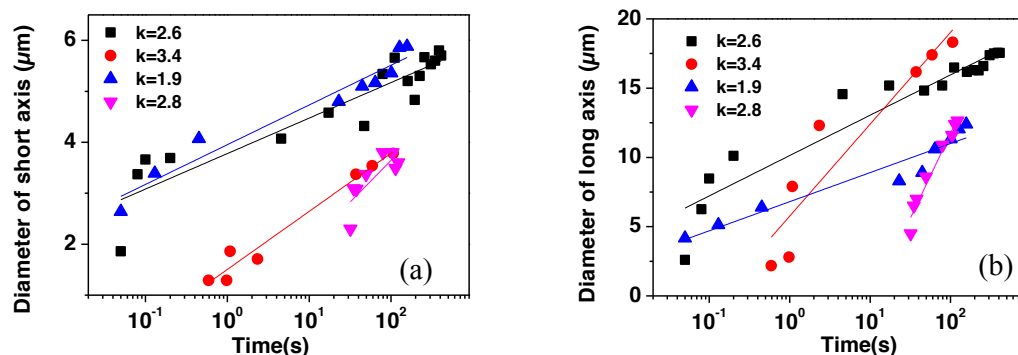


Figure B-IV.5: Semi-log plots of the diameter of the dry part (see text) as a function of time for four prolate ellipsoids with different aspect ratios. (a) Data for short axis. (b) Data for the corresponding long axes.

B-IV.2 Results for Oblate ellipsoids

Oblate ellipsoids follow a similar trend of wetting dynamics as that of prolate ones. Whether the particle is oscillating or static just below the interface, the wetting dynamics starts at an angle from one end and then grows to the other end of the particle. Fig. B-IV.6 below shows a time series (top view images) of an oblate ellipsoid ($k_1=0.45$, $k_2=0.33$) getting partially wetted. In the first image ($t=0.35$ s), the longest axis of the particle is aligned along the z -axis (beam axis) and the second larger axis is oriented parallel to the interface. This orientation may be referred as the “on-edge” configuration. In the second image ($t=5.34$ s) the particle starts to tilt and slide sideways forming an angle with the interface plane. In the remaining images, the particle is partially wetted and the contact line growth is clearly visible.

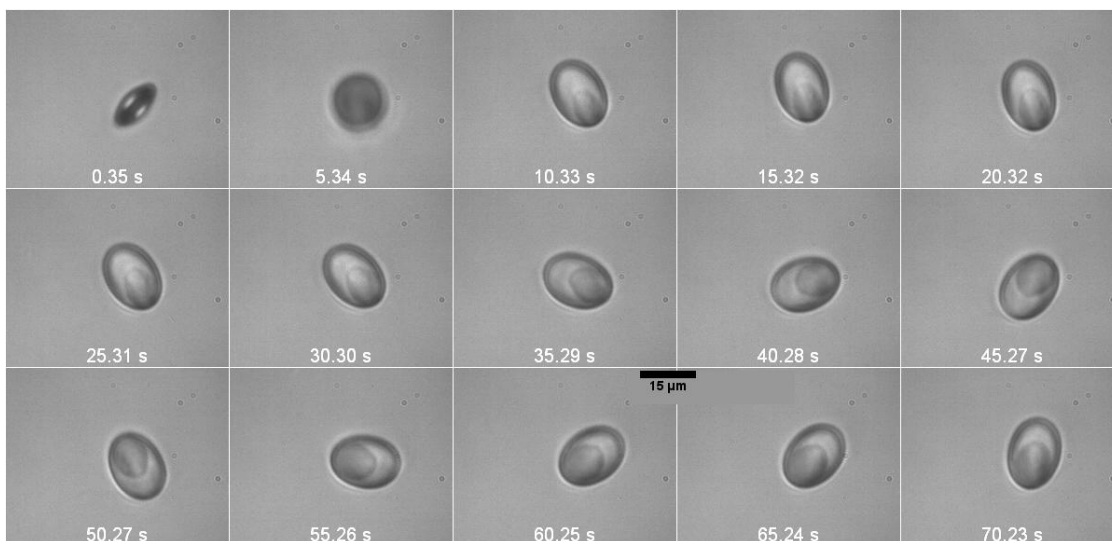


Figure B-IV.6: Wetting dynamics of an oblate ellipsoid ($k_1=0.45$, $k_2=0.33$). The dimensions of the protruding elliptical area in air (darker area) grow over time.

Similarly to prolate ellipsoids, we have measured the time evolution of the dry part for oblate particles. The data are plotted in Figs. B-IV.7 & 8.

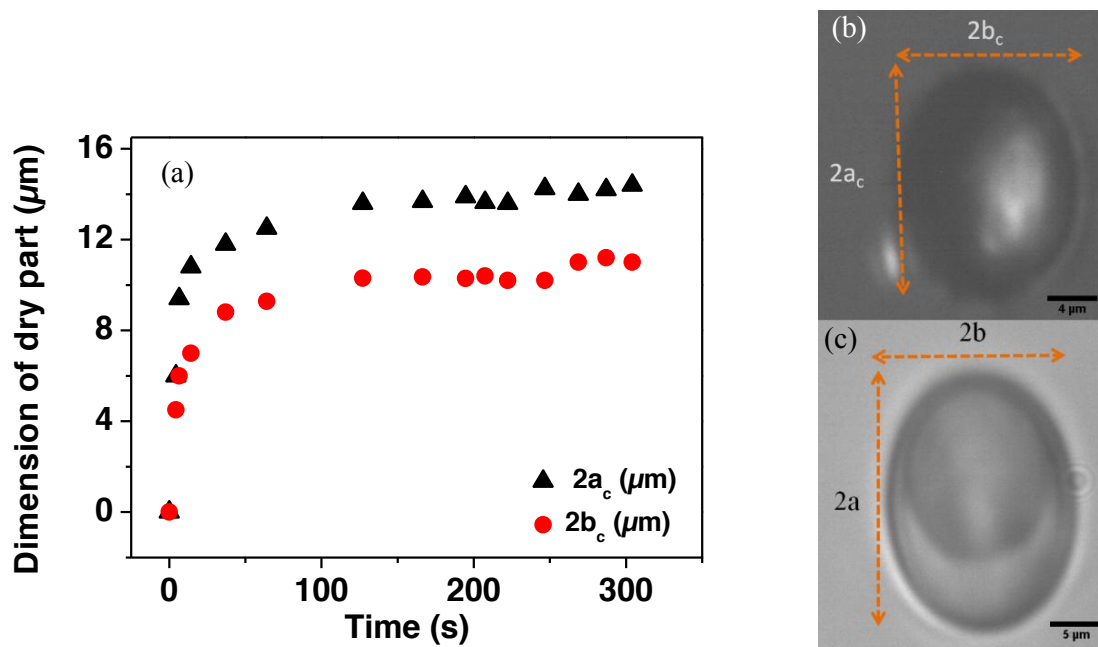


Figure B-IV.7.: (a) Time evolution of the protruding elliptical areas (long axis: $2a_c$; short axis: $2b_c$) in air for an oblate ellipsoid (aspect ratios: $k_1=0.45$, $k_2=0.33$). Red circles: short

axis. Black squares: long axis. Optical microscopy pictures obtained in reflection (b) and transmission (c) modes.

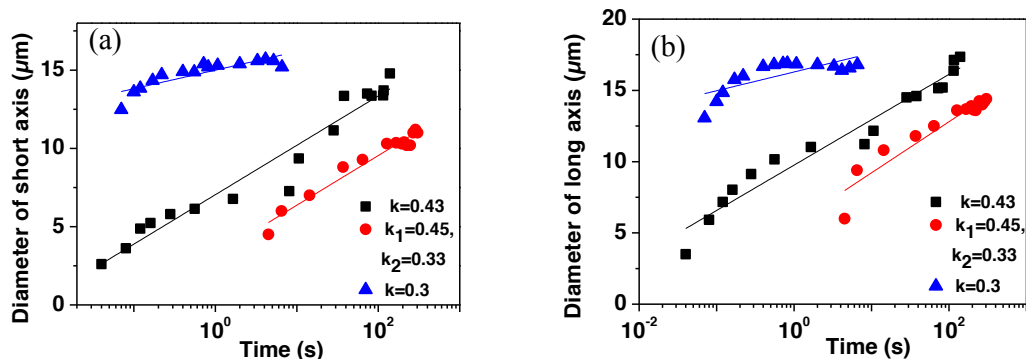


Figure B-IV.8: Semi-log plots of the diameter of the dry part (see text) as a function of time for three oblate ellipsoids with different aspect ratios. (a) Data for short axis. (b) Data for the corresponding long axes.

The qualitative trends are globally the same as those mentioned for prolate ellipsoids: sharp increase at the time of breaching before leveling out at later times. The semi-log plots of Fig. B-IV.8 reflect more or less the logarithmic law evidenced so far but one should be careful since, as aforesaid for particles, some data do not even span one decade and are a bit noisy.

B-IV.3 Discussion

For both prolate and oblate ellipsoids, whether static or oscillating, the adsorption trajectory starts by a sudden interface breach, with the particle at an angle with respect to the interface plane, and then proceeds through a relaxation mechanism where the position of the contact line evolves over time. Ultimately, the particle long axis gets aligned parallel to the interface. This scenario does not agree with what was recently predicted by de Graaf *et al.* in the case of prolate ellipsoids assuming a flat interface [de Graaf 2010]. A typical computed adsorption trajectory from this work is exhibited in Fig. B-IV.9 below. It features a large transient protruding state in air with the particle vertically aligned perpendicular to the interface plane. Eventually, the particle rotates and aligns its long axis parallel to the interface plane. Clearly, such a large excursion in air is not observed in our experiments and one may first call into question the assumptions made by de Graaf *et al.* together with the fact that they ignored the

motion of the contact line. Treating the full problem is not an easy matter at all and needless to say that this issue requires a lot more theoretical and experimental investigations.

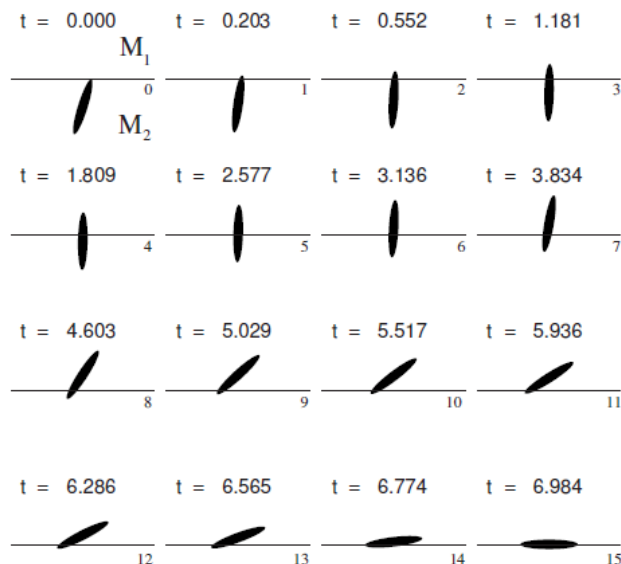
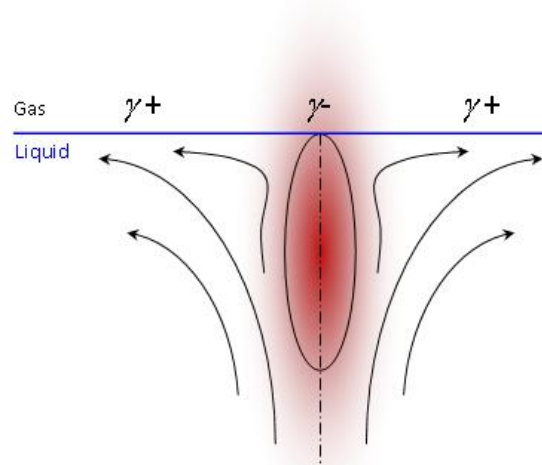


Figure B-IV.9: *Predicted adsorption trajectory for a prolate ellipsoidal particle ($k_1=k_2=6$) [de Graaf 2010]. The indicated t values correspond to the (dimensionless) simulation time.*

Next, we wish to comment a bit on the experimentally observed adsorption trajectory for both prolate and oblate ellipsoids. Whether static or oscillating, the route towards the partial wetting configuration is qualitatively the same. We currently have no solid explanation to explain our observations but we may tentatively invoke thermal effects and make the following reasoning :

Although our PS particles do not absorb the used laser light ($\lambda=514$ nm), or very little so, we cannot rule out at 100% that absorption does not occur to some tiny extent. If so, the particle becomes a hot spot after a while which can easily create a thermal gradient in the immediate vicinity of the W/A interface. Now this thermal gradient may induce a surface tension gradient which in turn may trigger the onset of convection currents in a thin layer of fluid close to the interface. This is the Marangoni effect, a well-known phenomenon in interfacial hydrodynamics [Landau 1994; Guyon, Hulin, Petit 2001]. Such a flow (see Fig. B-IV.10) will exert a force on the particle which may be strong enough to push it out of the laser beam axis. As described above, the ellipsoids indeed first tilt away from the beam axis and further slide sideways before breaching the interface. Therefore, we may surmise that this tilting and sliding might be thermally induced through a Marangoni effect.

Figure B-IV.10: *Sketch of a thermally-induced flow close to a fluid interface due to a Marangoni effect (surface tension gradient). The origin of the thermal gradient would be a slight absorption of the laser light by the ellipsoid which becomes a hot spot.*



This conjecture prompted us to answer the following question: what would be the minimal thermal gradient required for Marangoni forces to be large enough and compete with radiation pressure forces ?

Working out the orders of magnitude (see appendix B for details), we estimate that temperature differences as small as ~ 1 mK close to the interface would be sufficient to drive a particle motion due to thermally induced fluid flows.

Hence, thermal effects cannot be entirely ignored and are likely to play a role in our levitation experiments at fluid interfaces. Note, however, that such Marangoni effects cannot appear in the levitation experiments carried out at the glass interface since there is no surface tension to be considered in this case. It is worth emphasizing that ellipsoids could oscillate for hours at the top of the glass cell while it was never so with fluid interfaces: after a few minutes, the ellipsoids stall and breach the interface as already described above.

Consequently, experiments at free surfaces require special care and the point raised above definitely calls for more in-depth investigations.

A final comment deals with the wetting dynamics investigated in this work.

A slow logarithmic relaxation towards equilibrium takes place with spheres but also with both prolate and oblate ellipsoids apparently. Although better statistics are needed for ellipsoids,

our results might not be too surprising after all: indeed, although the contact lines for ellipsoids are non planar at the micrometer scale, there are also likely to be rugged and undulated at the nanoscale because of tiny surface defects, similarly to spheres. If the motion of the contact line is mainly governed by a thermally-activated pinning-depinning mechanism over defects, as proposed by Kaz *et al.*, the actual global shape of the contact line may not be the most relevant factor influencing the wetting dynamics. So, as long as the particle surface bears defects, a slow relaxation towards equilibrium could be a general trend whatever the particle shape.

Conclusion and prospects

The main part of this report has been focused on the behaviour of ellipsoid-shaped particles in response to optical forces from a moderately focused laser beam. The particles were fabricated from polystyrene spheres, 10 μm in diameter. Prolate ellipsoids ($k > 1$) were generated by uniaxial stretching, and oblate ones ($k < 1$) by biaxial stretching of the spheres. We thus obtained ellipsoids with dimensions between a few μm and several 10 μm . We studied the behaviours of these particles in a classical levitation experiment, with a vertical laser beam, in water. The beam waist diameter was 2.6 μm , with a corresponding diffraction length $\approx 14 \mu\text{m}$. We collected many observations with particles of different aspect ratios located in different regions of the beam. The altitude in the beam was fixed either by using the balance between the particle weight and the optical levitation force, or by bringing the particle in contact to the upper surface of the sample cell. We thus observed the particles' responses in bulk water and close to a surface, which might be solid (water-glass) or fluid (water-air and water-oil interfaces).

Near the beam-waist, particles which were not too far from a sphere got trapped on the laser beam axis in static configurations, with their long axes lying vertical. Conversely, we found that particles of high ellipticity, either rod-like ($k \gg 1$) or disk-like ($k \ll 1$) never came to static configurations: they were seen to undergo sustained oscillations, in the form of coupled translation and tilt motions.

We have proposed an interpretation of the observed dynamical behaviours on the basis of a simple 2-dimensional (2d) model, using the ray-optics approximation. For prolate ellipsoids and a simply parallel beam, the model indeed produced a bifurcation between static states and limit cycles when k increases. As an essential outcome, the model showed that the non linear dependence of the radiation pressure forces versus the particle position and angle coordinates was enough to explain the oscillations. In our model, and contrary to [Cheng 2003], no special hydrodynamic contribution from bounding surfaces was required as a necessary condition to produce oscillations.

The model, being 2-dimensional, can only predict static equilibriums and periodic dynamical states (limit cycles). Such states are indeed observed in experiments, but the 3-dimensional character of the real system generates more complex dynamics in certain cases. Using

standard tools of non linear dynamics analysis, we indeed evidenced irregular dynamics akin to deterministic chaos with particles of various size parameters, at various altitudes in the laser beam. However, we were not able to evidence a simple route to chaos. From our experience, we can tell whether a given particle will stay static in the beam or oscillate, but we are not at the point where we can say a priori whether the motion of this particle will be periodic or irregular.

The work on particles' dynamical states may be continued and extended in different directions:

- Our experiments were limited to a simple levitation scheme, with a moderately focused beam. In view of the applications related to optical manipulation, it would be very interesting to move to configurations that allow for true 3d trapping, at least for spheres. We might then go to more strongly focused beams, up to conditions of single beam optical tweezers. As an alternative, we may keep the option of weak focusing but add a second -contra-propagating- beam to set up a two-beam trap (see e.g. [\[Rodrigo 2004-2005\]](#)). The latter configuration offers the advantage of long working distances, which then would allow us to confine the particle far from the cell boundaries for a wide range of laser power and then avoid complications due to hydrodynamic coupling to surfaces. The configuration has the further advantage of being compatible with side observation, contrary to optical tweezers.
- We need more feedback from theory and simulations. There is still much to be learnt from the ray-optics model. Still in the 2d version, the model may be made more complete by taking into account the divergence of the beam. This would help us simulate the behaviours of particles in different regions of the beam, as we did in the experiments. One relatively simple question to be addressed is the vertical-to-horizontal transition that we observed with particles far from the beam-waist. Extension to 3d is possible too, as was done recently by [\[Chang 2012\]](#).

In the course of our PhD we started a few calculations of optical forces and torques in 3d, using the discrete-dipole-approximation, under the supervision of Prof. F. Ren (CORIA, Rouen). This work (not reported in this manuscript) has not gone further than preliminary results with particle sizes limited to a few μm . The project now has been taken over by M. Yang and F. Ren, with the method called "Multilevel Fast

Multipole Algorithm” (MLFMA). Most interestingly, this method allows dealing with the large particle sizes of our experiments.

Much information is expected from the forthcoming simulations, both in the ray-optics and MLFMA versions. Predictions of optical forces and torques for static states may be verified by future experiments; these will be stringent tests to validate the computation methods.

Prediction of oscillatory regimes is expectably a very demanding task, first because of the many degrees of freedom (up to 6) of the particle to be included in the dynamical equations. A second difficulty lies in the hydrodynamic part of the problem, to represent the viscous drag force and torque that oppose the action of the radiation pressure. In the 2d model, we simply supposed that translation and rotation were decoupled, and we adopted constant drag coefficients. Reality is more complex because the translation drag depends on the particle orientation [[Happel 1983](#)]. Ultimately, the hydrodynamic part of the problem may call for dedicated numerical simulation (as in [[Chang 2012](#)]), in parallel to the part on optical force-torque.

Beyond the academic study of the particles’ responses to optical forces, we applied the levitation technique to a problem pertaining to physical chemistry of surfaces. We investigated how polystyrene particles, initially in bulk water, come to a static equilibrium across the water-air interface, in partial wetting configuration. We focused our study on possible differences between spheres and ellipsoids, because we suspected that the non planarity of contact lines on ellipsoidal bodies might cause a difference in the dynamics of the particle emersion, compared to spheres. In fact, the data that we collected showed that there was no real difference. We concluded that in all cases the dynamics of the contact line is mainly controlled by the pinning-depinning mechanism, in line with the recent results of [[Kaz 2012](#)] for spherical micrometre-sized spheres. This conclusion holds equally for spheres and ellipsoids, either prolate or oblate. Conversely models that do not take this peculiar mechanism into account [[de Graaf 2010](#)] lead to definitely unrealistic prediction of particles’ emersion dynamics.

Coming back to mechanical effects of light, the problem of a particle that sits across an interface (e.g. water-air) has not yet been fully addressed. Basically the problem amounts to calculating the electromagnetic field scattered by a particle located across the planar boundary between two semi-infinite dielectric media. To our knowledge, no accurate solution has been

proposed up to now, even in the case of a sphere. Solutions may be within reach of modern computation methods (see cited references in chapter A-V), and would be very useful to determine partial wetting configurations of particles from scattered light diagrams. Since optical forces are the direct consequence of light scattering, we may check results of calculations through simple measurements of forces and torques necessary to move particles parallel to the interface. Such experiments may be readily performed using the tools developed throughout this work.

Conclusion et perspectives

Dans la majeure partie de cette étude, nous nous sommes intéressés aux réponses de particules en forme d'ellipsoïdes aux forces optiques exercées par un faisceau laser modérément focalisé. Nos particules sont obtenues à partir de sphères de polystyrène, de 10 μm de diamètre, par étirement uniaxial (pour des ellipsoïdes prolates, $k > 1$) ou biaxial (pour des ellipsoïdes oblates, $k < 1$). Ce procédé nous a permis de fabriquer toute une gamme de particules, dont les dimensions vont de 5 à 50 μm environ. Nous avons étudié les comportements des ellipsoïdes dans une expérience classique de lévitation optique, avec un faisceau laser vertical, dans l'eau. Dans ce montage, le faisceau est modérément focalisé, avec un rayon au col (beam-waist) de 2.6 μm et une longueur de diffraction $\approx 14 \mu\text{m}$. Nous avons fait de nombreuses observations avec des particules de rapports d'aspect variés dans des régions différentes du faisceau. Nous avons contrôlé l'altitude de chaque particule dans le faisceau en utilisant l'équilibre entre son poids et la force de lévitation optique, ou en amenant la particule au contact de la surface en haut de la cellule d'expérience. Cette surface était dans la plupart des cas une paroi de verre, mais nous avons également étudié les cas de particules au contact d'interfaces eau-air et eau-huile.

Nous avons montré qu'au voisinage du beam-waist, les particules prolates peu ou modérément allongées ($k < 3$) se piègent radialement sur l'axe du faisceau, en configuration verticale. Par contre, les particules fortement elliptiques, en forme de bâtonnet ($k \gg 1$) ou de disque ($k \ll 1$) ne peuvent pas être immobilisées. Ces particules « dansent » autour du faisceau, dans un mouvement permanent associant translation et rotation.

Nous avons proposé une interprétation des dynamiques observées à partir d'un modèle simple en dimension 2 (2d), dans l'approximation de l'optique géométrique. Pour des ellipsoïdes prolates et un faisceau parallèle (la diffraction est négligée), ce modèle prédit une bifurcation entre états statiques et dynamiques périodiques (cycles limites) lorsque l'allongement k augmente. Une conclusion essentielle de cette analyse est que les oscillations viennent de la non linéarité des forces et couples optiques en fonction des variables de position et d'orientation de la particule. Dans ce modèle, la contribution hydrodynamique associée au

contact avec une paroi n'est pas une condition nécessaire pour l'existence d'oscillations, contrairement au modèle de [Cheng 2003].

Ce modèle, étant limité à 2 dimensions, ne peut produire que des équilibres statiques ou des oscillations périodiques. Ces états sont effectivement observés dans les expériences, mais le caractère tridimensionnel du système réel engendre des dynamiques plus complexes dans certains cas. En utilisant des méthodes standards de l'analyse des signaux non linéaires, nous avons montré l'existence de dynamiques irrégulières, assimilables à du chaos déterministe.

A partir de l'ensemble de nos observations, nous pouvons dire si une particule ellipsoïdale de caractéristiques données pourra être immobilisée dans le faisceau ou si elle va osciller. Par contre nous ne savons pas prédire la nature des oscillations, périodique ou irrégulière. Pour le moment, l'ensemble des analyses n'a pas permis de dégager une « route vers le chaos », en changeant simplement les rapports d'aspect ou l'altitude de la particule dans le faisceau.

Plusieurs pistes se présentent pour continuer ce travail:

- nous avons limité nos expériences au seul schéma de la lévitation optique, avec un faisceau modérément focalisé. Pour nous rapprocher des applications utilisant la manipulation optique, il faudrait faire évoluer le montage vers des versions permettant le piégeage en 3 dimensions, tout au moins pour des particules sphériques. Une option est de focaliser beaucoup plus fortement le faisceau, comme dans la géométrie des pinces optiques. Une alternative est de garder le principe d'une faible focalisation, mais d'ajouter un faisceau coaxial en sens inverse pour créer un piège à deux faisceaux (voir par ex. [Rodrigo 2004-2005]). Cette version offre l'avantage d'une grande distance de travail, ce qui permet de travailler loin dans le volume et d'éviter la complication d'un couplage hydrodynamique avec une paroi. On peut en même temps observer la particule par le côté, ce qui est difficilement envisageable avec une pince optique.

- Il est souhaitable de pousser beaucoup plus loin la modélisation et les simulations. Le simple modèle d'optique géométrique en 2d peut encore nous apprendre beaucoup de choses, en particulier l'effet de la divergence du faisceau. Le modèle pourrait ainsi rendre compte de l'effet du diamètre de faisceau vu par la particule en fonction de l'altitude. Une question relativement simple concerne la transition entre les configurations verticale et horizontale quand on s'éloigne du beam-waist.

Il serait évidemment très utile d'aller vers une version 3d du modèle, comme dans la récente étude de Chang et al. [[Chang 2012](#)].

Au cours de cette thèse, nous avons entrepris des calculs des forces et couples optiques en 3d avec l'aide du Prof. F. Ren, par la technique DDA (« discrete-dipole-approximation »). Ce travail (non décrit dans le manuscrit) est resté exploratoire et s'est limité à des particules de quelques μm seulement. Le projet est mené maintenant par M. Yang et F. Ren, qui utilisent la méthode MLFMA (“Multilevel Fast Multipole Algorithm”). Cette technique est très prometteuse, parce qu'elle permet de traiter les cas des « grandes » particules de nos expériences.

La simulation permettra de calculer précisément les amplitudes des forces et couples. Les valeurs calculées pourront être vérifiées avec les particules en équilibre statique. Les mesures expérimentales des effets mécaniques de la lumière sur ces particules serviront donc d'outil de validation des codes de calcul.

- Prédire les oscillations en 3d est une affaire probablement beaucoup plus ambitieuse, d'abord parce qu'il faut inclure tous les degrés de liberté (jusqu'à 6) dans les équations du mouvement. Une deuxième difficulté se présente dans la partie hydrodynamique du problème. Il faut modéliser les forces et couples de trainée dus à la viscosité du fluide. Dans le modèle 2d que nous avons présenté, nous avons considéré que les composantes translationnelle et rotationnelle de la trainée étaient découplées et régies par des coefficients constants. En réalité, la force translationnelle dépend de l'orientation de la particule [[Happel 1983](#)]. Une simulation complète devrait inclure une partie numérique dédiée à l'hydrodynamique, comme dans l'étude de [[Chang 2012](#)].

Dans la partie B du manuscrit nous avons présenté une application de la lévitation optique pour une étude de la dynamique de démouillage des surfaces de nos particules. Nous avons observé comment une particule de polystyrène, initialement dans l'eau, se place en travers de l'interface eau-air, où elle adopte une configuration de mouillage partiel. Nous avons étudié la dynamique de cette transition et recherché si elle dépend fortement de la forme de particule, depuis la sphère jusqu'à des ellipsoïdes très allongés (prolates) ou plats (oblates). Nous avons conclu qu'il n'y avait en fait pas de variations notables entre ces différents cas. Nos observations indiquent que, quelle que soit la forme de la particule, la dynamique de la ligne de contact est régie essentiellement par le mécanisme d'accrochage-décrochage sur les défauts de la surface. Cette conclusion corrobore celle de [[Kaz 2012](#)] dans leur récente étude pour

des sphères de l'ordre du micromètre. Au contraire, les dynamiques que nous avons observées sont très différentes de celles prédites par le modèle de [de Graaf 2010], qui ne prend pas en compte ce mécanisme.

Nous terminons en revenant vers les effets mécaniques de la lumière, cette fois sur une particule à l'interface, en mouillage partiel. Pour calculer les forces et couples exercés par un faisceau laser sur cette particule, il faut calculer le champ électromagnétique diffusé par cette particule. Le problème est celui d'un corps en travers d'une surface plane à la frontière entre deux milieux diélectriques semi-infinis. A notre connaissance, aucune solution de ce problème n'est disponible dans la littérature, même pour une sphère. Des solutions numériques peuvent certainement être obtenues avec les outils modernes que nous avons cités (voir le chapitre A-V). On pourrait, à partir de la simulation, déterminer la configuration de mouillage partiel à partir d'un diagramme de diffusion. Une alternative simple est de mesurer la force nécessaire pour déplacer la particule parallèlement à la surface avec un faisceau laser. La valeur de cette force étant directement liée au champ diffusé, l'expérience permettrait de valider le calcul. Ces mesures sont faisables directement avec les outils que nous avons développés au cours de cette thèse.

Bibliography

- Alpmann C., *et al.*, Holographic optical bottle beams, *Appl. Phys. Lett.* **100**, 111101 (2012).
- Arlt J., and Padgett M. J., Generation of a beam with a dark focus surrounded by regions of higher intensity: the optical bottle beam, *Opt. Lett.* **25**, 191-193 (2000).
- Ashkin A., Acceleration and trapping of particles by radiation pressure, *Phys. Rev. Lett.* **24**, 156 (1970).
- Ashkin A., *et al.*, Observation of a single-beam gradient force optical trap for dielectric particles, *Opt. Lett.* **11**, 288 (1986).
- Ashkin A., Forces of a single beam gradient laser trap on a dielectric sphere in the ray optics regime, *J. Biophys.* **61**, 569-82 (1992).
- Ashkin A., *Optical trapping and manipulation of neutral particles using lasers*, (World Scientific, London 2006).
- Aveyard R., Binks B. P., and Clint J. H., Emulsions stabilized solely by colloidal particles, *Adv. Coll. Interface Sci.* **100-102**, 503-546 (2003).
- Bansal R.K., *"A text book of fluid mechanics"* (New Delhi, 2006).
- Bareil P. B., and Sheng Y., Angular and position stability of a nanorod trapped in an optical tweezers, *Opt. Express* **18**, 26388-26398 (2010).
- Benito D., Simpson S. H., and Hanna S., FDTD simulations of forces on particles during holographic assembly, *Opt. Express* **16**, 2942–2957 (2008).
- Berge' P., Pomeau Y., and Vidal C., *"Order within Chaos: Towards a Deterministic Approach to Turbulence"* (Wiley, New York, 1986).
- Beth R. A., Mechanical detection and measurement of the angular momentum of light, *Phys. Rev.* **50**, 115-125 (1936).
- Binks B. P., Particles as surfactants, *Curr. Opinion Colloid Interface Sci.* **7**, 21 (2002).
- Binks B. P., Horozov T. S. (Eds), *"Colloidal Particles at Liquid Interfaces"*, Cambridge Univ. Press, 2006.
- Bobadova-Parvanova P., and Pouligny B., unpublished (1995).
- Bonessi D., Bonin K., and Walker T., Optical forces on particles of arbitrary shape and size, *J. Opt. A, Pure Appl. Opt.* **9**, S228–S234 (2007).

Borghese F., et al., Radiation torque and force on optically trapped linear nanostructures, *Phys. Rev. Lett.* **100**, 163903 (2008).

Buican T. N., et al., Optical trapping, cell manipulation, and robotics, *Proc. SPIE* **1063**, 190 (1989).

Cao Y., et al., Equilibrium orientations and positions of nonspherical particles in optical traps, *Opt. Express* **20**, 12987 (2012).

Champion J. A., Katare Y. K., and Mitragotri S., Particle shape: A new design parameter for micro-and nanoscale delivery carriers, *J.Control. Release* **121**, 3-9 (2007).

Chang C. B., et al., Optical levitation of a non-spherical particle in a loosely focused Gaussian beam, *Opt. Exp.* **20**, 24068 (2012).

Chaumet P. C., Rahmani A., and Nieto-Vesperinas M., Optical trapping and manipulation of nano-objects with an apertureless probe, *Phys. Rev. Lett.* **88**, 123601 (2002).

Chen W., et al., Long-ranged attraction between charged polystyrene spheres at aqueous interfaces, *Phys. Rev. Lett.* **95**, 218301 (2005).

Cheng Z., Chaikin P. M., and Mason T. G., Light streak tracking of optically trapped thin microdisks, *Phys. Rev. Lett.* **89**, 108303 (2002).

Cheng Z., Mason T. G., Chaikin P. M., Periodic oscillation of a colloidal disk near a wall in an optical trap, *Phys. Rev. E* **68**, 051404-9 (2003).

Danjean S., "*Manipulation optique de sphères au contact de la surface libre de l'eau, Rapport de stage de DEA de physique*", Université de Bordeaux (1996).

Danov K. D., et al., Interactions between particles with an undulated contact line at a fluid interface: Capillary multipoles of arbitrary order, *J. Colloid and Interface Sci.* **287**, 121–134 (2005).

Daoud M., and Williams C.E., "*Soft Matter Physics*", (Springer, 1999).

Dendukuri D., et al., Controlled synthesis of non spherical micro particles using micro fluidics, *Langmuir* **21** (6), 2113 (2005).

Dendukuri D., et al., Continuous-flow lithography for high-throughput micro particle synthesis, *Nat. Mater.* **5** (5), 365 (2006).

Destribats M., Schmitt V., and Backov R., Thermostimulable wax@SiO₂ core-shell particles, *Langmuir* **26** (3), 1734-1742 (2010).

Dickey F. M., Holswade S.C., “*Laser beam shaping theory and techniques*” (New York, 2000).

Dinsmore A. D., *et al.*, Colloidosomes: Selectively permeable capsules composed of colloidal particles, *Science* **298**, 214-227 (2002).

Draine B. T., and Flatau P. J., Discrete-dipole approximation for scattering calculations, *J. Opt. Soc. Am. A* **11**, 1491–1499 (1994).

Friese M. E. J., Optical alignment and spinning of laser-trapped microscopic particles, *Nat.* **394**, 348-350 (1998).

Friese M. E. J., *et al.*, Optically driven micromachine elements, *Appl. Phys. Lett.* **78**, 547-549 (2001).

Gahagan K. T., Swartzlander G. A. Jr., Optical vortex trapping of particles, *Opt. Lett.* **21**, 827-829 (1996).

Gahagan K. T., and Swartzlander G. A. Jr., Trapping of low-index microparticles in an optical vortex, *J. Opt. Soc. Am. B* **15**, 524-534(1998).

Gauthier R. C., Theoretical investigation of the optical trapping force and torque on cylindrical micro-objects, *J. Opt. Soc. Am. B* **14**, 3323 (1997).

Gauthier R. C., Ashman M., and Grover C. P., Experimental confirmation of the optical-trapping properties of cylindrical objects, *Appl. Opt.* **38**, 4861(1999).

de Gennes P. G., Brochart-Wyart F., and Quéré D., in “*Gouttes, bulles, perles et ondes*”, Ed. (Belin, Paris, 2005).

Glassner A. S., “*An Introduction to Ray Tracing*”, Ed. San Francisco: Morgan Kaufmann, 1989.

Gouesbet G., Maheu B., and Grehan G., Light scattering from a sphere arbitrarily located in a Gaussian beam, using a Bromwich formulation, *J. Opt. Soc. Am. A* **5**, 1427–1443(1988).

de Graaf J., Dijkstra M., and van Roij R., Adsorption trajectories and free-energy separatrices for colloidal particles in contact with a liquid-liquid interface, *J. Chem. Phys.* **132**, 164902 (2010).

Grover S. C., Gauthier R. C., and Skirtach A. G., Analysis of the behaviour of erythrocytes in an optical trapping system, *Opt. Express* **7**, 533–539 (2000).

Guzowski J. J., PhD thesis, “*Capillary interactions between colloidal particles at curved fluid interfaces*”, Institut für Theoretische und Angewandte Physik Universität Stuttgart & Max-Planck-Institut für Metallforschung Stuttgart (2010).

Guyon E., Hulin J. P., and Petit L., “*Hydrodynamique physique*”, EDP Sciences (CNRS Editions), 2001.

Happel J., Brenner H., “*Low Reynolds Number Hydrodynamics*”, Ed The Hague: Martinus Nijhoff Publishers (1983).

Hegger R., Kantz H., and Schreiber T., Practical implementation of nonlinear time series methods: The TISEAN package, *Chaos* **9** (2), 413 (1999).

Hinojosa-Alvarado A., Gutiérrez-Vega J. C., Geometrical optics calculation of forces and torques produced by a ringed beam on a prolate spheroid, *J. Opt. Soc. Am. B* **27**, 1651-8 (2010).

Ho C. C., *et al.*, Preparation of monodisperse ellipsoidal polystyrene particles, *Colloid Polym. Sci.* **271**, 469 (1993).

van der Horst A., *et al.*, Manipulating metal-oxide nanowires using counter-propagating optical line tweezers, *Opt. Express* **15**, 11629-11639 (2007).

Horsthemke W., and Lefever R., “*Noise-Induced Transitions*”, ed. Springer Verlag, Berlin Heidelberg, New York, Tokyo (1984).

Imasaka T., *et al.*, Optical Chromatography, *Anal. Chem.* **67**(11), 1763-5 (1995).

Jackson J. D., “*Classical Electrodynamics*”, John Wiley & Sons Ltd. 1962.

Jonáš A., Zemánek P., Light at work: The use of optical forces for particle manipulation, sorting, and analysis, *Electrophoresis* **29**, 4813 (2008).

Jones P. H., Maragó O. M., and Stride E. P. J., Parametrization of trapping forces on microbubbles in scanning optical tweezers, *J. Opt. A: Pure and Applied Opt.* **9**, S278-S283 (2007).

Katok A., Hasselblatt B., “*Introduction to the Modern Theory of Dynamical Systems*” Ed. Cambridge: Cambridge Univ. Press, 1995.

Kaz D. M., *et al.*, Physical ageing of the contact line on colloidal particles at liquid interfaces, *Nature Materials* **11**, 138-142 (2012).

Kennel M. B., Brown R., and Abarbanel H. D. I., Determining embedding dimension for phase space reconstruction using a geometrical construction, *Phys. Rev. A* **45**, 3403 (1992).

Kraikivski P., Pouligny B., and Dimova R., Implementing both short- and long-working-distance optical trapping into a commercial microscope, *Rev. Sci. Instrum.* **77**, 113703 (2006).

Kralchevsky P. A., Denkov N. D., and Danov D. K., Particles with an undulated contact line at a fluid interface: Interaction between capillary quadrupoles and rheology of particulate monolayers, *Langmuir* **17**, 7694-7705 (2001).

Lai Y.-C., Ye N., Recent developments in chaotic time series analysis, *Int. J. Bifurcation and Chaos* **13**, 1383-1422 (2003).

Landau L. D. and Lifchitz E. M., “*Cours de physique théorique – Mécanique des fluides*”, Ed. Ellipses (Editions Marketing, 1994).

Lehle H., Noruzifar E., Oettel M., Ellipsoidal particles at fluid interfaces, *Eur. Phys. J. E* **26**, 151 (2008).

Lewandowski E. P., Bernate J. A., Searson P. C., and Stebe K. J., Rotation and alignment of anisotropic particles on nonplanar interfaces, *Langmuir* **24**, 9302-9307 (2008).

Loudet J. C., *et al.*, Capillary interactions between anisotropic colloidal particles, *Phys. Rev. Lett.* **94**, 018301 (2005).

Loudet J. C., Yodh A. G., and Pouligny B., Wetting and contact lines of micrometer-sized ellipsoids, *Phys. Rev. Lett.* **97**, 018304 (2006).

Loudet J. C., and Pouligny B., Self-assembled capillary arrows, *Europhys. Lett.* **85**, 28003 (2009).

Loudet J. C., and Pouligny B., How do mosquito eggs self assemble on the water surface, *Eur. Phys. J. E* **34**, 76 (2011).

Lucassen J., Capillary forces between solid particles in fluid interfaces, *Colloids and Surfaces* **65**, 131–137 (1992).

Mbamala E. And von Grunberg H., Effective interaction of a charged colloidal particle with an air-water interface, *J. Phys. Condens. Matter* **14**, 4881-4900 (2002).

Mondiot F., “*Behavior of colloidal particles in nematic solvents: shape and size effects*”, thesis, University of Bordeaux 1(2011).

Neuman K. C., and Block S.M., Optical trapping, *Rev. Sci. Instr.* **75**, 2787-809 (2004).

- Neves A., *et al.*, Rotational dynamics of optically trapped nanofibers, *Opt. Express* **18**, 822-830 (2010).
- Nieminen T. A., *et al.*, Optical tweezers computational toolbox, *Journal of Optics A: Pure and App. Opt.* **9**, S196-S203 (2007).
- Oettel M. and Dietrich S., Colloidal interactions at fluid interfaces, *Langmuir* **24**(4), 1425-1441 (2008).
- Pauzauskie P. J., *et al.*, Optical trapping and integration of semiconductor nanowire assemblies in water, *Nat. Mat.* **5**, 97-101(2006).
- Pickering S. U., Emulsions, *J. Chem. Soc.* **91**, 2001-2021 (1907).
- Plewa J., Processing carbon nanotubes with holographic optical tweezers, *Opt. Express* **12**, 1978-1981 (2004).
- Qin J.-Q., *et al.*, FDTD approach to optical forces of tightly focused vector beams on metal particles, *Opt. Express* **17**, 8407–8416 (2009).
- Quatieri T. F., “Discrete- Time speech signal processing: Principle and Practice”, Prentice hall PTR, 2002.
- Ren K. F., Grehan G., and Gouesbet G., Radiation pressure forces exerted on a particle arbitrarily located in a Gaussian beam by using the generalized Lorenz-Mie theory, and associated resonance effects, *Opt. Commun.* **108**, 343–354 (1994).
- Ren K. F., *et al.*, Vectorial complex ray model and application to two-dimensional scattering of plane wave by a spheroidal particle, *Opt. Exp. Lett.* **36**, 3 (2011).
- Rodrigo P. J., Daria V. R., and Glückstad J., Real-time three-dimensional optical micromanipulation of multiple particles and living cell, *J. Opt. Lett.* **29**, 2270 (2004).
- Rodrigo P. J., *et al.*, Actuation of microfabricated tools using multiple GPC-based counterpropagating-beam traps, *Opt. Express* **13**, 6899–6904 (2005a).
- Rodrigo P. J., Daria V., and Glückstad J., Four-dimensional optical manipulation of colloidal particles, *Appl. Phys. Lett.* **86**, 074103 (2005b).
- Rodriguez-Otazo M., *et al.*, High rotation speed of single molecular microcrystals in an optical trap with elliptically polarized light, *Appl. Opt.* **48**, 2720-30. (2009).
- Roosen G., and Imbert C., Optical levitation by means of two horizontal laser beams: A theoretical and experimental study, *Phys. Lett.* **59A**, 6 (1976).

Roosen G., A theoretical and experimental study of the stable equilibrium positions of spheres levitated by two horizontal laser beams, *Opt. Commun.* **21**, 189 (1977).

Roosen G., thesis, Université Paris XI (1978).

Sauer T., Yorke J., and Casdagli M., *Embedology*, *J. Stat. Phys.* **65**, 579 (1991).

Schreiber T., Interdisciplinary application of nonlinear time series methods, *Phys. Rep.* **308**, 1 (1997).

Seveno D., *et al.*, Dynamics of wetting revisited, *Langmuir* **25**, 13034-13044 (2009).

Sheng X. Q., *et al.*, Solution of combined-field integral equation using multilevel fast multipole algorithm for scattering by homogeneous bodies, *IEEE Trans. Antenn. Propag.* **46**, 1718–1726 (1998).

Shvedov V. G., Robust trapping and manipulation of airborne particles with a bottle beam, *Opt. Express* **19**, 17350-17356 (2011).

Siegman A., “*Lasers*”, (USA, 1986).

Simpson S. H., and Hanna S., Optical trapping of spheroidal particles in Gaussian beams, *J. Opt. Soc. Am. A* **24**, 430-443(2007).

Simpson S. H., and Hanna S., Optical angular momentum transfer by Laguerre–Gaussian beams, *J. Opt. Soc. Am. A* **26**, 625–638 (2009).

Simpson S. H., and Hanna S., First-order nonconservative motion of optically trapped nonspherical particles, *Phys. Rev. E* **82**, 031141 (2010a).

Simpson S. H., and Hanna S., Holographic optical trapping of microrods and nanowires, *J. Opt. Soc. Am. A* **27**, 1255–1264 (2010b).

Simpson S. H., and Hanna S., Computational study of the optical trapping of ellipsoidal particles, *Phys. Rev. A* **84**, 053808(2011a).

Simpson S. H., and Hanna S., Optical trapping of microrods: variation with size and refractive index, *J. Opt. Soc. Am. A* **28**, 850-858 (2011b).

Song J. M., and Chew W. C., Multilevel fast multipole algorithm for solving combined field integral equations of electromagnetic scattering, *Micro. Opt. Tech. Let.* **10**, 14–19 (1995).

Sosa-Martínez H., Gutiérrez-Vega J. C., Optical forces on a Mie spheroidal particle arbitrarily oriented in a counterpropagating trap, *J. Opt. Soc. Am. B* **26**, 2109-16 (2009).

Takens F., in “*Detecting Strange Attractors in Turbulence*”, Lecture Notes in Mathematics Vol. **898** (Springer-Verlag, New York, 1981).

Thamilmaran K., Lakshmanan M., Classification of bifurcations and routes to chaos, *Int. J. Bifurcation and Chaos* **12**, 783-813 (2002).

Thomson J. M. T., and Stewart H. B., in “*Nonlinear Dynamics and Chaos*” (Wiley, 1986).

Ueda Y., “*Steady motions exhibited by Duffing’s equation: a picture book of regular and chaotic motions in New Approaches to Nonlinear Problems in Dynamics*”, Ed. P. J. Holmes, SIAM Philadelphia (1980).

Varadan V. K., and Varadan V. V., eds., “*Acoustic, Electromagnetic and Elastic Wave Scattering: Focus on the T-matrix Approach*” (Pergamon, 1980).

Velikov K. P., and Velev O.D., “*Stabilization of thin films, foams, emulsions and bifluid gels with surface-active solid particles*”, in *Colloid Stability and Application in Pharmacy*, T. F. Tadros, Ed., Wiley-VCH Publ. Weinheim (2007).

Vossen D. J., *et al.*, Optical tweezers and confocal microscopy for simultaneous three-dimensional manipulation and imaging in concentrated colloidal dispersions, *Rev. Sci. Instrum.* **75**, 2960–2970(2004).

Walz J. Y., Prieve D. C., Prediction and measurement of the optical trapping forces on a microscopic dielectric sphere, *Langmuir* **8**, 3073-82 (1992).

White D. A., Numerical modeling of optical gradient traps using the vector finite element method, *J. Comput. Phys.* **159**, 13–37 (2000).

Wilking J. N., and Mason T. G., Multiple trapped states and angular Kramers hopping of complex dielectric shapes in a simple optical trap, *Eur. phys. Lett.* **81**, 58005 -58005(2008).

Xu S.Q., *et al.*, Generation of monodisperse particles by using micro fluidics: control over size, shape, and composition, *Angew. Chem., Int. Ed. Engl.* **44** (5), 724 (2005).

Xu F., *et al.*, Theoretical prediction of radiation pressure force exerted on a spheroid by an arbitrarily shaped beam. *Phys. Rev. E* **75**, 026613 (2007).

Xu F., *et al.*, Radiation torque exerted on a spheroid: Analytical solution. *Phys. Rev. E* **78**, 013843-59 (2008).

Yurkin M. A., and Hoekstra A. G., The discrete dipole approximation: an overview and recent developments, *J. Quant. Spectrosc. Radiat. Transf.* **106**, 558–589 (2007).

Appendix A

Wetting energy of a spherical particle at a fluid interface and viscous dissipation near the contact line

A-1) Wetting energy of a sphere at a liquid-gas interface

We summarize here a well-known thermodynamic calculation to compute the wetting energy of spherical particle at a fluid interface.

Let us consider a smooth solid spherical particle of radius a floating at a flat liquid-gas interface characterized by surface tension γ (Fig. A1). The equilibrium position of the sphere is determined by the minimum of the total surface free energy F which can be written as [Guzowski 2010]

$$F = \gamma_{sl} \Delta S_{sl} + \gamma_{sg} \Delta S_{sg} + \gamma \Delta S_{lg} ,$$

where ΔS_{sl} (resp. ΔS_{sg} , ΔS_{lg}) corresponds to the change of the surface energy of the sphere-liquid (resp. sphere-gas, liquid-gas) contact area S_{sl} (resp. S_{sg} , S_{lg}) characterized by surface tension γ_{sl} (resp. γ_{sg} , γ).

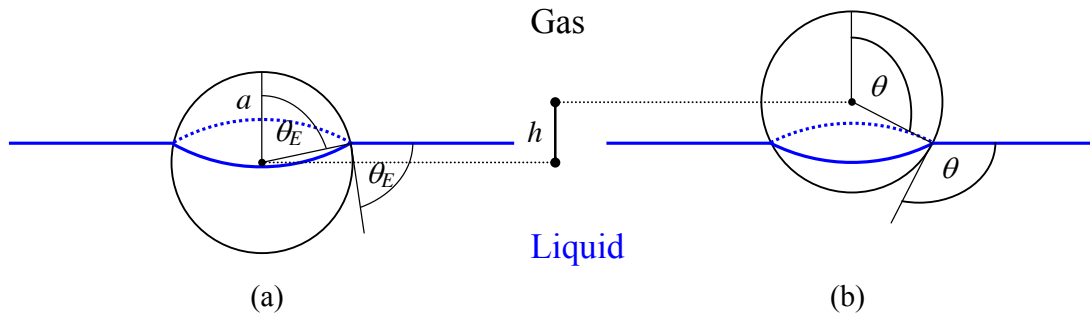


Figure A1: Sketches of the configuration of a sphere trapped at a flat liquid-gas interface. (a) corresponds to the reference configuration with $\theta = \theta_E$ whereas (b) represents a configuration with an arbitrary polar angle θ .

Since $\Delta S_{sg} = -\Delta S_{sl}$, after applying Young's law

$$\cos \theta_E = \frac{\gamma_{sg} - \gamma_{sl}}{\gamma} ,$$

we obtain

$$F = \gamma \left(-\cos \theta_E \Delta S_{sl} + \Delta S_{lg} \right),$$

where θ_E is the equilibrium contact angle. The contact areas are functions of the polar angle θ which specifies the position of the tpc-line at the particle surface (see Fig. B-I.1). Taking as a reference the configuration with $\theta = \theta_E$, one has

$$\begin{aligned} \Delta S_{sl} &= 2\pi a^2 (\cos \theta - \cos \theta_E), \\ \Delta S_{lg} &= -\pi a^2 (\sin^2 \theta - \sin^2 \theta_E). \end{aligned}$$

Therefore, the surface free energy F can be expressed as

$$F = \gamma \pi a^2 (\cos \theta - \cos \theta_E)^2 = \gamma \pi h^2,$$

where the height $h = a(\cos \theta - \cos \theta_E)$ is measured with respect to the reference configuration (Fig. A1). A plot of F as a function of h/a is presented on Fig. B-I.2 in the main text (§ B-I).

A-2) Viscous dissipation near the contact line

In this paragraph, we quickly show how the shear flow from a wedge of fluid near a moving contact line on a solid surface leads to a diverging viscous dissipation, as mentioned in the main text (section B-I). This situation is well-known and described in details in standard textbooks [Guyon, Hulin, Petit, 2001, de Gennes 2005]. For the sake of completeness and clarity, we only provide the reader with the main steps of the reasoning.

We consider the simplified situation sketched in Fig. A2 with an ideal linear liquid wedge making a small contact angle value ($\tan \theta_D \sim \theta_D$) with the solid substrate. Since θ_D differs from θ_E (out of equilibrium situation), a non zero surface tension force, F_γ , is exerted on the contact line, pulling the liquid towards the dry area. The work (per unit of time) done by F_γ to generate the flow inside the liquid wedge may be written as

$$\frac{dE_\gamma}{dt} = F_\gamma V = \gamma (\cos \theta_E - \cos \theta_D) V,$$

where V is the contact line velocity⁸. As stated in the main text, the corresponding energy will be dissipated by the viscous flow occurring in the liquid wedge.

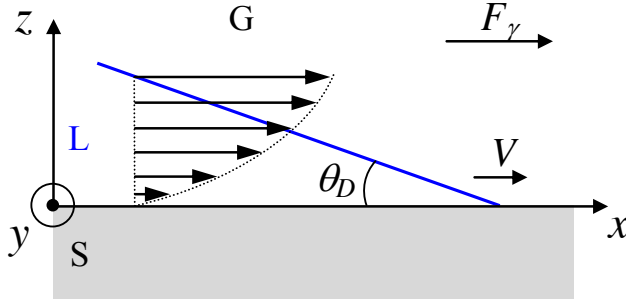


Figure A2 : Flow in the highly confined region near the contact line (spreading regime $\theta_D > \theta_E$). The contact angle value is small. The traction force F_γ makes the contact line move with a velocity V that is the average of the fluid flow velocity over the local thickness. L stands for “liquid”, S for “solid” and G for “gas”. Adapted from [de Gennes 2005].

Next, we need to know the velocity profile of the fluid flow in the confined region close to the contact line. Using the lubrication approximation (the tangential stress, $\eta \partial v_x / \partial z$, is zero at the free surface) together with the condition that the velocity field $v_x(z)$ is zero on the solid surface ($v_x(0)=0$), one ends up with a velocity profile of the form (see Fig. A2)

$$v_x(z) \propto [e(x) - z/2]z,$$

where $e(x)$ is the local interface height ($e(x) = \theta_D x$). The exact expression shows that the fluid velocity at the free surface is greater (by a factor 1.5) than the average fluid velocity which turns out to be equal to V . The velocity gradient may therefore be written

$$\partial v_x / \partial z \sim V / \theta_D x.$$

Noting η the liquid viscosity, the dissipated energy (per unit of time) by the viscous flow, dE_η/dt , is given by (per unit length along the y -direction)

$$\frac{dE_\eta}{dt} = \int_0^\infty dx \int_0^e \eta \left(\frac{\partial v_x}{\partial z} \right)^2 dz \propto \frac{\eta V^2}{\theta_D} \int_0^\infty \frac{dx}{x}.$$

⁸In situations of complete wetting ($\theta_E=0$), there is always a precursor film (of submicrometer thickness) located in front of the moving contact line that we have not represented on Fig. A2. The angle θ_D is actually an *apparent* dynamic contact angle in this case.

The above integral diverges at both limits and one has to introduce two cutoff lengths, one at large x ($x=L \sim$ size of the spreading drop or size of the colloidal particle in our case), and another at small x ($x=a \sim$ molecular length). It is found that $l=\ln(L/a) \sim 15$ to 20 [de Gennes 2005].

Then, writing $dE_\gamma/dt = dE_\eta/dt$ leads to (using the small angle approximation)

$$V(\theta_D) \propto \frac{\gamma}{\eta l} \theta_D (\theta_D^2 - \theta_E^2) .$$

Two important remarks may be raised from the above $V(\theta_D)$ law :

- (i) when $\theta_D \rightarrow \theta_E$, we find $V = 0$, which is expected once equilibrium is reached.
- (ii) we also have $V \rightarrow 0$ when $\theta_D \rightarrow 0$: the dissipation in a highly confined region is strongly enhanced and stalls the contact line motion.

The latter point could have explained the slow wetting dynamics of interfacial colloids observed by Kaz *et al.* [Kaz 2012] but, as mentioned in the main text, this damping mechanism is not consistent with the reported experimental trends and orders of magnitude.

Note, however, that the above law $V \sim (\theta_D)^3$ (Tanner's law) is well-verified experimentally in dynamic wetting experiments on macroscopic solid surfaces (with $\theta_E = 0$) [Guyon, Hulin, Petit, 2001, de Gennes, 2005].

Appendix B

Thermal gradients at fluid interfaces

In this appendix, we shortly derive the orders of magnitude of the Marangoni and radiation pressure (RP) forces to tentatively account for the adsorption trajectories observed with ellipsoids (see discussion § B-IV.3).

(i) Radiation pressure forces, F_{RP} , are of order:

$$F_{\text{RP}} \sim \varepsilon P/c ,$$

where P is the laser power, c the speed of light in vacuum and ε a factor of order 0.1 [Ashkin, 1970, 2006].

(ii) Marangoni forces stem from a surface tension gradient originating from an interfacial thermal gradient [Landau 1994, Guyon, Hulin, Petit, 2001] and read :

$$F_{\text{Mar}} \sim 2\pi a(d\gamma) ,$$

where $d\gamma = (d\gamma/dT)dT$ is the change in surface tension due to a temperature gradient dT and a is the typical short dimension of a (prolate) ellipsoid.

Putting the following typical numbers, $P = 10$ mW, $c = 3.10^8$ m/s, $a = 3$ μm and $d\gamma/dT \approx 3.10^{-4}$ N.m⁻¹.K⁻¹ [Guyon, Hulin, Petit, 2001, de Gennes 2005], and writing that $F_{\text{RP}} \sim F_{\text{Mar}}$ lead to

$$dT \sim 1 \text{ mK} .$$

Therefore, very small temperature differences close to the water-air interface would be sufficient to make Marangoni forces comparable to radiation pressure ones.